AD610634

U. S. ARMY
TRANSPORTATION RESEARCH COMMAND
FORT EUSTIS, VIRGINIA

TRECOM TECHNICAL REPORT 64-42

THEORETICAL AND EXPERIMENTAL STUDIES OF
IMPINGING UNIFORM AND NONUNIFORM JETS

Task 1D121401A14129
Contract DA 44-177-AMC-18(T)

August 1964

COPY 2 OF 3

HARD COPY $.4.00
MICROFICHE $.0.75

102 p

prepared by:

CORNELL AERONAUTICAL LABORATORY, Inc.
Buffalo, New York 14221

DDC

FEB 3 1 1965

DDC-IRA B

DISCLAIMER NOTICE

DDC AVAILABILITY NOTICE

This report has been reviewed by the U. S. Army Transportation
Research Command and is considered to be technically sound.   The
report is published for the exchange of information and the
stimulation of ideas.

FOR THE COMMANDER:

PATRICK A. CANCRO
Project Engineer

JOHN E. YEATES
Acting Leader
Aeromechanics Group

APPROVED.

FOR THE COMMANDER:

LARRY M. HEWIN
Technical Director

THEORETICAL AND EXPERIMENTAL STUDIES OF IMPINGING UNIFORM AND NONUNIFORM JETS

CAL Report TG-1818-S-1

FOREWORD

The work described in this report was accomplished by the Cornell Aeronautical Laboratory, Inc. (CAL), Buffalo, New York, for the U.S. Army Transportation Research Command (USATRECOM), Fort Eustis, Virginia, over an eleven-month period starting May 1963. The work was performed under Contract DA 44-177-AMC-18(T), "VTOL Downwash Impingement Problems." Dr. Gary R. Ludwig and Mr. W. Gordon Brady of CAL conducted the study, and Mr. J. McHug and, subsequently, Mr. P. Cancro administered the project for USATRECOM.

The authors extend their appreciation to Messrs. C. Ryan, J. Balcer and J. Nemeth of CAL for their significant contributions to the investigation.

The work reported herein is a continuation of the initial effort under Contract DA 44-177-TC-782 that was reported in TRECOM Technical Report 63-11, Theoretical and Experimental Studies of Impinging Uniform Jets, April 1963.

TABLE OF CONTENTS

LIST OF ILLUSTRATIONS

LIST OF SYMBOLS

D Diameter of Jet Nozzle at Exit = 1 foot

H Distance of Jet Nozzle Exit From Ground, feet

M_r Radial Momentum Flux, Slugs-ft./(sec.)^2

P_A Atmospheric Pressure, psf.

P_S Static Pressure, psf.

P_T Total Pressure, psf.

Q_r Radial Mass Flow, Slugs/sec.

R D/2

U Average Velocity in Nozzle $= \dfrac{2}{R^2}\int_0^R v r_N \, dr_N$, fps.

$\bar{U}_M$ Mean Radial Momentum Velocity $= \sqrt{\dfrac{2}{R^2}\int_0^R v_r v r_N \, dr_N}$, fps.

U_R Reference Velocity $= \sqrt{\dfrac{2 q_R}{\rho}}$, fps.

U_∞ Jet Reference Velocity $= \sqrt{\dfrac{2 P_T}{\rho}}$, fps. (Uniform Jet Only)

W Absolute Value of Velocity, fps.

q_R Reference Dynamic Pressure = Wind Tunnel Settling Chamber Pressure, psf.

r Radial Distance Along Ground Board from Stagnation Point, feet

r_N Radial Distance from Jet Axis in Nozzle Exit Plane, feet

t Distance from Nozzle Exit, Positive Toward Ground Plane, feet

u Local Velocity Parallel to Ground Plane, fps.

u_m Maximum Value of u Attained in the Ground Flow at Any One Radial Station, fps. (See Figure 6)

v Local Velocity Perpendicular to Ground Plane, fps.

V_T Velocity Based on Local Total Pressure $= \sqrt{\dfrac{2(P_T - P_A)}{\rho}}$ fps.

y Distance Above G ound Board, feet

y_m y When $u = u_m$ (see Figure 6)

$y_{1/2}$ y When $u = \frac{1}{2} u_m$ in Outer Ground Flow Region (see Figure 6)

z Distance Above Ground Board Along Jet Centerline, feet

α Form Parameter Associated With Ground Flow Reynolds Number for Radial Wall-Jet (see Reference 4)

θ Angular Coordinate About Jet Centerline (θ is measured clockwise looking downstream. $\theta = 0$ is vertically upward.)

ρ Air Density, Slugs/ft^3

δ_t $= y_m - y_{1/2}$, feet

ν Kinematic Viscosity, ft^2/sec

SUMMARY

The results of an experimental investigation of the flow under a
normally impinging nonuniform jet are presented. The jet velocity
profile was designed to be representative of rotors and ducted fans.
Primary emphasis was placed on determining the properties of the
flow near the ground. Some measurements of the flow in the turning
region of the jet are also presented along with flow visualization
pictures. The jet was tested at distances from the ground of 4, 2,
and $\frac{1}{2}$ nozzle diameters. The data are compared to corresponding,
previously published data obtained with a uniform jet. An approximate
analysis which uses an empirical relation for radial mass flow near
the ground is used to calculate the properties of the flow along the
ground at radii large enough so that the pressure gradient is approxi-
mately zero. The results of the approximate analysis are compared
to the experimental data for both the uniform and the nonuniform
impinging jets.

A method of calculating the properties of the flow in an inviscid,
normally impinging, uniform jet has been formulated. The formula-
tion is applicable for all distances between the jet nozzle and the ground.
Solutions have been obtained for jets at nozzle-to-ground distances of
$\frac{1}{4}$ and 1 jet diameters. The mathematical model used was based on
a vortex-sheet representation, and solutions were obtained by means
of an iterative technique using an IBM 704 digital computer. Good
agreement was obtained with experimental ground-plane and jet-
centerline pressure distributions,and with nozzle-exit velocity profiles.

1

CONCLUSIONS

On the basis of the results presented both in this report and in Reference 1, the following conclusions can be drawn regarding the flow under impinging uniform and nonuniform jets of circular cross section. The nonuniform jet considered here is one with a triangular velocity distribution similar to that generated by rotors and ducted fans.

1. The flow in the turning region of a normally impinging nonuniform jet with a triangular velocity distribution is substantially different from that under a uniform jet. Under the nonuniform jet there is a region of upwash near the center of impingement which is not present with a uniform jet.

2. Once the jet has been completely turned by the ground, the flows under both types of jets rapidly approach the form of a turbulent radial wall jet. For the same thrust per unit area, the maximum velocity and thickness of the flow in the wall jet region are almost identical for both jets for values of $H/D \leq 1$. At larger values of H/D, the flow under the nonuniform jet is thicker and reaches a lower maximum velocity than that under a uniform jet of equal radius and thrust. These differences are relatively small.

3. The flow under a nonuniform jet with a triangular velocity distribution is extremely sensitive to small deviation angles from the normal impingement condition. (No check of the effect of tilt angle was made during the earlier uniform jet experiments; but based on the general experience gained in setting up conditions for normal flow impingement for both types of jets, a uniform jet may not exhibit such sensitivity.)

TR 64-42

4. An approximate analysis developed to predict the properties
    of the flow along the ground under both uniform and nonuniform
    jets provided satisfactory agreement with the experimental
    data for sufficiently large radii. (This analysis, based on
    Glauert's wall-jet theory and an empirical curve for radial
    mass flow, is strictly valid only in regions where the static
    pressure gradient along the ground is zero.)

5. Solutions for the properties of the inviscid flow under uniform
    impinging jets with $H/D = 1.0$ and $H/D = 0.25$ have been obtained
    on a digital computer using a vortex-sheet representation
    for the free-jet boundary. The computed results for the
    flow in the turning region of the impinging uniform jet can
    be applied to the real viscous jet problem with good accuracy
    in the range $H/D \leq 1$. At larger values of H/D, viscous mixing
    significantly alters the real flow from the inviscid flow.

RECOMMENDATIONS

On the basis of the results presented herein and in Reference 1, the following recommendations are made.

1.   A brief quantitative experimental investigation of the effect of tilting the uniform and nonuniform jets from the normal impingement condition should be made.

2.   Experimental measurements of the aerodynamic forces on objects in ground-plane flows similar to those observed under the uniform and nonuniform jets should be made. The resulting data should then be combined with the completed studies of the flow field under impinging jets to provide a means of predicting particle entrainment under hovering VTOL vehicles.

TECHNICAL DISCUSSION
I INTRODUCTION

A major attraction of VTOL aircraft is their ability to operate from unprepared sites. Such an ability does not come without some serious problems, one of which is the entrainment of particles on the ground into the jet or rotor downwash during takeoff, and hovering or slow-speed flight near the ground. In order to obtain an understanding of the ground particle entrainment process, it is necessary to know both the nature of the flow near the ground and the forces which act on particles immersed in such a flow. The research described in this report is part of a continuing program conducted at Cornell Aeronautical Laboratory, designed to investigate particle entrainment under hovering VTOL vehicles.

To date, the properties of the flow under normally impinging uniform and nonuniform jets have been studied. The experimental investigation of the flow in a uniform impinging jet and the formulation of a method of solution for the equivalent inviscid problem have been presented in References 1 and 2. This report presents the results of an experimental study of a normally impinging nonuniform jet and the completed inviscid analysis of the uniform impinging jet. The nonuniform jet had an approximately triangular velocity profile similar to that generated by rotors and ducted fans. In addition, an approximate method of analysis to determine the properties of the flow along the ground after the jet has been turned is presented and the results are compared with experiment.

II EXPERIMENTAL PROGRAM

A. Experimental Apparatus

The CAL-Air Force One-Foot High-Speed Wind Tunnel was used
during the experimental research. The transonic-supersonic test
section was completely removed. A 12-inch-diameter molded fiber-
glass nozzle, designed to produce a uniform parallel flow at the exit,
was mounted to an adapter plate on the test section face of the wind
tunnel settling chamber. An axisymmetric shear screen mounted in a
circular 1-foot-diameter tube (Figure 1) was fastened to the end of
the uniform jet nozzle. This shear screen was designed to generate
a near triangular jet velocity distribution across the radius at the exit
of the extended nozzle. The ground board was 8 by 8 feet square
and could be set at varying distances from the nozzle. A pattern of
static pressure taps was located on the ground board. These taps
were connected to an inclined manometer board. Photographs of
the experimental apparatus, excluding the shear screen assembly, have
been presented in References 1 and 2.

Velocities and static pressures in the jet were measured with total
and static pressure probes mounted on a traverse mechanism. In
addition, some velocity profiles in the jet near the ground were mea-
sured with a hot-wire anemometer. Ground flow measurements were
obtained with small static and total-head probes extending through holes
in the ground board and mounted to a second traversing mechanism, so
made that the position of the probe relative to the ground could be
determined with accuracy. The boundary layer total-head probe was
made from 0.014-inch O. D. hypodermic tubing with a tip tapered to
0.009 inch. The static probe was made from hypodermic tubing with an

outside diameter of 0.032 inch. The boundary layer probes were attached to a small U-tube manometer on the reverse side of the ground board.

A flow visualization technique was used to obtain pictures of the flow in the impinging jets. A typical arrangement for these tests is shown in Figure 2. This photograph was taken during the earlier un form jet experiments, so the shear screen is not shown. In these tests, a thin steel or aluminum plate (splitter plate) was suspended by an angle-iron frame in the horizontal plane of symmetry of the jet. The frame was constructed so that it did not interfere with the flow. The plate was coated with a mixture of powdered graphite (lampblack) and kerosene, and the flow was started. When a well-defined pattern had developed, the flow was stopped. When the mixture was completely dry, the plate was removed and photographed. In addition, patterns were obtained for the flow along the ground under the nonuniform jet. No flow visualization pictures were recorded for the flow along the ground under the uniform jet because exploratory tests showed nothing of significance, only the expected symmetrical pattern of radial stream-lines originating at the jet centerline.

B. Experimental Results

1. Flow Visualization Pictures

Since the lampblack and kerosene flow pictures provide a visualization of the turning process, these pictures will be presented first so that the quantitative measurements can more easily be interpreted. Some general comments on the technique and its limitations are given in Appendix I. A previously obtained flow picture for the uniform im-pinging jet is included for purposes of comparison.

Photographs of the patterns obtained are presented in Figures 3 through 5 for H/D = 2. The streamline pattern on the splitter plate in the uniform jet (Figure 3) behaves as expected. Near the nozzle, there is a central area of potential flow surrounded by a mixing region which grows in thickness with distance from the nozzle. Turning of the jet appears to occur first at a distance of approximately one nozzle diameter above the ground. In this picture, the trailing edge of the plate was 6 inches from the ground level. This rather large gap along with the cutout in the rear center portion of the splitter plate was required to prevent boundary layer separation. This effect is discussed in Appendix I.

With the nonuniform jet the flow in the deflecting portion of the jet is altered considerably (Figure 4(a)). The trailing edge of the splitter plate in this picture is only 1 inch from the ground. There is a dome-shaped region surrounding the center of the impingement area in which the flow moves radially inward along the ground and then curves upward and outward to mix with the impinging flow. At the base of this dome,there is a toroidal- or doughnut -shaped vortex sitting a short distance above the ground. At large radial distances, the flow near the ground approached that of the classical turbulent radial-wall jet, just as in the case of the uniform jet. The flow under the nonuniform jet is similar to that found under annular-jet ground-effect machines. Note that there is a region of upwash under jets having a velocity which increases with the distance from the axis.

The flow along the ground which corresponds to Figure 4 (a) is shown in Figure 4 (b). [*] The inflow region is surrounded by a stagnation ring (dark circle) where the velocity is essentially zero. Outside of

---

[*] The black square in the center of the photograph is a piece of blotting paper which was used to soak up an excess of lampblack and kerosene mixture which tended to accumulate in that region. Deviation of the indicated streamline pattern from radial flow just above the blotting paper is a gravity effect on the kerosene-lampblack. This occurred because the board was mounted vertically in the tests.

this ring, the flow is directed radially outward. In all cases for which flow pictures were obtained (H/D = 4, 2, 1, $\frac{1}{2}$), the stagnation ring coincided with the position of maximum static pressure along the ground, and its radius was larger than the radius of the toroidal vortex observed on the corresponding splitter-plate pictures.

The general features of the pictures obtained at the other values of H/D were similar to those shown here, the only difference being that the size of the dome-shaped region, the toroidal vortex and the stagnation ring all became smaller as H/D was either increased or decreased from the value of 2. A probable explanation for this effect is that on one hand, as H/D is decreased, the jet is constrained by the nozzle walls and so the region in which turning of the jet occurs must be reduced. On the other hand, as H/D is increased beyond 2, mixing of the jet with still air prior to turning tends to reduce the effective shear in the jet so that any effect associated with shear in the jet before impinge-ment will also tend to be reduced. The type of shear being considered here is that which will provide a velocity minimum on the jet axis. Parabolic profiles such as are found in fully-developed pipe flow have a shear of the opposite sense. This latter type of velocity profile will not form a toroidal vortex with its associated central region of reversed flow.

Figure 5 illustrates the effect of small deviations from the normal impingement condition for the nonuniform jet. These photographs were obtained with a tilt angle of 5 degrees between the nozzle axis and normal to the ground board. The distance between the nozzle and ground in this case was measured along the extended axis of the nozzle. The distance between the trailing edge of the splitter plate and the ground was 1 inch. The white spot in Figure 5(b) resulted from wiping off an excess of lampblack and kerosene which accumulated at that point. Even for this relatively small angle of tilt, the flow pattern has changed considerably

9

from that obtained with the nonuniform jet impinging normally. The flow near the ground is appreciably thicker on the side furthest removed from the nozzle (right side of Figure 5(a)), and the stagnation ring has been broken on this same side (left side of Figure 5(b)). Although no quantitative measurements were made with the tilted jet, it is apparent from the pictures alone that the nonuniform jet is extremely sensitive to tilt angle. No check of the effect of tilt angle was made during the earlier uniform jet experiments, but it is believed, on the basis of the general experience gained in setting up conditions for normal flow impingement for both types of jets, that the uniform jet is not as sensitive as the nonuniform jet to small angles of tilt.

2. Quantitative Measurements

Tests were conducted on the nonuniform jet at ground-board locations corresponding to nozzle-height-to-nozzle-diameter ratios, H/D, of 4.07, 1.99 and 0.49. Most of the data were obtained with the settling chamber pressure held constant at 16 inches of water, which provided a maximum velocity near the outer edge of the jet of approximately 188 fps at the nozzle exit. Sample measurements were also made with a maximum jet velocity of 119 fps at the nozzle exit. At each H/D, velocity surveys were made at the nozzle exit and in the flow along the ground at various radial distances from the stagnation point up to a maximum of $r = 42$ inches. Static pressure distributions were measured along the jet centerline between the ground board and the jet nozzle and also along the ground board. The notation used in the presentation of the data is shown in Figure 6.

It was found that the flow at the nozzle-exit plane was somewhat irregular. A typical set of velocity data is shown in Figure 7. This figure shows the velocity measured along four radial lines at 90-degree

intervals in the exit plane of the nozzle for the jet exhausting into essentially free air. The data have been made nondimensional by a reference velocity U_R, which was chosen for experimental convenience and which is a reflection of the pressure in the settling chamber of the wind tunnel. The dashed line is an estimated mean curve drawn through the data. This curve was used to evaluate the momentum and mass flow of the jet. The accuracy of such a procedure can be judged by comparison of the jet momentum calculated from mean curves for different distances from the nozzle. The nondimensional jet momentum, $\frac{M}{\pi \rho R^2 U_R^2}$, calculated from the mean profile at the nozzle exit, was 0.302, as compared to 0.308 for $\frac{x}{b} = 2.02$. This is a difference of 2 percent, which is quite satisfactory.

It can be seen that the triangular velocity profile for which the shear screen was designed was only partially attained. In particular, the velocity at the outer edge of the jet deviates considerably from the desired distribution. The irregularities in this region are a consequence of insufficient nozzle length. A greater length of nozzle downstream of the shear screen would have allowed more mixing of the flow and, hence, smoothed out the velocity profile. The greater nozzle length was prohibited, however, by the space available for the tests.

The mean-velocity profiles in the free nonuniform jet measured at various distances from the nozzle are shown in Figure 8. The profile of a uniform jet with equal thrust is shown for comparison. The irregularities in the profiles disappeared rapidly with distance from the nozzle. At the same time the peak velocity in the jet moved toward the axis and decayed almost linearly with distance from the nozzle, while the velocity along the jet centerline increased. The behavior of the maximum velocity in the free jet and the velocity

on the jet centerline are shown in Figure 9. The decay of the maximum velocity for this particular nonuniform jet is represented quite well by the expression $-\dfrac{V_m}{U_R} = 0.695 - 0.0225 \dfrac{\xi}{R}$.

A comparison of the entrainment in the uniform and nonuniform jets is shown in Figure 10. In this figure the mass flow in each jet is plotted as a function of distance from the nozzle. The mass flow has been normalized by the value measured at the nozzle exit. When reduced in this way, the entrainment properties of the two jets appear to be identical. The dashed line is an empirical straight-line approximation to the data.

Figure 11 shows the velocity distributions at the nozzle for H/D = 4, 2, 1 and 0.5; the velocities are again normalized by the reference velocity U_R. The velocity distribution for H/D = 4 was essentially identical to that for H/D = ∞ . The effect of the proximity of the ground is most evident near the jet axis. Perhaps a better indication of the ground effect is given by Figure 12, where the static-pressure profiles at the nozzle are plotted. The pressures have been nondimensionalized by the settling chamber pressure, q_R . The static pressure difference was zero for H/D = 4 and ∞ . At H/D = 0.49, the non-dimensional static pressure on the jet axis reached a value of 0.25. This is approximately 50 percent of the maximum total pressure measured at the outer edge of the jet. There was some ground effect even at H/D = 1.99. The corresponding tests of the uniform jet showed no back pressure at H/ D = 2. The first evidence of ground effect in that case appeared at H/D = 1.

The static pressure distributions on the ground are presented in Figures 13(a) through 13(d). Data are shown for four radial lines separated by 90-degree intervals. The line θ = 270 degrees[*] is the

---

[*]See List of Symbols

one on which boundary-layer measurements were made. It is evident from the data that perfect axial symmetry was not attained in these experiments. There is a general tendency for the peak static pressure to be higher in the horizontal plane (θ = 90 and 270 degrees) than in the vertical plane (θ = 0 and 180 degrees). The position of the maximum static pressure coincided with the position of the stagnation ring in the flow visualization pictures as one might expect. The static pressure on the ground under the tilted nonuniform jet is shown in Figure 14. The plane corresponding to θ = 90 and 270 degrees is the one in which a 5-degree angle of tilt was imposed, with the line θ = 270 degrees being farthest from the nozzle. The break in the stagnation ring illustrated in Figure 5(b) is reflected in Figure 14 as a suppression of the peak in static pressure along the line θ = 270 degrees.

Figure 15 shows the static pressure distribution along the jet centerline as a function of nondimensional distance from the ground, z/D. Inspection of Figures 13 and 15 shows that the static pressure is approximately constant in the region surrounding the center of impingement, and, in addition, this constant pressure region is largest in extent for $H/D \approx 2$. These observations are in accord with the behavior of the jet as determined from the flow visualization pictures. The increase in static pressure along the jet axis near the ground at H/D = 4 over that at H/D = 2 is a reflection of the mixing process before impingement. The dynamic pressure on the centerline of the free jet increases with distance from the nozzle because of viscous mixing (Figure 8), and this increase causes a rise in static pressure recovery near the center of impingement.

TR 64-42

A brief hot-wire survey of the impingement region was performed for the normally impinging nonuniform jet with $H/D = 1.99$. The result of this survey is shown in Figure 16. The velocities shown are absolute velocities; the direction of the flow is not indicated by a single hot wire. This should be kept in mind when studying Figure 16. In particular, the flow visualization pictures indicated that the direction of the velocity along the jet axis near the board was perpendicular to and away from the board. The main point which can be determined from Figure 16 is that the velocity in the dome-shaped region of Figure 5(a) is only a small fraction of that found outside the dome and, hence, should not play an important role in the entrainment problem. There is, however, the possibility that particles entrained in the flow in higher velocity regions may be carried to the center of the impingement region by this secondary flow and deposited as a mound near the axis of symmetry of the flow.

Figure 17 presents velocity profiles in the flow along the ground at various radial stations in the turning region for $H/D = 0.49$, 1.99, and 4.07. A velocity profile measured inside the stagnation ring with $H/D = 1.99$ is included in Figure 17(b). Note that for radii near the stagnation ring, the maximum velocity is reached at a considerable height above the ground. Below this maximum velocity point, the velocity decreases gradually as the wall is approached until at a very small distance from the wall, the beginning of a true boundary layer is discernable. The region of increasing velocity between the very thin boundary layer and the maximum velocity is due to the static pressure difference between the wall and the outer edge of the flow. The decay in velocity at larger distances from the wall is due to viscous mixing. As the radius is increased to regions where the static pressure gradient at the wall

TR 64-42

approaches zero (see Figure 13), the velocity profiles rapidly approach
the fo m associated with the classical turbulent radial wall jet.

The experimental data for $H/D = 1.99$ and $r/D > 1$ are plotted as u/u_m
vs $y/y_{1/2}$ in Figure 18; $y_{1/2}$ is the distance to the point in the outer
mixing region at which $u = \frac{1}{2}u_m$ (see Figure 6). In general, the data
fall on a single curve when plotted in this way so long as the radius is
sufficiently large that the pressure gradient at the ground is approxi-
mately zero. Identical results were obtained for $H/D = 0.49$ and 4.07
with the exception that the minimum radius at which the data collapsed
to a wall-jet type of velocity profile changed with H/D. For each H/D,
the largest value of r/D indicated in Figure 17 is the smallest r/D at
which the wall-jet profile was obtained. The next smaller value of r/D
in each case followed the wall-jet profile in the outer portion of the flow
except for $H/D = 0.49$ (see, e. g., Figure 18, $r/D = 1.33$). Sample data
at a second, lower, value of mass flow in each case gave essentially
the same results when nondimensionalized. This is illustrated in Figure
18 for $r/D = 2.10$.

In Figure 19 the boundary layer region for the data of Figure 18 is
plotted on a greatly expanded scale. The comments made above apply
to Figure 19 as well.

TR 64-42

III THEORETICAL ANALYSES

A. Uniform Inviscid Impinging Jet Theory

A theory for the flow along the ground plane of an impinging jet, particularly for the boundary layer flow, requires, first, that the ground-plane pressure distribution be predicted. It was recognized that for free jets in air, viscous effects are important. However, the work reported in Reference 1 indicated that, for H/D less than approximately 2, the ground-plane pressure distribution under the uniform impinging jet was essentially that of the inviscid jet. Furthermore, the available theoretical results for inviscid impinging jets were not applicable for H/D less than 2. For H/D less than 2, as the jet exit approaches the ground plane, there is a back-pressure which is reflected at the exit in terms of reduced dynamic pressure in the center of the jet. Hence, the jet exit velocity profile is no longer uniform. As H/D is reduced below 2, there are, in addition, substantial changes in the ground-plane pressure distribution.

analysis of the uniform inviscid impinging jet was a continuation of the study partially reported in Reference 1. Work was brought to a conclusion during the present research. The analysis is based on a vortex sheet representation for the jet boundaries. The resultant mathematical model was programmed for an IBM 704 digital computer. An iterative technique was developed in which successive positions of the jet boundary were computed until the appropriate boundary conditions for the flow were satisfied. Details of the mathematical model and the implementation of this model on the computer are presented in Appendix II. For the sake of completeness, parts of the discussion of Reference 1 are repeated.

During the formulation stage of the analytical program, it was
realized that problems could arise concerning convergence of the
iterative technique which might be amplified by the approximations
inherent in any digital computer program for continuous systems.
Hence, the convergence properties were investigated from an experi-
mental point of view by a trial and error process. Fortunately, con-
vergence was ultimately attained.

Boundaries and flow properties were computed for $H/D = 1$ and
$H/D = 0.25$. The computed boundaries are shown in Figure 20,
where the results of Leclerc, Reference 3, for $H/D = 2$ (approxi-
mately equivalent to $H/D = \infty$, are shown for comparison. Computed
static pressure distributions along the jet centerline are shown in
Figure 21, and along the ground plane in Figure 22. Computed
velocity profiles and flow angularity with reference to the jet axis
at the nozzle are presented in Figure 23.

B. Boundary Layer Analysis

An approximate method of analysis was developed in Reference 1
which appeared to be adequate for predicting the flow along the
ground under an impinging uniform jet. The method was semi-
empirical in that it was based on the experimentally determined fact
that the mass flow along the ground could be made independent of
H/D (at least in the range $\frac{1}{4} \leq H/D \leq 4$) by a proper choice of non-
dimensionalizing parameters. In addition, the analysis required
knowledge of the pressure distribution along the ground. This latter
requirement was to be met by the inviscid solution to the problem of
the impinging uniform jet. Such a solution is reported in Section III (A).
Since this solution was not available at the time the boundary layer
analysis was performed, the experimental pressure distributions were
used in anticipation of the inviscid solution.

The problem became more difficult when an initially nonuniform jet was considered. Since a theoretical solution for the pressure distribution on the ground under such a jet was not available, it was necessary to restrict the analysis to regions of the flow where the pressure gradient is approximately zero. The logical procedure appeared to be to search for a correlation between the mass flow parameters of the uniform and nonuniform jets and to use such a correlation, if found, in conjunction with a simple momentum balance to describe the flow at radii sufficiently large for the pressure to have reached nearly ambient conditions. A method of analysis based on this correlation would then be applicable to both the uniform and the nonuniform jets.

A factor in favor of this procedure is that the velocity profiles near the ground in the nearly ambient pressure region can be found from Glauert's radial wall jet analysis (Reference 4). The turbulent flow solution is the one of interest for this investigation. The shape of the theoretical velocity profile was prescribed by a parameter α, which in turn depended weakly on the Reynold's number $\frac{u_m \delta_r}{\nu}$, where u_m is the local peak velocity in the radial flow and δ_r is the distance between the point at which $u = u_m$ and the point at which $u = \frac{1}{2} u_m$ (Figure 6).

It is desirable to obtain an estimate of α from the properties of the jet before impingement. Because of the weak dependence of α on $\frac{u_m \delta_t}{\nu}$, this can be accomplished with considerable accuracy even if some relatively broad assumptions are made. It was assumed that Glauert's theory applies for $r/R = 3$, that the loss in radial momentum flux due to skin friction is negligible at this radius, and that u_m equals the value of v_m in the free jet at a distance $t/R = H/R + (\frac{r}{R} - 1)$ where $\frac{r}{R} = 3$ for this calculation. A discussion of this method of estimating α has been presented in Appendix II of Reference 1 and will not be repeated here. The value $\alpha \approx 1.16$ computed in this manner compares very closely

with those derived from the experimental measurements of $\frac{u_m \delta_t}{y}$.

Once the shape of the velocity profile has been determined by α , the functional dependence of $y_{1/2}$ and u_m on r is given by

$$u_m / \bar{U}_m = C_u (r/R)^a; \quad y_{1/2}/R = C_y (r/R)^b \tag{1}$$

where the exponents "a" and "b" depend on the value of α , the constants C_u and C_y may be functions of H/D and the type of jet considered, and $\bar{U}_m$ is a reference velocity which will be defined shortly. The approximate determination of C_u and C_y forms the remaining portion of the analysis.

Consideration of the momentum in the jet provides one relation for finding the unknown constants C_u and C_y . Consider an impinging jet in which both the total and the static pressure distributions at the nozzle exit are functions of radius (Figure 24). If, for the moment, one artificially allows no mixing to occur, then one may say that the total pressure along any streamline will be a constant. Along any stream tube annulus (dotted line in Figure 24) in the impinging jet,

$$2\pi\rho \, v(r_N) r_N dr_N = 2\pi\rho \, r \, u(y) dy, \tag{2}$$

$P_T - P_A$ = constant in the streamtube and

$$v(r_N) = \sqrt{\frac{2[(P_T - P_A)_N - (P_S - P_A)_N]}{\rho}} \tag{3}$$

where the subscript N denotes that the quantities are evaluated at the nozzle exit plane. If one considers the flow along the ground where $P_S - P_A = 0$, then

$$u(y) = \sqrt{\frac{2(P_T - P_A)}{\rho}} = \sqrt{\frac{2(P_T - P_A)_N}{\rho}} , \tag{4}$$

Therefore from (2), (3), and (4),

$$dy = \frac{v(r_N) r_N dr_N}{r \, u(y)} = \frac{r_N}{r} \sqrt{\frac{(P_T - P_A)_N - (P_S - P_A)_N}{(P_T - P_A)_N}} \, dr_N$$

or

$$y = \int_0^{r_N} \frac{r_N}{r} \sqrt{1 - \left(\frac{P_S - P_A}{P_T - P_A}\right)_N} \, dr_N \quad \text{and} \quad u(y) = \sqrt{\frac{2[P_T(r_N) - P_A]}{\rho}} \, . \quad (5)$$

Note that the thickness of the flow, $Y_s(r)$, is obtained simply by replacing $\int_0^{r_N}$ with $\int_0^R$ in equation (5). The radial momentum flux at r is given by

$$M_r = 2\pi \rho r \int_0^\infty u^2 \, dy. \quad (6)$$

Substitution of equation (5) into (6) gives

$$M_r = 4\pi \int_0^R (P_T - P_A)_N \sqrt{1 - \left(\frac{P_S - P_A}{P_T - P_A}\right)_N} \cdot r_N \, dr_N \, , \quad (7)$$

which is the radial momentum flux in terms of conditions at the nozzle exit plane provided that the radial station considered is sufficiently far from the jet axis so that the pressure at the wall has become approximately atmospheric.

Since Equation (7) deals with momentum flux, it is valid for the flow under a real impinging jet even though entrainment was neglected in its derivation, provided that the momentum flux loss due to wall skin friction can be neglected. The momentum flux loss at the start of the wall-jet flow has been found experimentally to be small for all cases tested to date, so Equation (7) will be used in the following analysis.

It is convenient at this point to define two characteristic mean velocities based on conditions at the nozzle exit. These are a mean mass flow velocity $\bar{U} = \frac{2}{R^2} \int_0^R v \, r_N \, dr_N$

and a mean momentum velocity $\bar{U}_M \equiv \sqrt{\frac{2}{R^2} \int_0^R v_T \, v \, r_N \, dr_N}$ where $v_T = \sqrt{\frac{2(P_T - P_A)}{\rho}}$. With this definition of $\bar{U}_M$, Equation (7)

simplifies to

$$\frac{M_R}{\pi \rho R^2 \bar{U}_M{}^2} = 1 \quad \text{(skin friction neglected)} . \tag{7a}$$

An additional relationship is required to obtain the two unknowns, C_u and C_y, in Equation (1). In the tests of the uniform jet (Reference 1), this relation was obtained empirically. It was found that the radial mass flow, Q_r, in the wall-jet region was independent of H/D when plotted as $\frac{Q_r}{\pi \rho R^2 U_\infty}\left(\frac{U_\infty}{\bar{U}}\right)^{0.91} \bar{\omega}\frac{r}{R}$ where U_∞ is the velocity at the edge of the uniform jet. On reviewing the calculations for the uniform jet, however, a small error in the calculation of $\bar{U}/U_\infty$ from the experimental data was found for $H/D = 0.25$. The revised estimate of $\bar{U}/U_\infty$ became 0.56 as compared to the original estimate of 0.60. With this more accurate value for $\frac{\bar{U}}{U_\infty}$, the nondimensional mass flow parameter became $\frac{Q_r}{\pi \rho R^2 U_\infty}\left(\frac{U_\infty}{\bar{U}}\right)^{0.91}$. This revised parameter will be used in the following analysis. Application of the definition of $\bar{U}_M$ to the uniform jet (note $v_r = U_\infty$ for the uniform jet) shows that $\bar{U}_M = \sqrt{\bar{U}\, U_\infty}$, so that the equivalent mass flow parameter in terms of $\bar{U}_M$ is $\frac{Q_r}{\pi \rho R^2 \bar{U}_M}\left(\frac{\bar{U}_M}{\bar{U}}\right)^{0.14}$. The correlation of the experimental data for both the uniform and the nonuniform jets is illustrated in Figure 25.

The data for each type of jet correlate when plotted in this way, but there is 15 percent difference between the two sets of data. It is possible that some of the difference may be attributable to small deviations from axial symmetry in the tests of the nonuniform jet. Such deviations are noted in Section II. A further indication of asymmetry in the flow under the nonuniform jet is that the experimental radial momentum flux with $H/D = 4$ reached values up to 10 percent higher than is theoretically possible for an axisymmetric jet with no losses. Since the measurements in the flow along the ground were made only along one radial line, the results are subject to error if the flow is not accurately axisymmetric. In view of this uncertainty in the experimental results, it was decided that a weighted average of the two sets of data would be used to complement Equation (7a) in the

calculation of C_μ and C_y.

The variation of Q_r with r is prescribed by Glauert's form parameter α. For $\alpha = 1.16$, the theoretical values of a and b in Equation (1) are -1.075 and 1.008 respectively. However, the experimental values of a and b as found in the uniform jet tests proved to be better represented by $a = -1.143$ and $b = 1.028$. Since, in practice, the value of α is unlikely to differ very much from that found in the present work because of an insensitivity of α to nozzle Reynold's number, and the values of a and b in turn are only weakly dependent on α in this range, it was felt justified to assume that the experimental values of a and b were representative of all practical cases. Hence, $Q_r \sim u_m y_{1/2} r \sim (r)^{0.885}$. The relations

$$\frac{Q_r}{\pi \rho R^2 \bar{U}_M} \left(\frac{\bar{U}_M}{\bar{U}} \right)^{0.14} = 0.50 \left(\frac{r}{R} \right)^{0.885} \quad \text{for the uniform jet}$$

$$= 0.58 (r/R)^{0.885} \quad \text{for the nonuniform jet}$$

appear to give the best fit to the experimental data. A weighted average of these two curves, $\frac{Q_r}{\pi \rho R^2 \bar{U}_M} \left(\frac{\bar{U}_M}{\bar{U}} \right)^{0.14} = 0.52 \left(\frac{r}{R} \right)^{0.885}$, is used in the subsequent analysis. In arriving at this value, most of the emphasis was placed on the uniform jet data because it was believed that these data were the most accurate.

The following relations determine the flow near the ground:

$$\frac{M_r}{\pi \rho R^2 \bar{U}_M^2} \approx 1 \qquad\qquad \frac{r}{R} \leq \frac{r_t}{R} \qquad (7a)$$

$$\frac{Q_r}{\pi \rho R^2 \bar{U}_M} \left(\frac{\bar{U}_M}{\bar{U}} \right)^{0.14} \approx 0.52 \left(\frac{r}{R} \right)^{0.885} \qquad\qquad \frac{r}{R} \geq \frac{r_t}{R} \qquad (8)$$

and $\quad \frac{u_m}{U_M} = C_\mu \left(\frac{r}{R} \right)^{-1.143}, \quad \frac{y_{1/2}}{R} = C_y \left(\frac{r}{R} \right)^{1.028} \qquad \frac{r}{R} \geq \frac{r_t}{R} \qquad (1)$

where r_t is the radius where the wall-jet flow begins. Further, it will be assumed that at the start of the wall jet, u_m is equal to the maximum velocity in an equivalent free jet at a distance $\frac{t}{R} = \frac{H}{R} + \left(\frac{r_t}{R} - 1 \right)$

TR 64-42

from the nozzle exit. For the two jets tested, the above assumption gives

uniform jet: $\frac{u_m}{U_\infty} = 1$ at $\frac{r_t}{R}$ provided $H/D \leq 4$

nonuniform jet:
(see Figure 9) $\frac{u_m}{U_M} = \left[0.695 - 0.0225\left(\frac{H}{R} + \frac{r_t}{R} - 1\right)\right] / \frac{U_M}{U_R}$ at $\frac{r_t}{R}$ $\left.\begin{array}{c} \\ \\ \\ \\ \end{array}\right\}$ (9)

where U_R is a reference velocity used for experimental convenience and is representative of the wind tunnel settling chamber pressure.

The method of solution for C_u and C_y is as follows. From Equation (7(a)) one obtains

$*$ $1.53 \left(\frac{u_m}{U_M}\right)^2 \frac{y_{1/2}}{R} \frac{r}{R} = \frac{M_r}{\pi \rho R^2 \bar{U}_M^2} \approx 1$ for $\frac{r}{R} = \frac{r_t}{R}$

and, since $u_m / \bar{U}_M$ has been assumed in this region, then

$$\frac{y_{1/2}}{R} \approx \frac{1}{1.53} \left(\frac{u_m}{U_M}\right)^{-2} \left(\frac{r}{R}\right)^{-1} \quad \text{for} \quad \frac{r}{R} = \frac{r_t}{R} \quad (10)$$

and $*$ $\frac{Q_r}{\pi \rho R^2 \bar{U}_M} \approx 2.22 \frac{u_m}{\bar{U}_M} \frac{y_{1/2}}{R} \frac{r}{R} = 1.45 \left(\frac{u_m}{\bar{U}_M}\right)^{-1}$ for $\frac{r}{R} = \frac{r_t}{R}$

or $\frac{Q_r}{\pi \rho R^2 \bar{U}_M} \left(\frac{\bar{U}_M}{\bar{U}}\right)^{0.14} = 1.45 \left(\frac{u_m}{\bar{U}_M}\right)^{-1} \left(\frac{\bar{U}_M}{\bar{U}}\right)^{0.14}$ for $\frac{r}{R} = \frac{r_t}{R}$. (11)

The combination of Equations (8) and (11) gives

$$1.45 \left(\frac{u_m}{U_M}\right)^{-1} \left(\frac{\bar{U}_M}{\bar{U}}\right)^{0.14} \approx 0.52 \left(\frac{r_t}{R}\right)^{0.885} \quad (12)$$

which may be solved for r_t/R with the aid of Equation (9), or its equivalent if other jet profiles are of interest.

Once r_t/R has been found, then C_u and C_y are given by

$$C_u = \left(\frac{u_m}{U_M}\right)_t \left(\frac{r_t}{R}\right)^{1.143} ; \quad C_y = \left(\frac{y_{1/2}}{R}\right)_t \left(\frac{r_t}{R}\right)^{-1.028} . \quad (13)$$

$*$ The numerical constants in these equation were obtained by integration of the theoretical velocity profiles, That is,

$Q_r = 2\pi \rho r u_m y_{1/2} \int_0^\infty \left(\frac{u}{u_m}\right) d\left(\frac{y}{y_{1/2}}\right) \approx 2.22 \pi \rho r u_m y_{1/2}$ for $1.1 \leq \alpha \leq 1.2$

and

$M_r = 2\pi \rho r u_m y_{1/2} \int_0^\infty \left(\frac{u}{u_m}\right)^2 d\left(\frac{y}{y_{1/2}}\right) \approx 1.53 \pi \rho r u_m^2 y_{1/2}$ for $1 \leq \alpha \leq 1.6$.

Equations (1), (9), (10), (12) and (13) along with Glauert's velocity profile for $\alpha = 1.16$ constitute a complete description of the flow along the ground in the region where the wall static pressure gradient approaches zero. The solution may be applicable for radii slightly less than r_ϕ. The flow near the ground at $r \cdot r_\phi$ will have a minimum in thickness and an approximate maximum in velocity, and hence this is probably the radius where the entrainment problem will be most severe.

The results of the calculations are presented in Figures 26 and 27 for the uniform and nonuniform jets respectively.

IV COMPARISON OF THEORY AND EXPERIMENT,
AND DISCUSSION OF RESULTS

A. Inviscid Impinging Uniform Jet Analysis

Computed jet boundaries are presented in Figure 20 for $H/D = 1.0$
and $H/D = 0.25$. Also shown is the boundary derived by Leclerc from
an electric analog tank experiment for $H/D = 2$. Comparison of these
computed boundaries with experimental data is not possible, because
the experimental jet boundaries are obscured by viscous mixing. It
is apparent from Figure 20 that as H/D decreases, the theoretical
thickness of the jet above the ground plane decreases. This was inferred
in Reference 1 from mass flow considerations. As H/D decreases,
the equivalent uniform velocity, U , in the tube (or nozzle) also decreases.
Conservation of mass requires that at some distance along the ground
plane from the stagnation point, where the pressure has fallen to near
ambient pressure,

$$Y_s(r) \approx \frac{R^2 U}{2r U_\infty} \tag{14}$$

which is Equation (1) of Reference 1 ; $Y_s(r)$ is the height of the jet
boundary above the ground plane. Equation (14) is consistent with
Equation (5), Section III B, which applies generally for impinging jets
with no mixing.

Computed static pressure distributions along the jet centerline and along
the ground plane are compared with corresponding experimental results
from Reference 1 in Figures 21 and 22 respectively. It is apparent that
excellent agreement was obtained,   although computed ground plane
pressures are slightly low for $0.7 < \frac{r}{R} < 1.4$ at $H/D = 1.0$. The small
discrepancies probably reflect the effects of viscosity (mixing), in view
of the excellent agreement obtained for the ground plane pressure dis-
tribution at $H/D = 0.25$, and for the jet centerline pressure distribution

for H/D = 1.0. Comparison of computed and experimental velocity profiles at the nozzle are shown in Figure 23. Again, agreement is good, particularly for H/D = 0.25. Also shown in Figure 23 is the computed variation of flow angularity at the nozzle with reference to the jet axis for H/D = 0.25. Of interest is the fact that the computed angularity is as large as 18.5° in this particular instance.

Of those values of H/D for which experimental data are available from Reference 1, the H/D = 0.25 case is the one most critically affected by the ground. The excellent agreement with experimental results for H/D = 0.25 clearly demonstrates the accuracy of the theory.

Convergence of the iteration process was relatively slow. The H/D = 1.0 computation required approximately 70 iterations and about 4 hours of computing time on the CAL IBM 704 computer. The iteration technique involves so-called "gain" constants (See Equation (II-5) of Appendix II). The appropriate gain constants for convergence must be determined by trial and error. If they are too large, successive curves computed as the iteration program proceeds tend to oscillate through larger and larger amplitudes which ultimately diverge violently. For somewhat smaller values, the oscillations become damped, and the program ultimately converges. If the "gain" constants are reduced still more, the successively computed curves tend to approach the solution asymptotically. Apparently, there is an optimum "gain" constant which is analogous to critical damping and for which convergence will be obtained most rapidly. Unfortunately, a detailed investigation of this point was not believed to be practicable during the present program. Once "gain" constants were determined for which the successive iterations showed a converging solution, these constants were used thereafter, and the program was permitted to run to convergence.* It is believed that the

---

* An improved iteration technique which should provide much more rapid convergence is outlined in Appendix II.

convergence criterion used in these computations insures an accuracy
of between three and four significant figures in the final computed curve,
within the approximations inherent in the IBM program.

As a partial check on the accuracy of the computing program, absolute
velocities just inside the free-jet boundary at the control points were
computed. If the solution were exact, these velocities would all be equal
to U_∞ . For H/D = 1.0, for the five control points, these velocities
for the converged solution varied from 0.93 to 0.99 of U_∞, with three of the
five being within 3 percent of U_∞ . For H/D 0.25, these velocities
varied from 0.96 to 1.06 of U_∞, with three of the five within 3 percent of
U_∞ . Largest deviations from U_∞ occurred for the control points
closest to the nozzle, and hence closest to regions where shape approxi-
mations have been used. It is believed that these results could be
improved by using more control points, and by using a finer breakdown
for numerical integration purposes. This can be done easily, but at
the expense of increased computer running time.

Another indication of the accuracy of the analysis is provided by
Figure 28, in which the absolute velocity is plotted versus distance
from the ground plane for H/D = 1.0 at r/R = 1.7. The absolute velocity
outside the jet should be zero for the correct jet boundary and correct
area vorticity density distribution. For the computed points shown
in Figure 28, velocities outside the boundary are less than 0.01 U_∞ ;
the calculations also show the abrupt change in velocity across the jet
boundary which should be obtained theoretically.

A detailed investigation of the various approximations in the program
as they affect the computed results was believed to be unnecessary for
the present program in view of the excellent agreement between computed
and experimental pressure distributions. However, it is hoped that such

an investigation will be made because of the potential application of the general technique employed in this analytical program to other axially symmetric, three-dimensional, free-streamline flows.

B. Boundary Layer Analysis

Because of the complexity of the flow in the turning region under the impinging nonuniform jet, the analysis of the flow along the ground was restricted to those regions where the pressure gradient at the wall became approximately zero. Such a restriction required a treatment which was somewhat different from that presented for the uniform jet in Reference 1. The properties of the wall-jet portion of the flow for both the uniform jet and the nonuniform jet were computed using the method of analysis presented in this report. The uniform jet analysis predicts that the wall-jet velocity profiles should be given by Glauert's theory for $\alpha = 1.16$. It was shown in Reference 1 that the velocity profiles obtained with the uniform jet were in excellent agreement with Glauert's theory for $\alpha = 1.16$, and consequently these data will not be reproduced herein.

The experimental velocity profiles in the wall-jet region of the nonuniform jet with $H/D = 1.99$ are shown in Figure 18 along with the velocity profiles predicted by Glauert for values of $\alpha = 1.1$ and 1.2. These results are typical of the data obtained for all values of H/D tested. The appropriate value of α was found to be 1.16 in Section III B. The accuracy of the predicted profile is somewhat less than it was for the uniform jet. The portion of the data shown in Figure 18 would appear to be best represented by a value of α slightly less than 1.1 except in the range $y/y_{w/2} > 1.2$. The divergence from the theory at large values of $y/y_{w/2}$ was found also in the uniform jet work and by other experiments and is probably due to a combination of angularity of the flow with respect to the probe and the decreasing accuracy of the measurements at the very low velocities encountered.

The boundary layer region of Figure 18 is plotted in Figure 19. The theoretical profile for $\alpha = 1.16$ has been added to this figure. In this region, the experimental data are reasonably well represented by the curve for $\alpha = 1.16$ except at values of $\frac{r}{b} \leq 1.33$, where the pressure gradient increases rapidly. The curve for $\alpha = 1.16$ has been modified from Glauert's theory to account for the laminar sublayer. As in Reference 1, the outer edge of the laminar sublayer is in the region $\frac{y}{y_{vz}} \approx 0.015$. The theoretical profile was modified by matching the inner portion of the universal velocity distribution for smooth pipes (Figure 20.4 of Reference 5) to Glauert's profile at $\frac{y}{y_{vz}} = 0.015$.

The fact that slightly different values of α appear to be required in the boundary layer and outer regions of the velocity profile for agreement with the experimental results may be due to the deviations from radial symmetry discussed earlier, especially since the uniform jet tests, where the radial symmetry was excellent, provided extremely good agreement with the theoretical wall-jet profiles. The small deviations from theory in these velocity profiles constituted no serious problem in the calculation of u_m and $y_{1/2}$ in Section III, since the numerical values of the integrals for nondimensional mass flow and momentum used in the analysis are almost independent of α in the range of α which is applicable to the problem.

The calculated values of u_m/u_∞ and $\frac{y_{1/2}}{R}$ for the uniform jet are compared to the experimental data in Figure 26(a) and 26(b) respectively. As shown, the over-all accuracy is quite satisfactory; the difference between theory and experiment never exceeds 10 percent and is generally closer. The effect of varying H/D is to reduce the radius at which the apparent wall-jet flow starts. A similar comparison between theory and experiment is made in Figure 27(a) and 27(b) for the nonuniform jet. In Figure 27(a) u_m has been nondimensionalized by $\bar{U}_\omega$ and divided by 2

The factor $\frac{1}{2}$ is used only for convenience in presenting the results on logarithmic graph paper. Note that the sample data obtained at a second value of nozzle mass flow (solid symbols) are essentially the same as those obtained at the mass flow used for the bulk of the tests. Again the accuracy of the approximate analysis is satisfactory except near the start of the wall-jet flow at $H/D = 1.99$. In this case the assumption that the maximum velocity at the start of the wall jet can be approximated by the velocity in the free jet at an equivalent distance from the nozzle was not realized, although the use of this assumption provided reasonable results for radii slightly larger than that corresponding to the start of the wall-jet flow. The error in predicting $\frac{y_{1/2}}{R}$ for the nonuniform jet is somewhat larger than that for the uniform jet. This is primarily due to the higher emphasis placed on the uniform jet data when estimating the mass flow parameter. Generally, the radii for which the calculated results disagreed most with the experimental data coincided with the turning region of the jet as defined by the ground static pressure distributions of Figure 13. Since it was assumed in the analysis that the jet was completely turned, such results are not unexpected. Unfortunately, the extent of the turning region of the nonuniform jet at $H/D = 1.99$ is larger than the apparent radius for the start of the wall jet, and the calculated properties are in error in this region. The error is on the conservative side so that the use of the method of analysis will at least provide an upper limit to the seriousness of the entrainment problem even in this case.

It is evident from the experimental results and from the analysis that the lack of a method for predicting the flow along the ground in the turning region of the jet is not a serious limitation. In all cases except $H/D \approx 2$ with the nonuniform jet, the method of analysis provides reasonably accurate estimates of the properties of the flow along the ground at the start of the wall-jet flow. Since this radius corresponds to an approximate maximum in velocity and a minimum in thickness of the flow,

it will in all probability, from what is known about particle entrainment, be the region most critical to the entrainment problem.

C. Comparison of Boundary Layer Under Uniform and Nonuniform Jet

In Section III B, experimental properties of the flow along the ground under both jets were compared to the results of an approximate analysis. Application of this analysis requires a knowledge of the conditions at the nozzle as a function of H/D as well as the free air velocity decay curve of each jet. However, the properties of non-uniform jets at values of H/D sufficiently small that there is a ground effect at the nozzle $(H/D \lesssim 2)$ are not predictable by current theoretical techniques. Hence, it would appear advisable to compare directly the two types of jets to discover if the results from the uniform jet can be applied to the nonuniform jet at these low values of H/D. At higher values of H/D, there is no static pressure rise at the nozzle so that these cases require only a knowledge of the free air properties of the jet being considered. The comparison will be made on the basis of constant thrust per unit nozzle area.

The above basis for comparison poses no problem in the comparison of $\frac{y_{v_2}}{R}$ for both types of jets. The results shown in Figures 26(b) and 27(b) as $\frac{y_{v_2}}{R}$ versus $\frac{r}{R}$ are independent of thrust, so they can be compared directly. In the range of H/D covered by the experiments and for $\frac{r}{R} \gtrsim 4$, the two sets of data are essentially the same if one allows for probable errors in the nonuniform jet data due to slight flow asymmetry. The results of the two analyses are almost identical for the cases $H/D = \frac{1}{2}$ and 2 over the complete range of $\frac{r}{R}$ shown. This indicates that, as far as the prediction of $\frac{y_{v_2}}{R}$ is concerned, the uniform jet analysis can be applied directly to the nonuniform jet in the range $H/D \leq 2$. The result for the nonuniform jet will be in error at $H/D \approx 2$ for $\frac{r}{R}$ near the start of the wall-jet flow for the reasons discussed previously in the

comparison of theory and experiment. At H/D = 4, and in the range $r/R < 4$, both the experimental and analytical results indicate that the two jets are not comparable, the flow under the uniform jet being thinner than that under the nonuniform jet. Hence, for $H/D > 2$, the decay in maximum velocity in the nonuniform jet must be accounted for if reasonably accurate predictions are to be obtained.

In order to compare the maximum velocity near the ground generated by the two jets, it is necessary first to convert the results presented in Figures 26(a) and 26(b) to $\frac{u_m}{\sqrt{T/\rho A}}$, where T is the thrust and A is nozzle area (πR^2). For the uniform jet, this is done by expressing the thrust in terms of $\overline{U}/U_\infty$. It can be shown that

$$\frac{T}{\pi \rho R^2 U_\infty^2} = \frac{1}{2}\left[1 + \left(\frac{\overline{U}}{U_\infty}\right)^2\right] \tag{15}$$

and hence

$$\frac{u_m}{\sqrt{T/\rho A}} = \frac{u_m}{U_\infty}\sqrt{\frac{2}{1 - \left(\frac{\overline{U}}{U_\infty}\right)^2}}$$

The variation of $\frac{\overline{U}}{U_\infty}$ with H/D is shown in Figure 29, for a uniform jet.[*] The limit of $\frac{\overline{U}}{U_\infty}$ as H/D approaches zero was calculated from considerations of two-dimensional inviscid flow through a sluice gate. Since u_m/U_∞ reached a maximum value of approximately 1 at the start of the wall jet for all $H/D \leq 4$, the maximum velocity reached at the ground is simply $\quad \frac{u_m}{\sqrt{T/\rho A}} = \sqrt{\frac{2}{1 + \left(\frac{\overline{U}}{U_\infty}\right)^2}}$

for the uniform jet. The value of $u_m/\sqrt{\frac{T}{\rho A}}$ is shown in Figure 30 for both the uniform jet and the nonuniform jet. The points for the latter were taken directly from Figure 27(a) because the experimental data for the nonuniform jet indicated that, in the range $H/D \geq \frac{1}{2}$,

[*] Figure 29 may also be used to obtain an estimate of the thrust variation with constant power input for an axially symmetric, uniform, impinging jet. Using Equations (14) and (15) and the requirement that power remain constant, one can show $\frac{T}{T_{H=\infty}} = \frac{1}{3}\left(\frac{U_\infty}{U}\right)^{2/3}\left[1 + \left(\frac{\overline{U}}{U_\infty}\right)^2\right]$ for constant power. This equation plus Figure 29 may be used to calculate the variation of $T/T_{H=\infty}$ as a function of H/D.

$\overline{\dfrac{T}{\pi \rho R^2 \bar{U}_M}} t = 1$ and hence $u_m / \sqrt{\dfrac{T}{\rho A}} - u_m / \bar{U}_M$. The points shown are
the calculated velocity at the start of the wall jet (break in the curves of
Figure 27(a)).

It can be seen that the uniform jet analysis provides results for
$\dfrac{u_m}{\sqrt{\dfrac{T}{\rho A}}}$ identical to those obtained with the nonuniform jet analysis in
the range $H/D \leq 2$. In view of this result and the corresponding results
for $y_{1/2}/R$, it can be assumed with reasonable certainty that the
uniform jet analysis can be applied to calculate the properties of the
flow along the ground under nonuniform jets for values of $H/D \leq 2$.
The results of the analysis will of course be valid only for radii suffi-
ciently large that the flow has been completely turned. At values of
$H/D \leq 2$, the velocity decay characteristic of the nonuniform jet ex-
hausting into free air must be included in the analysis.

A general comparison of both the analytical and the experimental results
for the two jets provides the following features. At values of $H/D \lesssim 1$,
the flows along the ground under the two jets are essentially the same.
The limit $H/D \lesssim 1$ rather than $\frac{1}{2}$ is stipulated, even though quantitative
measurements of the flow along the ground were not obtained with
the nonuniform jet at $H/D = 1$. Flow visualization pictures and the
ground static pressure distribution obtained at $H/D = 1$ indicated that
the effective turning radius of the jet was sufficiently small as to cause
no such problems as those observed at $H/D = 2$. At values of $H/D > 1$,
the flow along the ground under the nonuniform jet had a lower maximum
velocity and larger thickness than that under the uniform jet. These
differences were not large, but they do provide the unexpected result
that the nonuniform jet is slightly less prone to cause particle entrain-
ment at large values of H/D, and is no worse than the uniform jet
at small values of H/D.

BIBLIOGRAPHY

1. Brady, W. G., and Ludwig, G. R.,   Theoretical and Experimental
    Studies of Impinging Uniform Jets,   TRECOM TR 63-11,
    April 1963.

2. Brady, W. G., and Ludwig, G . R., "Theoretical and Experi-
    mental Studies of Impinging Uniform Jets", Journal of the
    American Helicopter Society,   Vol. 8, No. 2,   April 1963,
    pp. 1 - 13.

3. LeClerc, A.,   Deflection of a Liquid Jet by a Perpendicular
    Boundary, M.S. Thesis,   State University of Iowa,   1948.

4. Glauert, M. B.,   "The Wall Jet", Journal of Fluid Mechanics,
    Vol. 1, Part 6,   December 1956 ,   p. 625.

5   Schlichting, H. ,   Boundary Layer Theory, Fourth Edition,
    McGraw Hill Book Company, New York,   1960.

6. Milne-Thompson, L. M.,   Theoretical Hydrodynamics,
    Second Edition,   The MacMillan Company, New York ,   1950.

APPENDIX I

GENERAL COMMENTS
ON THE FLOW VISUALIZATION PICTURES

Splitter Plate Pictures

The streamline patterns obtained on the splitter plates must not be taken as an exact picture of the flow which would occur in the absence of such a plate. Since a surface has been inserted in the flow, there will be a boundary layer developed on this surface. In general, the combined thickness of the plate and the displacement thicknesses of the boundary layers developed on each side of the plate will be a negligible fraction of the jet diameter, so that this thickness will have little effect on the flow outside the boundary layer. However, in regions where there is a pressure gradient in the flow (close to the ground in this case), the effe   of the pressure gradient on the flow in the boundary layer will be to   celerate or decelerate mostly that portion of the air with the least kinetic energy. This is, of course, the region adjacent to the surface, the one instrumental in producing the streamline patterns

The net effect of the pressure gradients in the flow near the ground will be twofold. First, near the jet centerline the adverse pressure gradient occurring as the ground is approached will separate the boundary layer. Such behavior was observed in the uniform jet tests and is the reason why the trailing edge of the splitter plate was kept at least 6 inches from the ground board. In this case the flow in the core of the jet was essentially free of turbulence and the velocity at which the tests were conducted was sufficiently low so as to sustain a laminar boundary layer near the jet axis and hence to provide a high

susceptibility to separation. With the nonuniform jet, the turbulence
in the flow probably caused a forced transition to a turbulent boundary
layer near the plate leading edge. The higher resistance of a turbulent
boundary layer to separation and the less adverse pressure gradients
observed with this jet explain the absence of separation in the flow
pictures which were made with the trailing edge of the splitter plate
only 1 inch from the ground board.

The second effect is that of the pressure gradient in the radial direction
in the absence of separated flow. In this case, the flow in the boundary
layer very near the wall will be turned more than that in the free stream,
again because of the difference in kinetic energy. This will show up in
the flow pictures as an exaggerated turning of the flow near the ground
and possibly an increased apparent thickness of the radial outflow along
the ground. The portions of the flow patterns in the center of the
impingement region under the nonuniform jet should be least affected
by the interaction of boundary layer and radial pressure gradient, as
this region appeared to be at roughly constant pressure.

The above comments apply only to the patterns obtained on the splitter
plates. The conclusions to be drawn are that the patterns must be
regarded as providing only an approximate picture of the flow in any
region where the streamline patterns show a large curvature, with the
possible exception of flow in the center of the impingement area under
the nonuniform jet.

Ground Flow Pictures

The streamline patterns shown reflect the flow in the boundary layer
along the ground. Since the surface used to obtain the patterns is in the
flow at all times and is not an additional surface as with the splitter
plate, the resulting streamline pattern is reasonably representative of

the actual flow, except for a gravity effect. The board was mounted vertically in these tests; hence, in regions where the flow velocity was low, gravity caused the lampblack and kerosene mixture to flow downward. This is especially apparent in the center of the impingement region where, in some cases, there is a pronounced downward curvature to all of the streamlines.

APPENDIX II

DETAILS OF UNIFORM INVISCID IMPINGING JET ANALYSIS

A. Derivations of Equations for Inviscid Impinging Jet Flow Basic Formulation

Consider a Cartesian coordinate system with the z-axis directed along the axis of symmetry of the flow, positive vertically up from the ground plane, and the x-y plane ($z = 0$) coincident with the ground plane. Consider an element of volume $d\tau(x',y',z')$ with vorticity vector $\zeta(x',y',z')$. For vorticity distributed throughout a given volume V, one can write the vector velocity, $\bar{q}$, at any point (x, y, z) in the fluid as (Reference 6)

$$\bar{q}(x,y,z) = \frac{1}{4\pi} \int_V \frac{\bar{\zeta}(x',y',z') \times \bar{d}}{|\bar{d}|^3} \, d\tau(x',y',z') \tag{II-1}$$

where

$$\bar{d} = (x-x')\hat{\imath} + (y-y')\hat{\jmath} + (z-z')\hat{k}$$

and $\hat{\imath},\hat{\jmath},\hat{k}$ are unit vectors in the x, y, and z directions, respectively. In the case of axially symmetric flow,

$$\bar{\zeta} = \zeta_x \hat{\imath} + \zeta_y \hat{\jmath} \ .$$

The transformation to cylindrical coordinates (r, z, θ) where

$$x = r \cos\theta \ , \qquad y = r \sin\theta$$

and

$$\zeta_x = \zeta_0 \sin\theta \ , \qquad \zeta_y = -\zeta_0 \cos\theta$$

gives

$$\bar{\zeta} \times \bar{d} = \zeta_0 \left[-\hat{\imath}_r (z-z') \cos\theta - \hat{\jmath}_\theta (z-z') \cos\theta + \hat{k}_z (r \cos\theta - r') \right]$$

and

$$|\vec{d}|^3 = \left[(z-z')^2 + r^2 + (r')^2 - 2rr'\cos\theta'\right]^{3/2}$$

where $\hat{\imath}_r$, $\hat{\jmath}_\theta$ and $\hat{k}_z$ are unit vectors in the r, θ and z directions, respectively. Because of axial symmetry, only the $\theta = 0$ plane need be considered.

Substituting in Equation (II-1) and equating vector components, we have

$$u = -\frac{1}{4\pi}\int_V \frac{\zeta_0(r',z')(z-z')\cos\theta' \, d\tau(r',z',\theta')}{\left[(z-z')^2 + r^2 + (r')^2 - 2rr'\cos\theta'\right]^{3/2}}$$

(II-2)

$$v = \frac{1}{4\pi}\int_V \frac{\zeta_0(r',z')(r\cos\theta'-r') \, d\tau(r',z',\theta')}{\left[(z-z')^2 + r^2 + (r')^2 - 2rr'\cos\theta'\right]^{3/2}}$$

$$v_\theta = 0$$

where u, v are the velocity components parallel to the r-axis and the z-axis, respectively, and v_θ is the velocity component perpendicular to the meridian plane. The integration is taken over the volume V, which includes all the distributed vorticity of intensity $\zeta_0(r,z)$.

Consider now the vorticity distributed in a thin layer on the edge of the jet. Consider a given element of volume, $d\tau$, of this layer (Figure 31) whose projection on the meridian plane is ϵds, where ϵ is the infinitesimal thickness of the layer and ds is the length of the element along the curve $r = r_0(z)$ which defines the edge of the jet. From Stoke's theorem (Reference 6, page 46) for a circuit C in the meridian plane enclosing the projection of $d\tau$, we have

$$\int_{S'} \bar{n}\cdot\bar{\zeta}\,dA = \int_C \bar{q}\cdot d\bar{s}$$

where $\bar{n}$ is the unit outward normal vector to the surface enclosed by C, S' is the area enclosed by C, and $\bar{q}$ is the velocity vector around C. The integral on the right-hand side is taken in the

clockwise direction.   Then

$$\int_{S'} \bar{n} \cdot \bar{\zeta} \, dA = \zeta_0 \epsilon \, ds$$

$$\int_C \bar{q} \cdot \overline{ds} = (q_1 - q_2) \, ds \; ;$$

hence,

$$\zeta_0 \epsilon = q_1 - q_2$$

where q_1 and q_2 are as shown in Figure 31. If we let $\epsilon \to 0$, $\zeta_0 \to \infty$ such that

$$\zeta_0 \epsilon = \xi, \quad \text{a constant}$$

then

$$\xi = q_1 - q_2 \; .$$

Also,

$$\zeta_0 \, d\tau = \zeta_0 \epsilon r_0 \, ds \, d\theta'$$

$$= \xi r_0(z') \sqrt{1 + \left[\frac{dr_0(z')}{dz}\right]^2} \, dz' d\theta' \; .$$

Thus, Equation (II-2) can be written

$$u(r,z) = \frac{1}{4\pi} \int_S \frac{\zeta(z') r_0(z') \sqrt{1 + \left[\frac{dr_0(z')}{dz}\right]^2}(z - z') \cos \theta' \, dz' \, d\theta'}{\left[(z-z')^2 + r^2 + [r_0(z')]^2 - 2rr_0(z) \cos \theta'\right]^{3/2}}$$

(II-3)

$$v(r,z) = \frac{1}{4\pi} \int_S \frac{\zeta(z') r_0(z') \sqrt{1 + \left[\frac{dr_0(z')}{dz}\right]^2}[r \cos \theta' - r_0(z')] \, dz' \, d\theta'}{\left[(z-z')^2 + r^2 + [r_0(z')]^2 - 2rr_0(z') \cos \theta'\right]^{3/2}}$$

where the integration is carried out over the entire vortex sheet S .

The Boundary Conditions for Infinite Impinging Jet

The boundary conditions on the inviscid impinging jet flow are as follows:
Along the surface, $z = 0$, $v = 0$. Along the jet boundary which is a
free streamline, the velocity is equal to a constant; therefore,
ξ is also constant, as just outside the jet the velocity is zero.

To satisfy the boundary condition that $\nu = 0$ for $z = 0$, the plane $z = 0$ is made a plane of symmetry for the impinging jet and its image. Hence, the integration over S, Equation (II-3), must be carried out over two vortex sheets, that defining the impinging jet and that for the image jet.

The Boundary Conditons for Jet Nozzle at Finite Height Above the Ground

The jet is assumed to issue from a straight tube of constant diameter (Figure 32) at finite height, H, above the ground. A free-stream surface issues from the edge of the jet exit, B in Figure 32, such that the free streamline velocity vector at B is parallel to the side of the tube. The flow inside the tube along the side of the tube must be tangential to the side; but, of course, the streamline along this side is no longer a free streamline, as a pressure difference can exist and, hence, the magnitude of the edge velocity may vary. The boundary condition along the edge of the tube is, then, that the normal component of velocity, u, is zero. In addition, at B in Figure 32, ν is continuous. Again, along the free streamline BC, the velocity and, hence, ξ are constant.

Final Form for Velocity Components

Figure 32 illustrates the flow model as thus far developed. The straight tube of constant diameter, D, centered on the z-axis extends from z = H to z = ∞. For $0 < z < H$, the curve $r = r_0(z)$ defines the edge of the jet. To insure that ν is tangential at B in Figure 32, we require that $\dfrac{dr_0}{dz} = 0$ at z = H; that is, there is no discontinuity in slope between the side of the nozzle and the free-stream surface. The sides of the tube and the jet are represented

by a vortex sheet of vorticity $\bar{\xi}(r_0,z)$ per unit area whose r- and z-components are zero. The image of this vortex system for $\theta > z > -\infty$ assures that the boundary condition (no normal flow) along OD is satisfied.

The integrations with respect to θ' can be done in closed form in each of the integrals of Equation (II-3). If this is done, and we let $z = \bar{z}R$, $z' = \bar{z}'R$, $r = \bar{r}R$, $r_0 = \bar{r}_0 R$ and $\zeta = \bar{\zeta}\xi(H)$, there results

$$u(\bar{r},\bar{z}) = -\frac{\xi(H)}{2\pi\bar{r}}\left\{\int_{\frac{H}{R}}^{\infty} \frac{\bar{\xi}(\bar{z}')(\bar{z}-\bar{z}')}{\sqrt{(\bar{z}-\bar{z})^2+(\bar{r}+1)^2}}\left[\frac{(\bar{z}-\bar{z}')^2+\bar{r}^2+1}{(\bar{z}-\bar{z})^2+(\bar{r}-1)^2}E(k_1)-K(k_1)\right]d\bar{z}'\right.$$

$$-\int_{\frac{H}{R}}^{\infty} \frac{\bar{\xi}(\bar{z}')(\bar{z}+\bar{z}')}{\sqrt{(\bar{z}+\bar{z}')^2+(\bar{r}+1)^2}}\left[\frac{(\bar{z}+\bar{z}')^2+r^2+1}{(\bar{z}+\bar{z}')^2+(\bar{r}-1)^2}E(k_2)-K(k_2)\right]d\bar{z}'$$

$$+\int_{0}^{\frac{H}{R}} \frac{[\bar{z}-\bar{z}']\sqrt{1+\left[\frac{d\bar{r}_0(\bar{z}')}{d\bar{z}}\right]^2}}{\sqrt{[\bar{z}-\bar{z}]^2+[\bar{r}+\bar{r}_0(\bar{z})]^2}}\left\{\frac{[\bar{z}-\bar{z}']^2+\bar{r}^2+[r_0(\bar{z}')]^2}{[\bar{z}-\bar{z}']^2+[\bar{r}-\bar{r}_0(\bar{z}')]^2}E(k_3)-K(k_3)\right\}d\bar{z}'$$

$$\left.-\int_{0}^{\frac{H}{R}} \frac{[\bar{z}+\bar{z}']\sqrt{1+\left[\frac{d\bar{r}_0(\bar{z}')}{d\bar{z}}\right]^2}}{\sqrt{[\bar{z}+\bar{z}']^2+[\bar{r}+\bar{r}_0(\bar{z}')]^2}}\left\{\frac{[\bar{z}+\bar{z}']^2+r^2+[r_0(\bar{z}')]^2}{[\bar{z}+\bar{z}']^2+[\bar{r}-\bar{r}_0(\bar{z}')]^2}E(k_4)-K(k_4)\right\}d\bar{z}'\right\}$$

$$v(\bar{r},\bar{z}) = \frac{\xi(H)}{2\pi}\left\{\int_{\frac{H}{R}}^{\infty} \frac{\bar{\xi}(\bar{z}')}{\sqrt{(\bar{z}-\bar{z}')^2+(\bar{r}+1)^2}}\left[\frac{(\bar{z}-\bar{z}')^2+\bar{r}^2-1}{(\bar{z}-\bar{z}')^2+(\bar{r}-1)^2}E(k_1)-K(k_1)\right]d\bar{z}'\right.$$

$$-\int_{\frac{H}{R}}^{\infty} \frac{\bar{\xi}(\bar{z}')}{\sqrt{[\bar{z}+\bar{z}']^2+[\bar{r}+1]^2}}\left[\frac{(\bar{z}+\bar{z}')^2+\bar{r}^2-1}{(\bar{z}+\bar{z}')^2+(\bar{r}-1)^2}E(k_2)-K(k_2)\right]d\bar{z}'$$

$$+\int_{0}^{\frac{H}{R}}\sqrt{\frac{1+\left[\frac{dr_0(\bar{z}')}{d\bar{z}}\right]^2}{(\bar{z}-\bar{z}')^2+[\bar{r}+\bar{r}_0(\bar{z}')]^2}}\left[\frac{(\bar{z}-\bar{z}')^2+\bar{r}^2-[r_0(\bar{z}')]^2}{(\bar{z}-\bar{z}')^2+[\bar{r}-\bar{r}_0(\bar{z}')]^2}E(k_3)-K(k_3)\right]d\bar{z}'$$

$$\left.-\int_{0}^{\frac{H}{R}}\sqrt{\frac{1+\left[\frac{d\bar{r}_0(\bar{z}')}{d\bar{z}}\right]}{(\bar{z}+\bar{z}')^2+[\bar{r}+\bar{r}_0(\bar{z}')]^2}}\left[\frac{(\bar{z}+\bar{z})^2+r^2-[\bar{r}_0(\bar{z}')]^2}{(\bar{z}+\bar{z}')^2+[\bar{r}-\bar{r}(\bar{z}')]^2}E(k_4)-K(k_4)\right]d\bar{z}'\right\} \qquad (II-4)$$

where $K(k)$ is the complete elliptic integral of the first kind and $E(k)$ is the complete elliptic integral of the second kind, with modulus k ; also,

$$(k_1)^2 = \frac{4\bar{r}}{(\bar{z}-\bar{z}')^2+(\bar{r}+1)^2} \quad , \qquad (k_2)^2 = \frac{4\bar{r}}{(\bar{z}+\bar{z}')^2+(\bar{r}+1)^2}$$

$$(k_3)^2 = \frac{4\bar{r}\bar{r}_0(\bar{z}')}{(\bar{z}-\bar{z}')^2+[\bar{r}+\bar{r}_0(\bar{z}')]^2} \quad , \qquad (k_4)^2 = \frac{4\bar{r}\bar{r}_0(\bar{z})}{(\bar{z}+\bar{z}')^2+[\bar{r}+\bar{r}_0(\bar{z}')]}$$

These integrals are valid everywhere except on the boundaries, at $(1,\bar{z})$ for $\bar{z} \geq \frac{H}{R}$ and $(\bar{r}_0(\bar{z}),\bar{z})$ for $\bar{z} \leq \frac{H}{R}$, where the integrands are singular. However, even on the boundaries, it can be shown that the Cauchy principal values of these integrals exist.

Equations (II-4) enable the velocity at any point in the flow to be computed, once the form of $\bar{r}_0(\bar{z})$, the curve defining the boundary of the jet, and $\bar{\xi}(\bar{z})$, the vorticity area density of the vortex sheet on the boundary of the jet and the tube, are known.

Equations (II-4) with the associated boundary conditions

$$\lim_{\bar{r} \to 1} u(\bar{r},\bar{z}) = 0, \quad \bar{z} \geq H/R, \quad \bar{r} < 1$$

$$\lim_{\bar{r} \to \bar{r}_0} \frac{u(\bar{r},\bar{z})}{v(\bar{r},\bar{z})} = \frac{d\bar{r}_0(\bar{z})}{d\bar{z}}, \quad \bar{z} \leq H/R, \quad \bar{r} < \bar{r}_0$$

give rise to simultaneous nonlinear integral equations for $\bar{\xi}(\bar{z})$ and $\bar{r}_0(\bar{z})$, which, as they stand, do not admit of solution in closed form. However, by means of a high-speed, large-capacity digital computer, a solution might be possible if a convergent iterative process can be derived which will permit the determination of the jet boundary $\bar{r}_0(\bar{z})$.

43   TR 64-42

B. Details of IBM 704 Computer Program

The general computational procedure adopted is as follows:

1. An initial shape of the free-streamline boundary is assumed.
2. The boundary condition that the flow at the wall of the tube is parallel to the tube is used to determine the varying area vorticity density of the vortex sheet representing the tube and the constant area vorticity density of the free-stream surface vortex sheet.
3. The flow normal to the free-stream surface is then evaluated; if there is a velocity normal to the boundary assumed for the free-stream surface, that assumed boundary is incorrect and must be adjusted.
4. The iteration proceeds for the adjusted boundary (by going back to step 1).

The boundary condition at the wall of the tube, step 2, is satis-fied at a discrete number of points, or values of ξ , along the tube. The nondimensional area vorticity density, $\bar{\xi}(\xi)$ in Equation (II-4), is assumed to be a constant within the increment $\Delta\xi$ centered on each of these points (but, of course varying from point to point). The first two integrals in the expression for ν, Equations (II-4), can then be expressed as a sum. Setting ν= 0 at each of the specified values of ξ , there results a series of linear, simultaneous equations in the unknown $\bar{\xi}(\xi)$. For ξ large enough, $\bar{\xi}(\bar{\xi})$ approaches a constant limiting value, and this fact is utilized to limit the number of simultaneous equations which must be solved. It happens that if $\bar{\xi}(\xi)$ is a constant, the first two integrals in the equation for ν in Equations (II-4) can be integrated explicitly, which eases the numerical integration process on the computer and also lends considerably to the accuracy with which ν can be computed.

BLANK PAGE

In practice, the value of $\mathcal{Z}$ at which $\bar{\xi}(\mathcal{Z})$ approaches a constant is initially guessed at, and then adjusted after initial runs have been made. The computed distributions of $\bar{\xi}(\mathcal{Z})$ do not appear to vary significantly with variations in the assumed jet boundary for a given H/D, at least for the two cases computed in the present work.

The process of determining the revised jet boundary in step 3 is based on the boundary condition along the jet boundary free stream lines, that the velocity normal to the boundary is zero. For example, if the computed velocity normal to the jet boundary is directed outward, this intuitively would suggest that the assumed boundary should be displaced outward. Let the curve for the assumed free jet boundary BC (Figure 32) for the ith repetition of steps 1 through 3 be

$$(\bar{r}_0)_i = [\bar{r}_0(\mathcal{Z})]_i .$$

Once the distribution of the vorticity in the vortex sheet is known from step 2, above, it is possible to compute the velocity vector anywhere in the flow, based on $(\bar{r}_0)_i$, the assumed free-stream surface boundary using Equations (II-4). The velocity components $u(\bar{r}_0, \bar{z})$, $v(\bar{r}_0, \mathcal{Z})$ at the boundary are computed; then $[u(\bar{r}_0, \bar{z})/v(\bar{r}_0/\bar{z})]$ is the slope of the velocity vector along the ith assumed boundary. If this slope is equal to $d(\bar{r}_0)_i/d\bar{z}$ all along the assumed boundary, $(\bar{r}_0)_i$ is the correct curve, as all boundary conditions are then satisfied. If not, we let

$$[\bar{r}_0(\bar{z})]_{i+1} = [\bar{r}_0(\bar{z})]_i - K \left\{ \frac{u(\bar{r}_{0i}, \mathcal{Z})}{v(\bar{r}_{0i}, \bar{z})} - \frac{d[r_0(\bar{z})_i}{d\bar{z}} \right\}, \qquad (II-5)$$

where K is a constant, called the "gain" constant. It should be noted that no mathematical rigor is claimed for this procedure; it is primarily a systemization of the method which a computer might use to adjust boundaries in a successive approximation technique. Convergence can, thus far, be determined only by a trial and error process. Several iterations are made with a selected value of the

constant. If the successive boundaries appear to be diverging, then successively smaller values of K are used until convergence is obtained.

Although the integrations indicated in Equations (II-4) are all taken with respect to the coordinate $\bar{z}$, in actuality the integrals with limits of integration from 0 to H/R were broken up into several integrals; see Figure 33. In region I, the integration is with respect to $\bar{z}$ between the limits $\bar{z}_0$ and H/R. For regions II, III, and IV, the integral is transformed so that integration is with respect to $\bar{r}$, with limits as shown in Figure 33. In each of the noted regions, breakdowns for purposes of numerical integration can be varied individually.

Certain assumptions and approximations are involved in the actual computer program. Equation (II-5) is applied at each iteration at specified values of $\bar{r}$, called "control points, " in regions II and III in Figure 33. These control points may or may not coincide with values of $\bar{r}$ used in numerical integrations. Once the jet boundary at the control points has been adjusted in accordance with Equation (II-5), increments are added to the jet boundary curve; these increments vary linearly between the control points and match the increments at the control points computed from Equation (II-5). The value of $\bar{r}_i$ is kept as close to unity as possible, consistent with accuracy of integration. Variation of $\bar{r}_0 (\bar{z})$ between $\bar{z} = \bar{z}_0$ and $\bar{z} = H/R$ is based on the variation of $\bar{g}(\bar{r})$ at the control point closest to $\bar{r}_i$, although the shape is determined by the initial assumed curve. For $\bar{r} > \bar{r}_j$, the shape of $\bar{g}(\bar{r})$ is assumed to vary as $C/\bar{r}$, with C a constant, determined from Equation (14). Integration is cut off at $\bar{r}_\psi$; the value of $\bar{r}_\psi$ is made as large as necessary so as not to affect the accuracy of velocities computed at the control points. The computations for which results are presented in this report were made with five control points. For H/D= 1.0, $\bar{r}_i = 1.2$ and $\bar{r}_j = 4.4$; for H/D = 0.25, $\bar{r}_i = 1.05$ and $\bar{r}_j = 4.5$. In both cases, $\bar{r}_\psi = 50$.

C. Outline of a Possible Improved Iteration Technique

Consider the flow tangency boundary condition on the free streamline

$$u(\bar{r}_0, \bar{z}) - \frac{d\bar{r}_0(\bar{z})}{d\bar{z}} v(\bar{r}_0, \bar{z}) = 0. \tag{II-6}$$

For an assumed free-streamline curve $(\bar{r}_0)_a$ other than that for the exact solution, there would result

$$u((\bar{r}_0)_a, \bar{z}) - \frac{d(\bar{r}_0)_a}{d\bar{z}} v((\bar{r}_0)_a, \bar{z}) = E(\bar{z}). \tag{II-7}$$

For purposes of numerical integration on a digital computer, the integrals constituting u and v are evaluated by computing the integrand at specific values of $\bar{z}$, say, $\bar{z}_i$, and summing the results by an appropriate rule such as Simpson's rule. On this basis, Equation (II-7) can be stated $(at\ \bar{z} = \bar{z}_n)$

$$\sum_{i=0}^{M} \Delta u_i \left((\bar{r}_0)_{ai} ; (\bar{r}_0)_{an}, \bar{z}_n \right) \tag{II-8}$$

$$- \frac{d(\bar{r}_0)_{an}}{d\bar{z}} \sum_{i=0}^{M} \Delta v_i ((\bar{r}_0)_{ai} ; (\bar{r}_0)_{an}, \bar{z}_n) = E_n(\bar{z}_n). \tag{II-9}$$

Now, let

$$(\bar{r}_0)_{ai} = (\bar{r}_0)_i + (\Delta \bar{r}_0)_i$$

where $(\bar{r}_0)_i$ is the exact value of $\bar{r}_0$ at $\bar{z} = \bar{z}_i$ and $(\Delta \bar{r}_0)_i$ is the incremental error in $(\bar{r}_0)_{ai}$ at $\bar{z} = \bar{z}_i$. If Equation (II-9) is substituted in Equation (II-8) and the terms Δu_i , Δv_i are expanded to first order in $(\Delta \bar{r}_0)_i$, there results

$$\sum_{i=0}^{M} \left[\overline{\Delta u_i}((\bar{r}_0)_i ; (\bar{r}_0)_n, \bar{z}_n) \right] (\Delta \bar{r}_0)_i$$

$$- \frac{d(\bar{r}_0)_n}{d\bar{z}} \sum_{i=0}^{M} \left[\overline{\Delta v_i}((\bar{r}_0)_i ; (\bar{r}_0)_n, \bar{z}_n) \right] (\Delta \bar{r}_0)_i$$

$$\approx E_n(\bar{z}_n), \qquad\qquad \text{for } n = 0 \text{ to } M$$

$$\tag{II-10}$$

where equation (II-1) has been applied; $\overline{\Delta u}_i$, $\overline{\Delta v}_i$ are the coefficients of the first-order terms in $(\Delta \bar{r}_0)_i$ of the expansions of Δu_i, Δv_i . Equation (II-10) for $n=0$ to $n=m$ results in $M+1$ linear, simultaneous algebraic equations in the $M+1$ unknowns $(\Delta \bar{r}_0)_i$; $i=0$ to M. However, the $(\bar{r}_0)_i$ are also unknown; hence, the substitution

$$(\bar{r}_1)_i \approx (\bar{r}_0)_{ai}$$

is made in Equation (II-10).

This is the basis of the proposed iteration scheme. The initial assumed shape of the free-streamline boundary $\left[(\bar{r}_0)_{ai} \right]_0$ is used in Equation (II-7) to compute $E_n(\bar{z}_n)$, and the $M+1$ equations resulting from Equation (II-10) (with Equation (II-11) included) are solved for the $M+1$ $\left[(\Delta \bar{r}_0)_i \right]_0$. The process is repeated with

$$\left[(\bar{r}_0)_{ai} \right]_1 = \left[(\bar{r}_0)_{ai} \right]_0 - \left[(\Delta \bar{r}_0)_i \right]_0 .$$

The iteration proceeds until all the $\left[(\Delta \bar{r}_0)_i \right]_j$ are as small as desired.

Whether convergence is obtained at all undoubtedly depends on how close the assumed boundary is to the exact boundary. However, there seems to be no question that if convergence were obtained by the iteration method actually used during the present calculations (empirically determined "gain constant," Equation (II-5)), convergence would be obtained much more rapidly by the method proposed here. It is noted that if all $(\Delta \bar{r}_0)_i$ except $(\Delta \bar{r}_0)_n$ had been assumed to be zero, then an analytic expression for the empirical "gain constant" (Equation (II-5)) would result. Hence, such a value of K_n at each $\bar{z}_n$ would undoubtedly be an optimum value for most rapid convergence using Equation

(II-5). However, the proposed method based on Equations (II-10) and (II-11) should result in even faster convergence. Unfortunately, this method was devised too late in the present research to be incorporated in the IBM 704 program. It is hoped that in the near future, there will be opportunity to employ the method in the solution of a different problem.

DIRECTION
OF FLOW

DIRECTION
OF FLOW
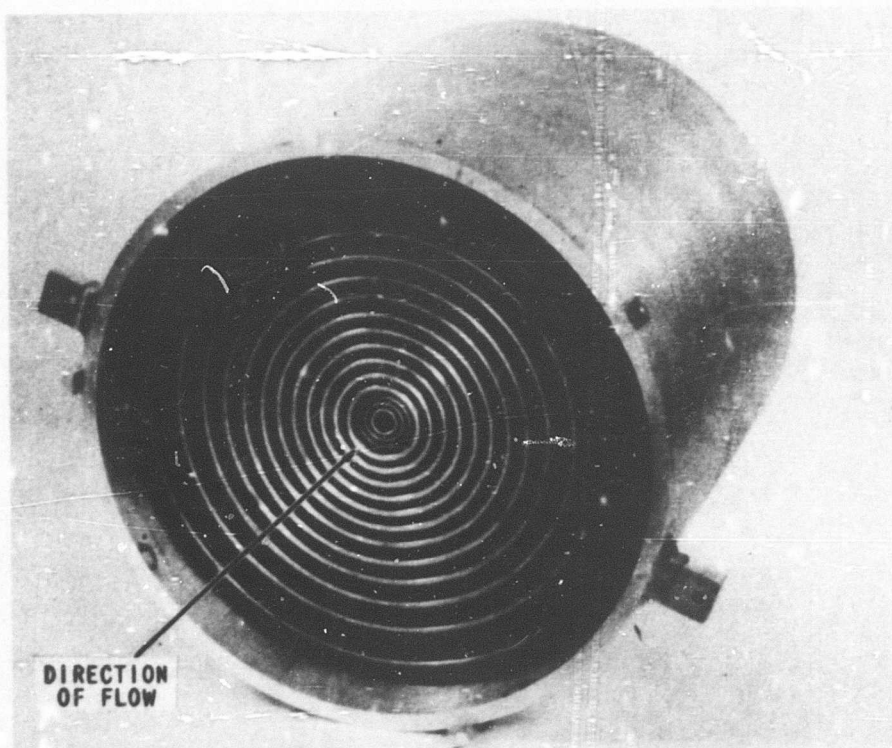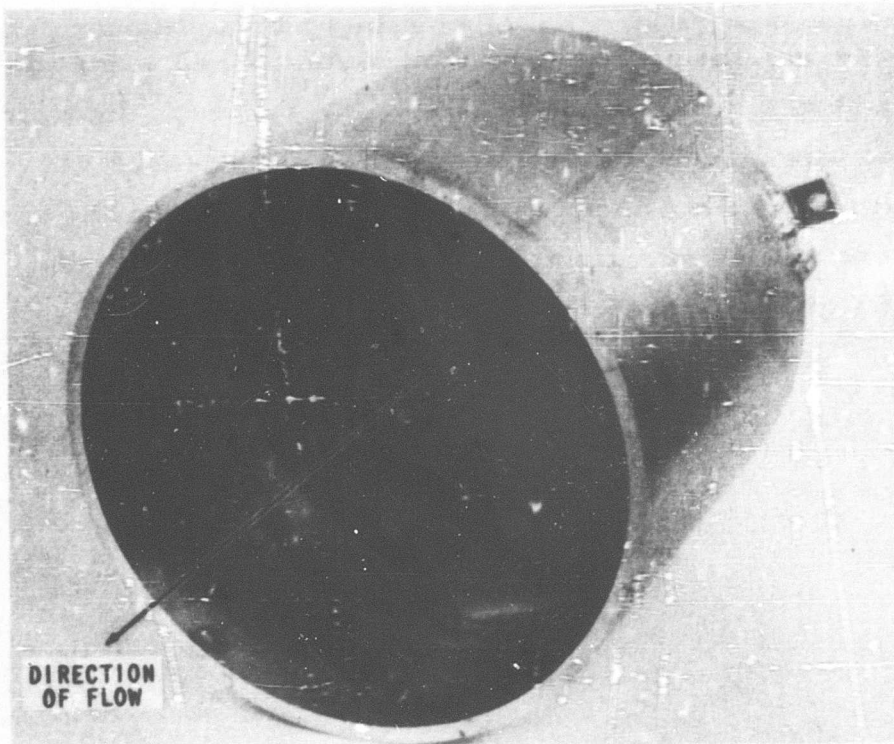
3268

Figure 1   SHEAR SCREEN ASSEMBLY

TR 64-42
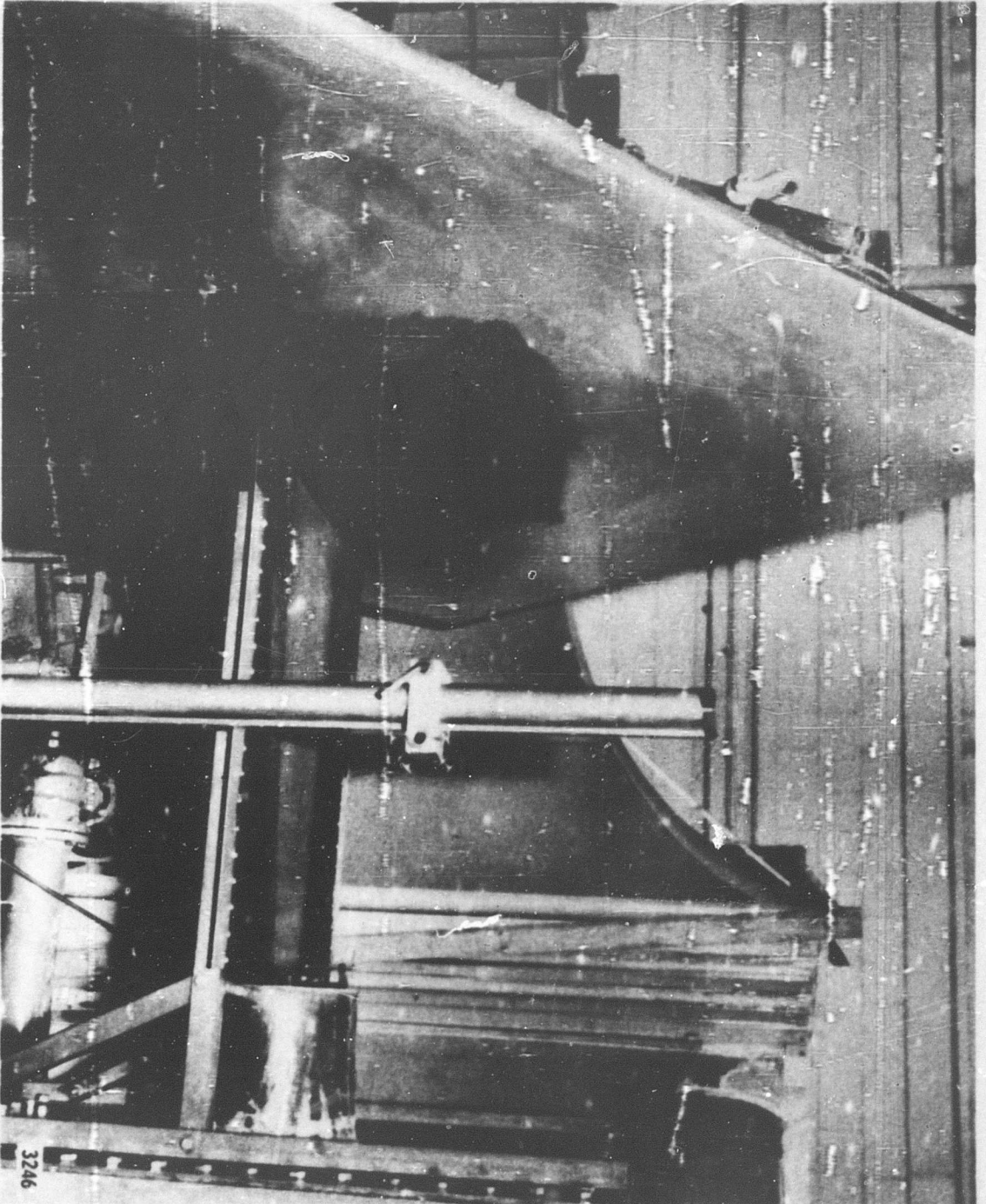
Figure 2 FLOW VISUALIZATION APPARATUS
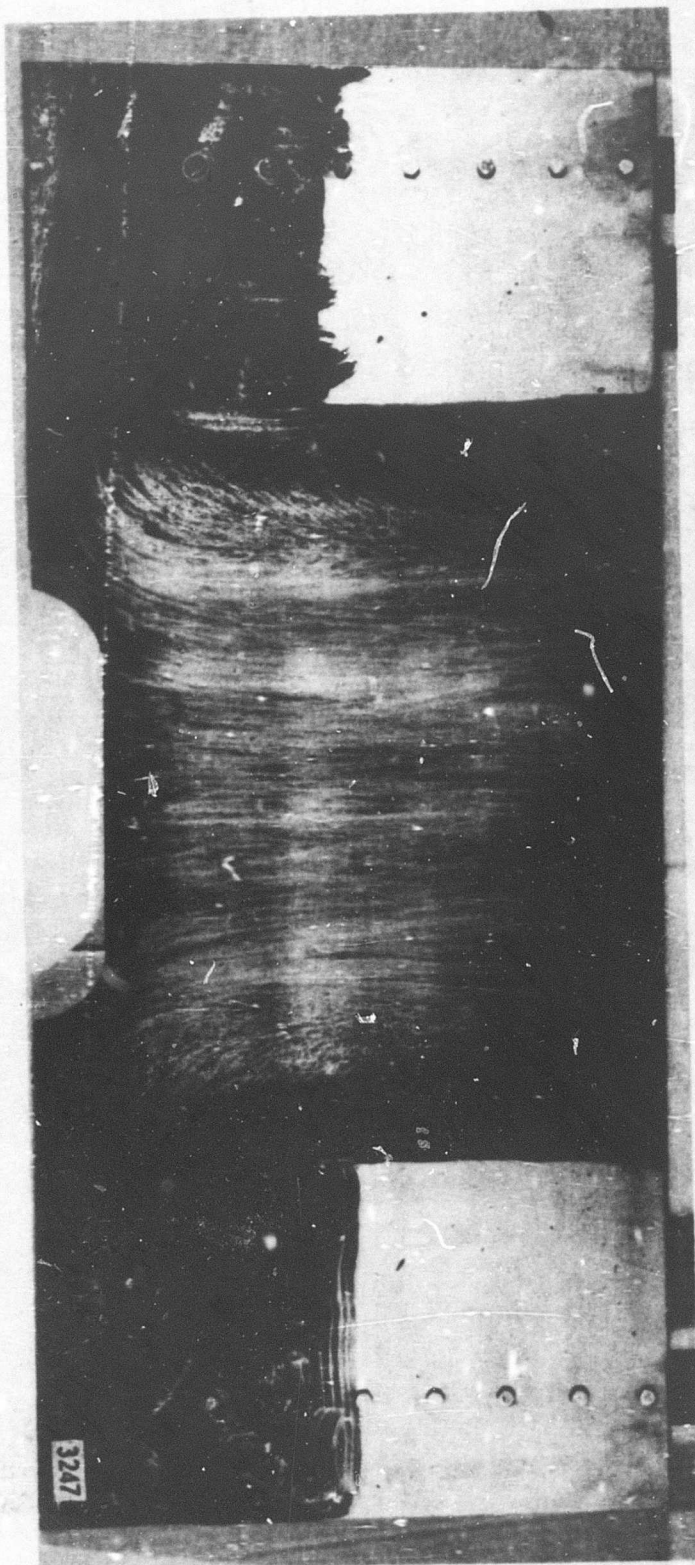
Figure 3 FLOW IN PLANE OF SYMMETRY OF NORMALLY IMPINGING UNIFORM JET, H/D = 2
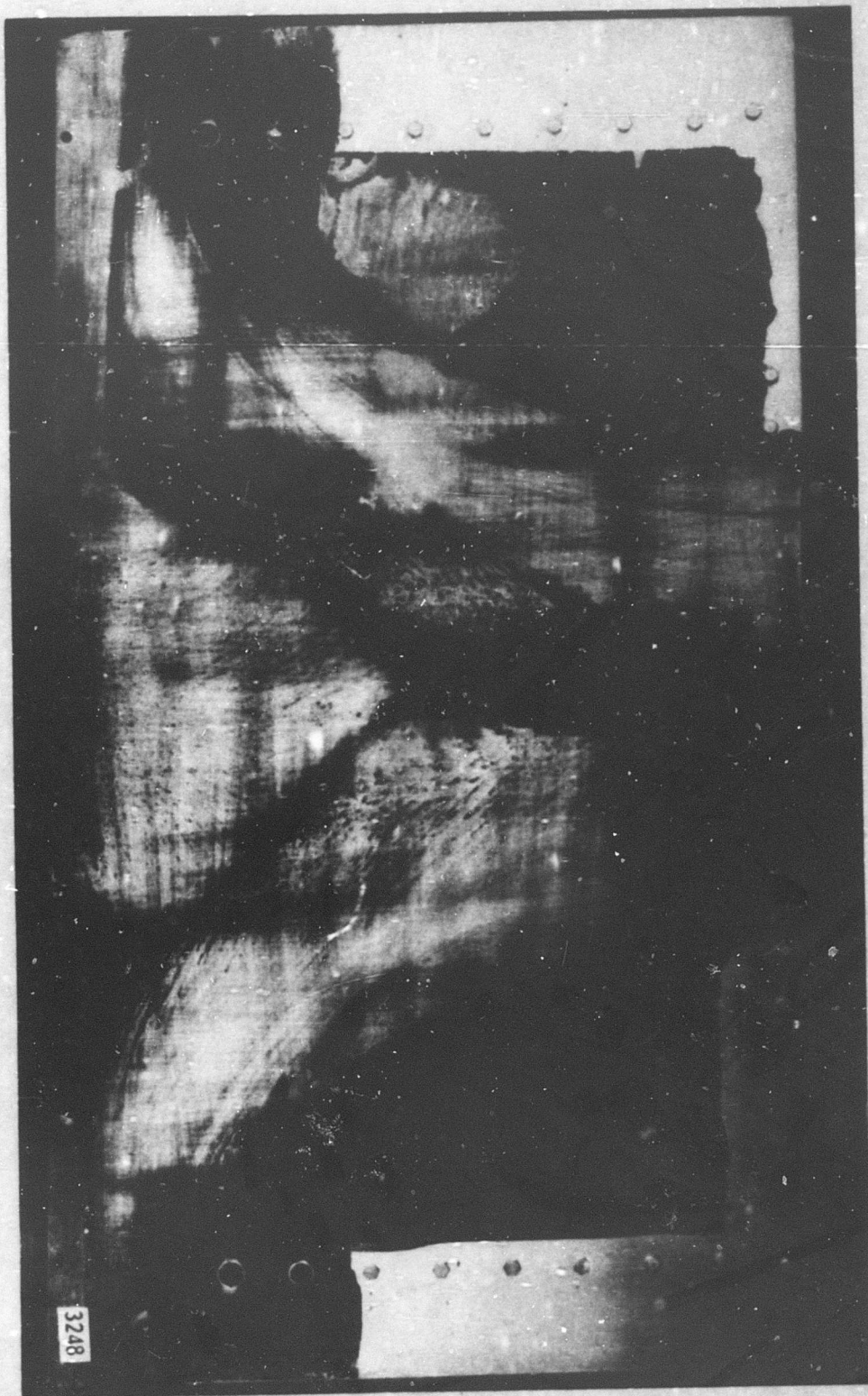
Figure 4 FLOW VISUALIZATION PICTURES OF NORMALLY IMPINGING NONUNIFORM JET, H/D = 1.99

(a) FLOW IN PLANE OF SYMMETRY
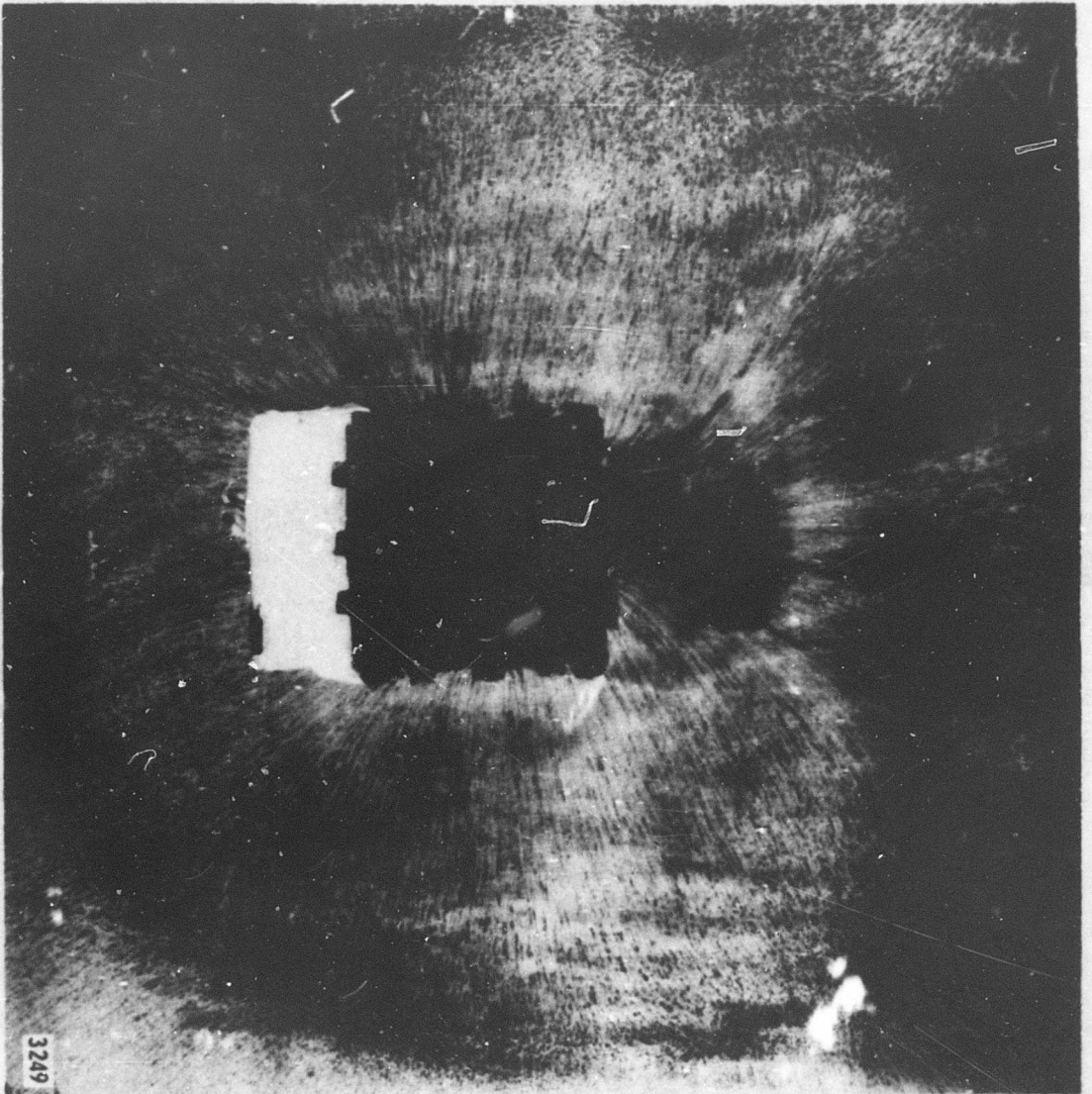
Figure 4 FLOW VISUALIZATION PICTURES OF NORMALLY IMPINGING NONUNIFORM JET, H/D = 1.99
(b) FLOW ALONG GROUND

Figure 5 FLOW VISUALIZATION PICTURES OF TILTED IMPINGING NONUNIFORM JET, H/D = 1.99
(a) FLOW IN PLANE OF SYMMETRY
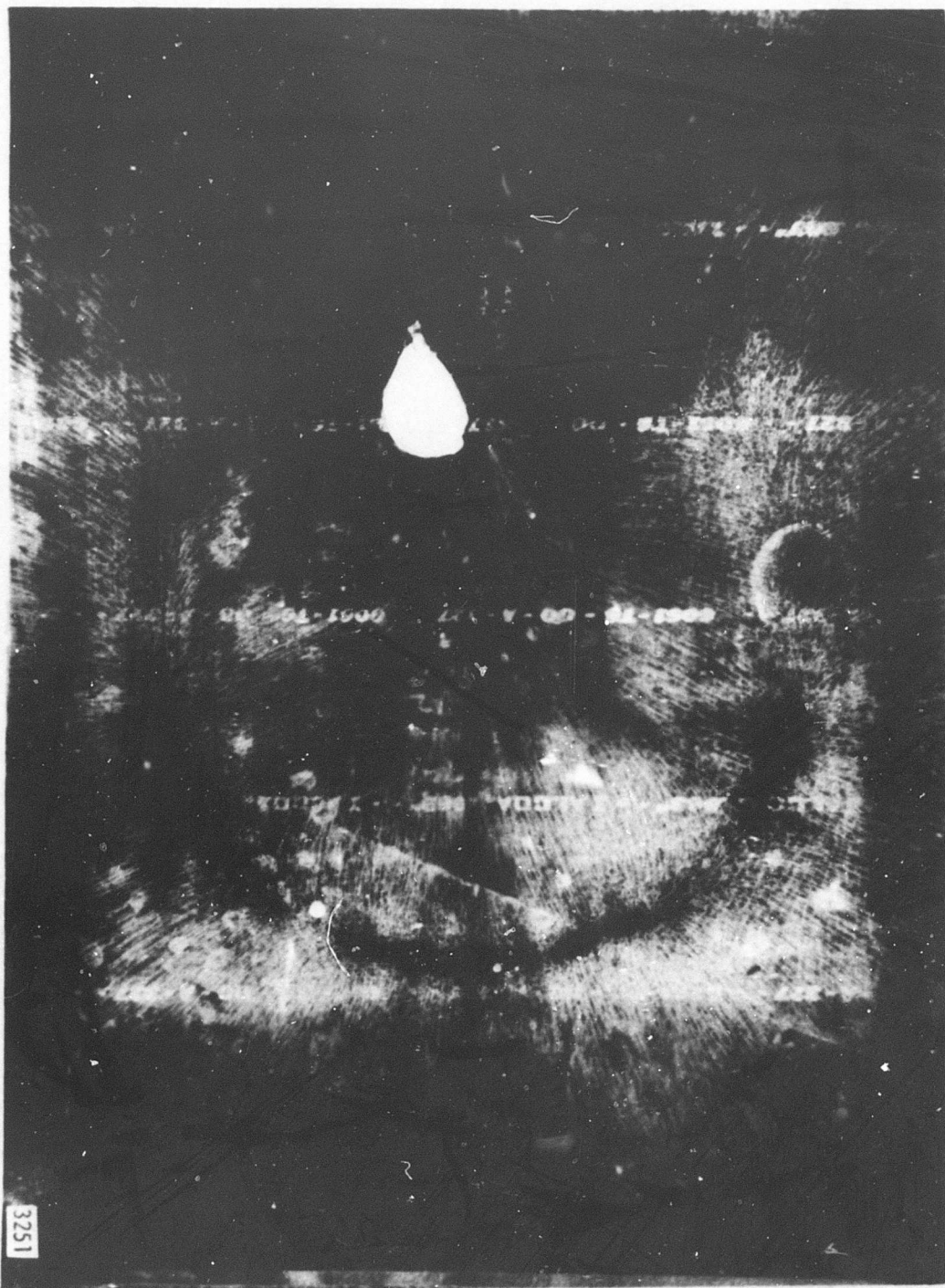
Figure 5 FLOW VISUALIZATION PICTURES OF TILTED IMPINGING NONUNIFORM JET, H/D = 1.99

(b) FLOW ALONG GROUND
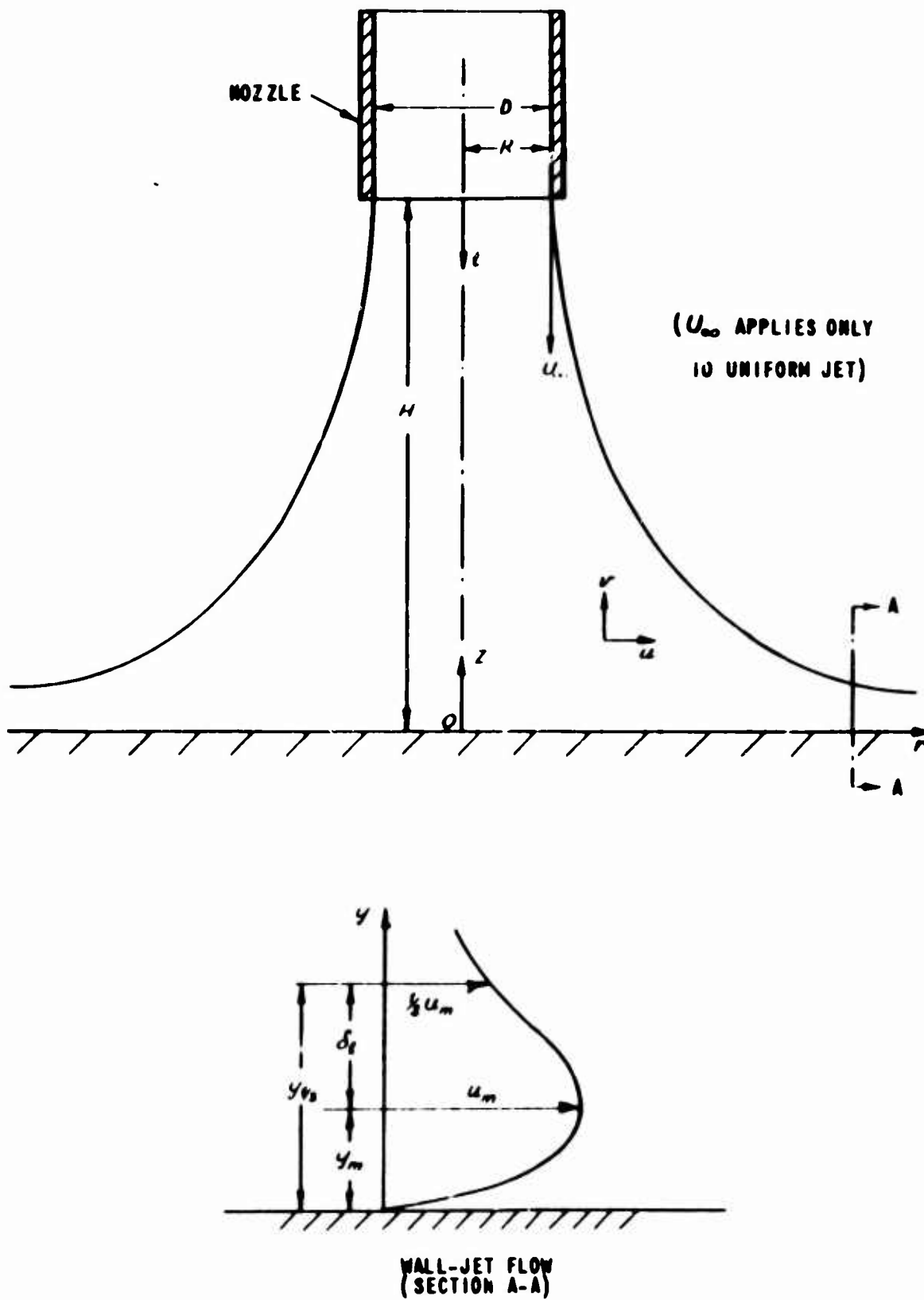
Figure 6 NOTATION FOR FLOW IN IMPINGING JET
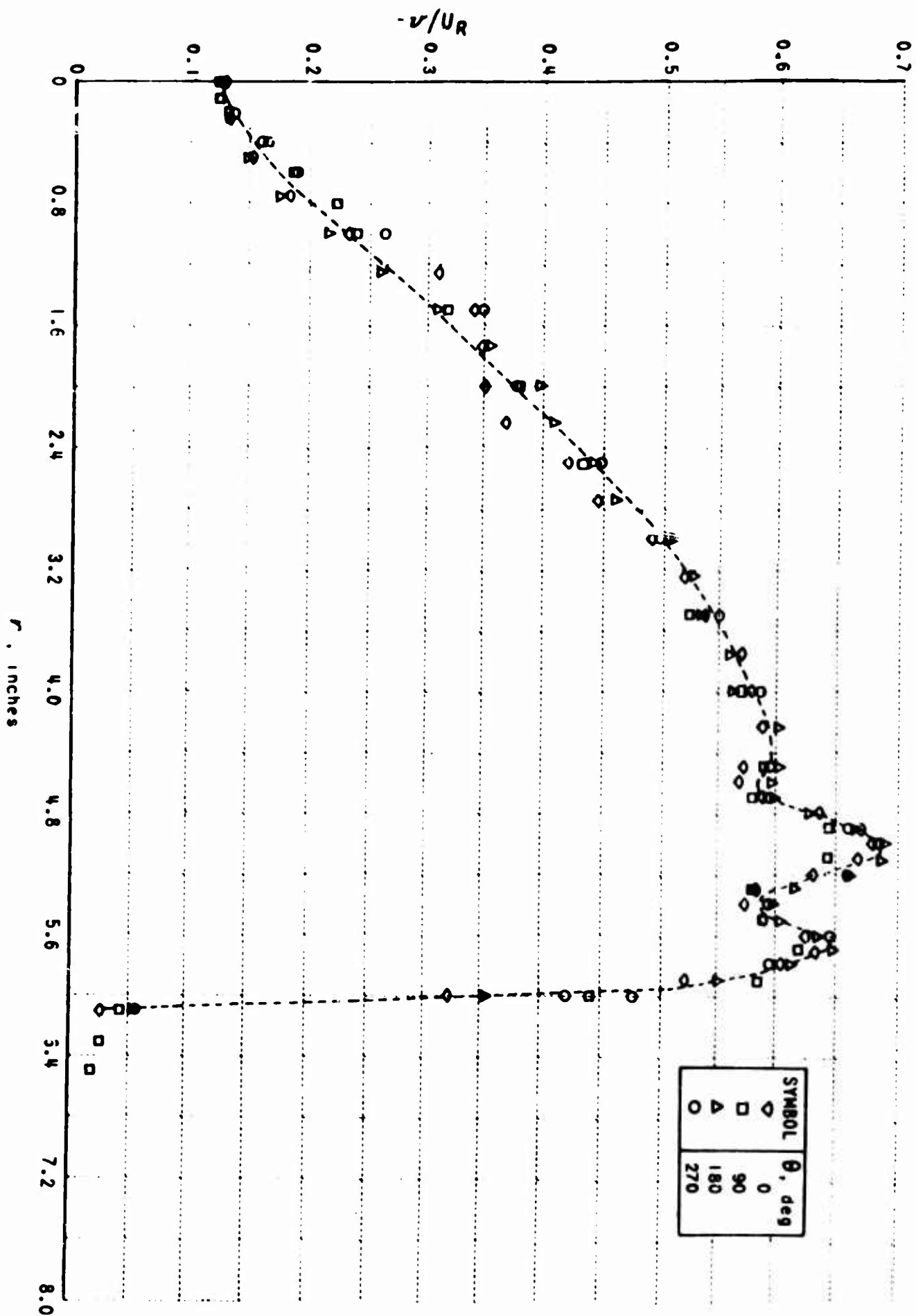
Figure 7 VELOCITY PROFILES IN FREE NONUNIFORM JET AT NOZZLE EXIT
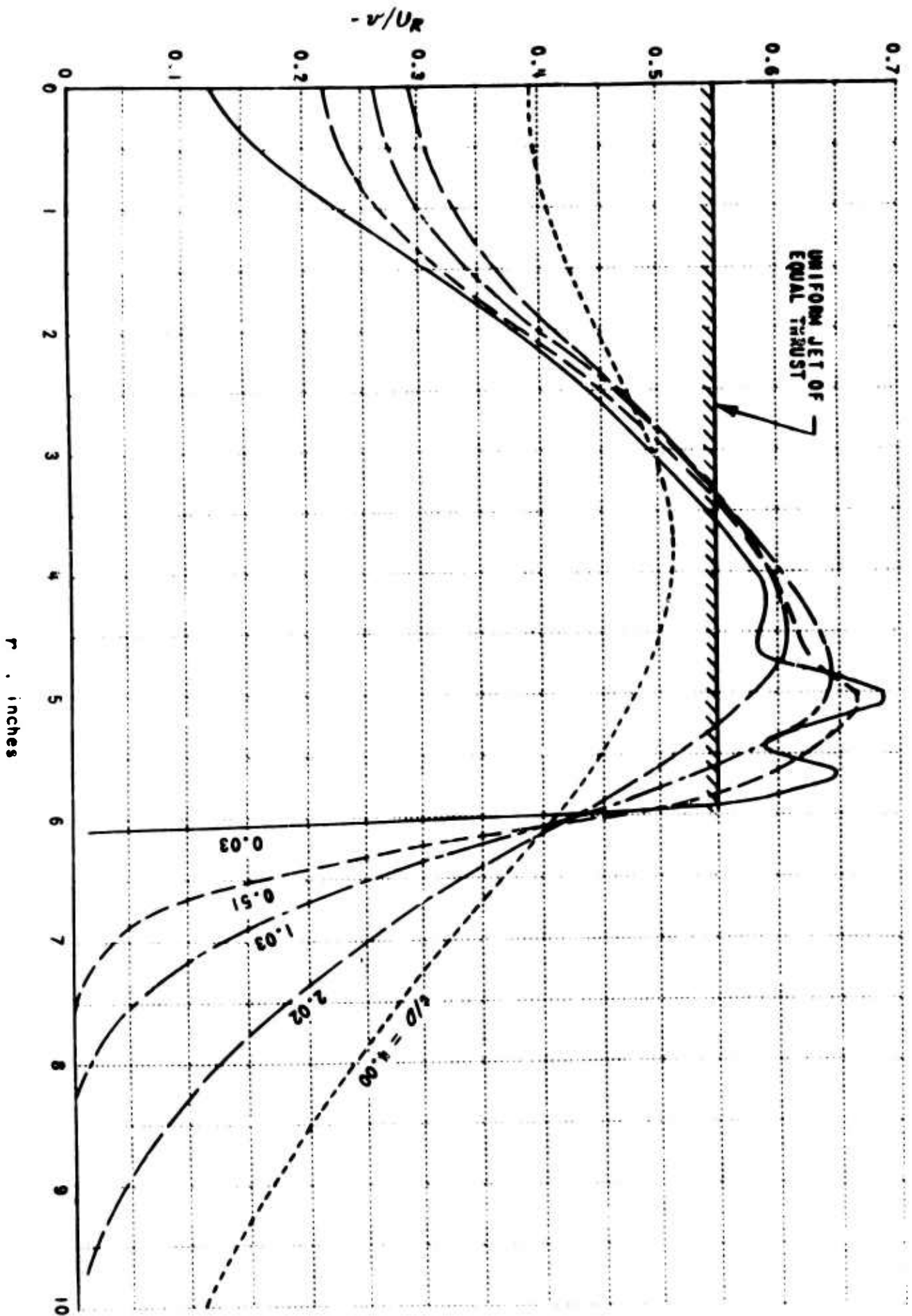
Figure 8 MEAN VELOCITY PROFILES IN FREE NONUNIFORM JET AT
VARIOUS DISTANCES FROM NOZZLE

Figure 9 VARIATION OF MAXIMUM VELOCITY AND CENTERLINE VELOCITY
IN NONUNIFORM FREE JET WITH DISTANCE FROM NOZZLE

$(0.695 - 0.0225 \, t/R)$

$-v/U_R$

t/R

△ CENTERLINE VELOCITY
○ MAXIMUM VELOCITY
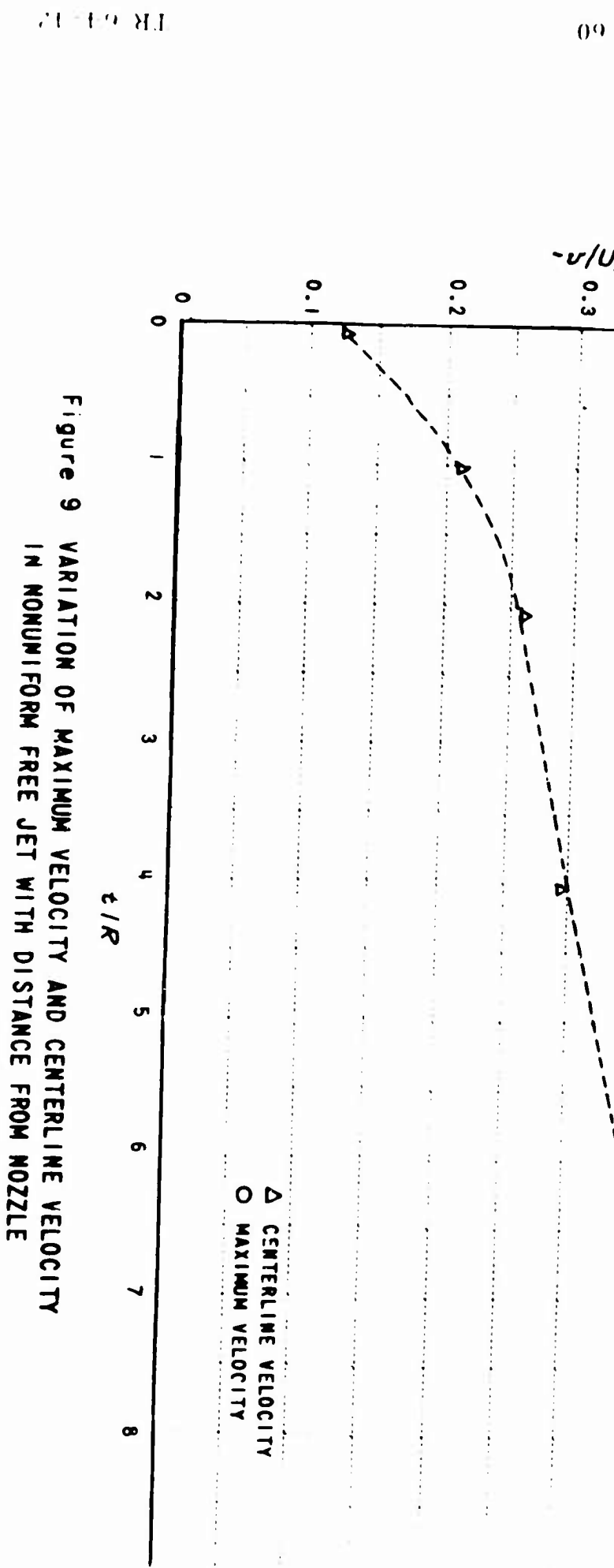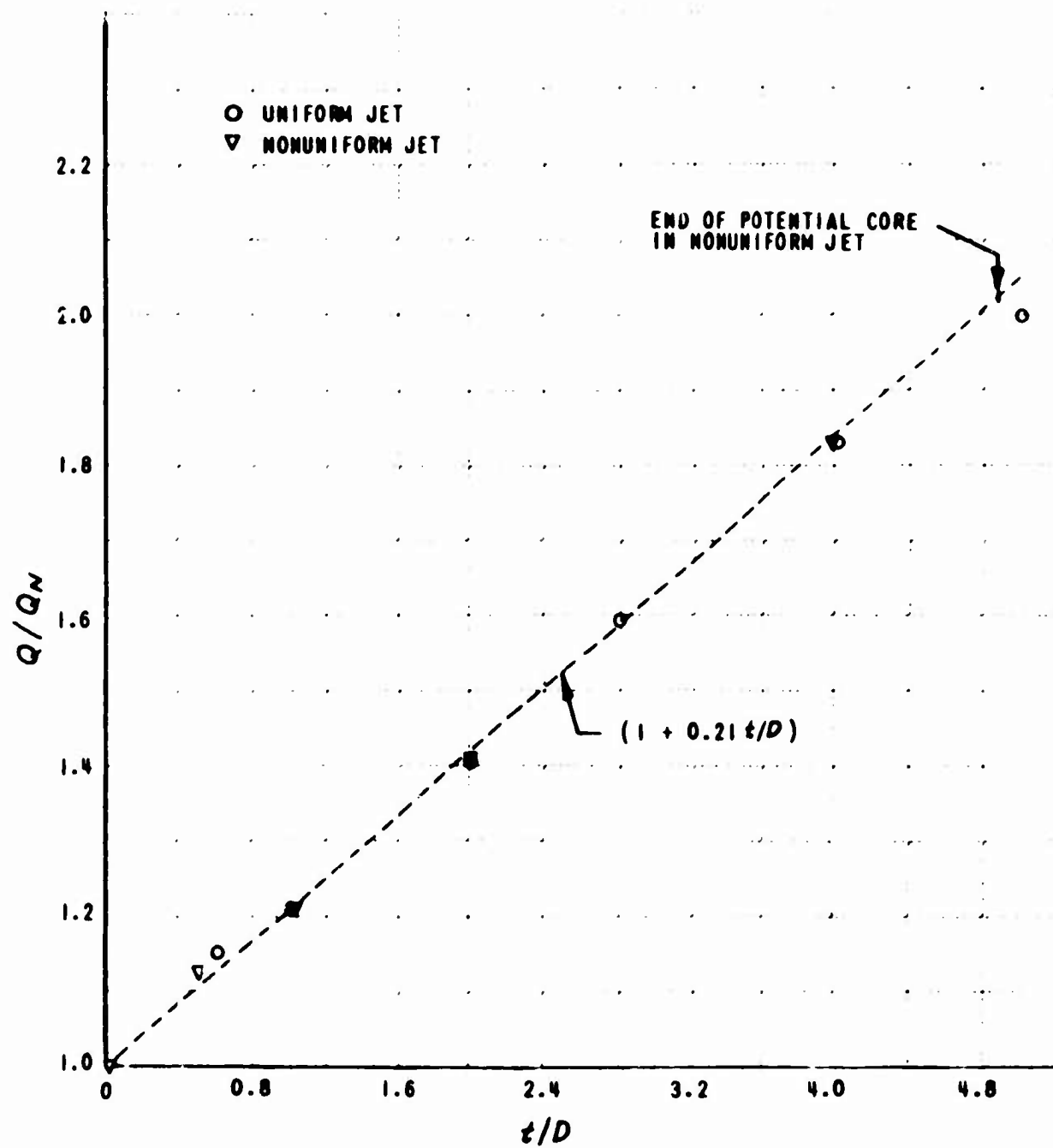
Figure 10 VARIATION OF MASS FLOW IN UNIFORM AND NONUNIFORM
FREE JETS WITH DISTANCE FROM NOZZLE

61
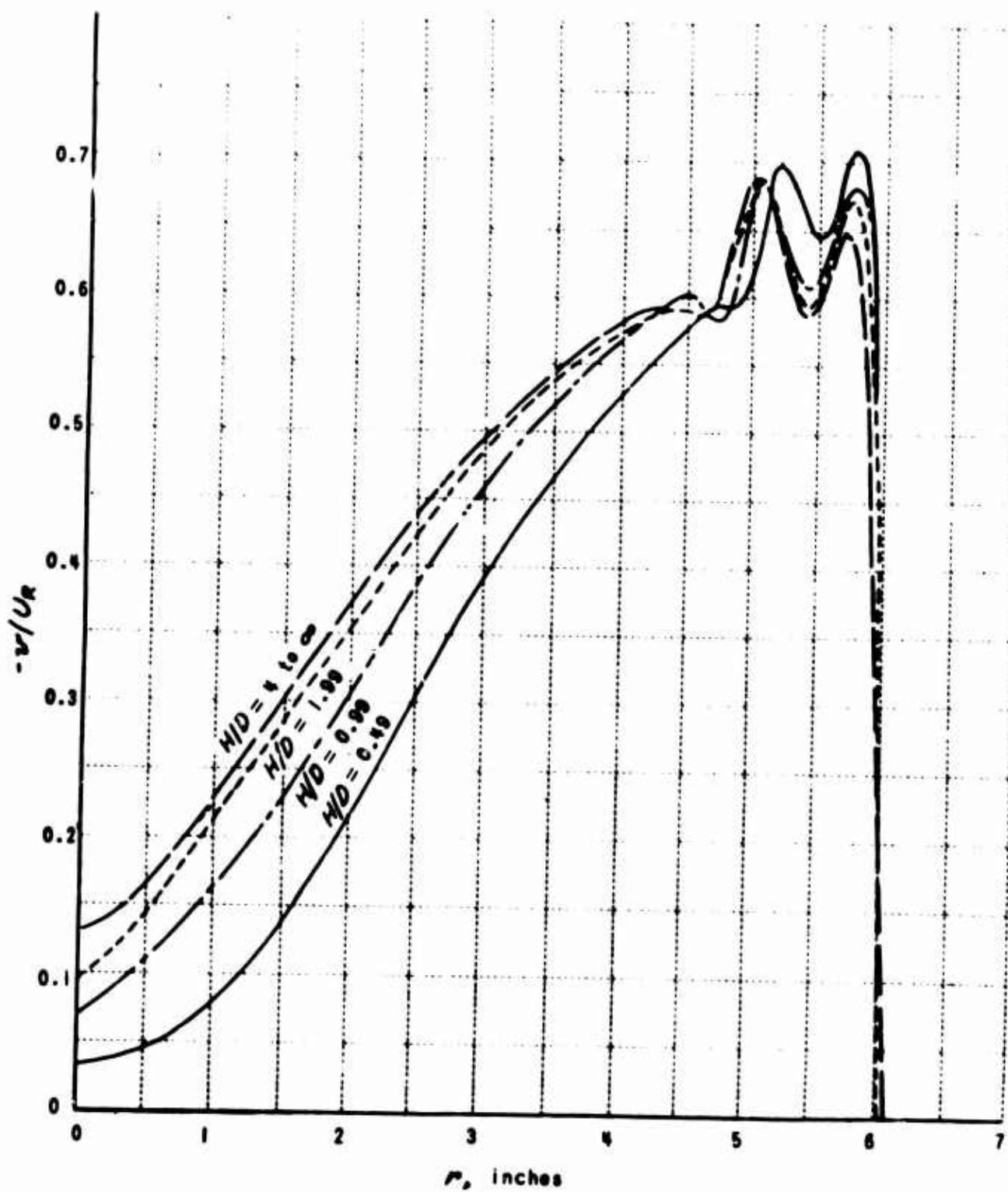
Figure 11 MEAN VELOCITY PROFILES IN NOZZLE EXIT PLANE FOR VARIOUS H/D, NONUNIFORM JET
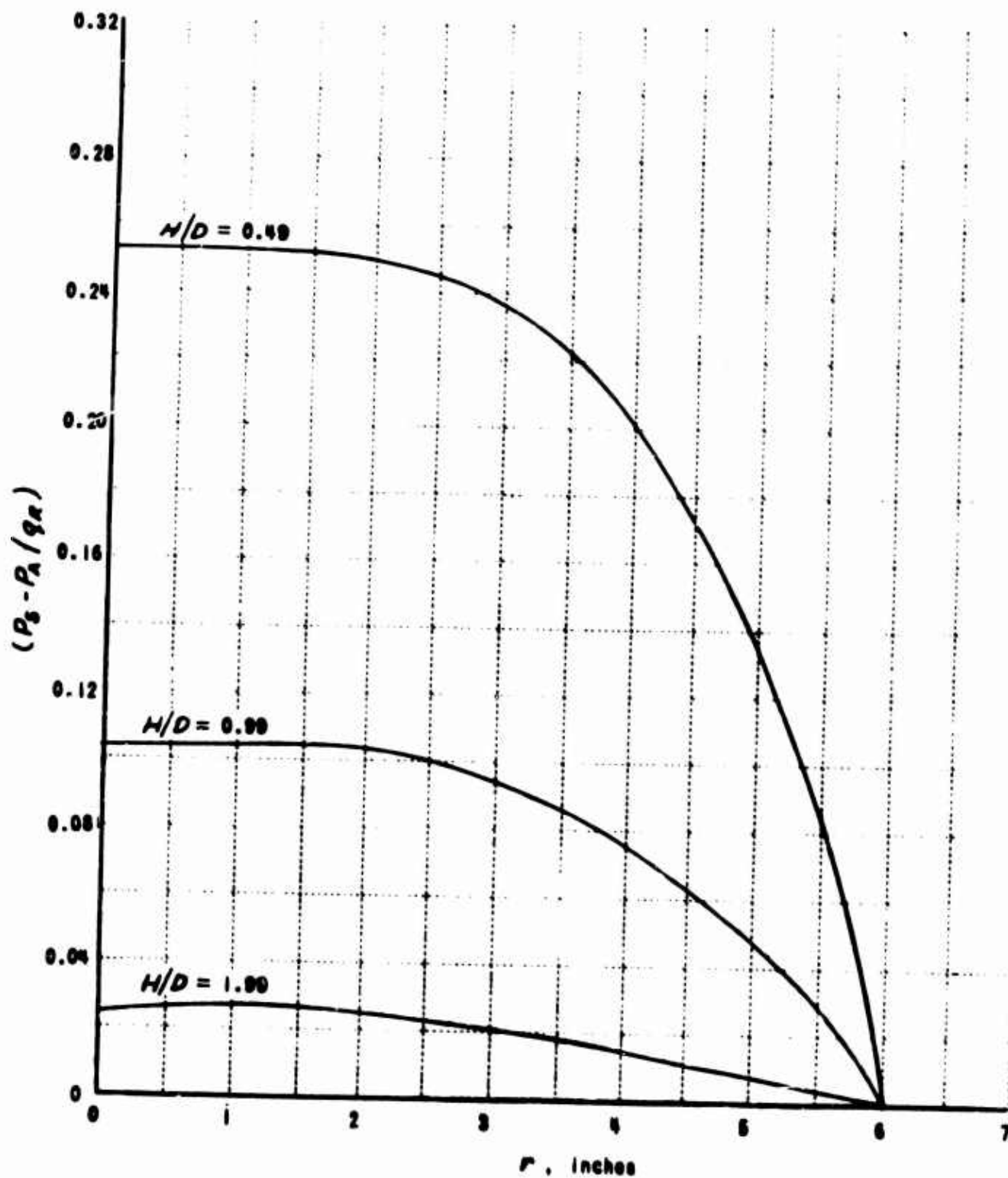
Figure 12 MEAN STATIC PRESSURE PROFILES IN NOZZLE EXIT PLANE
FOR VARIOUS *H/D*, NONUNIFORM JET
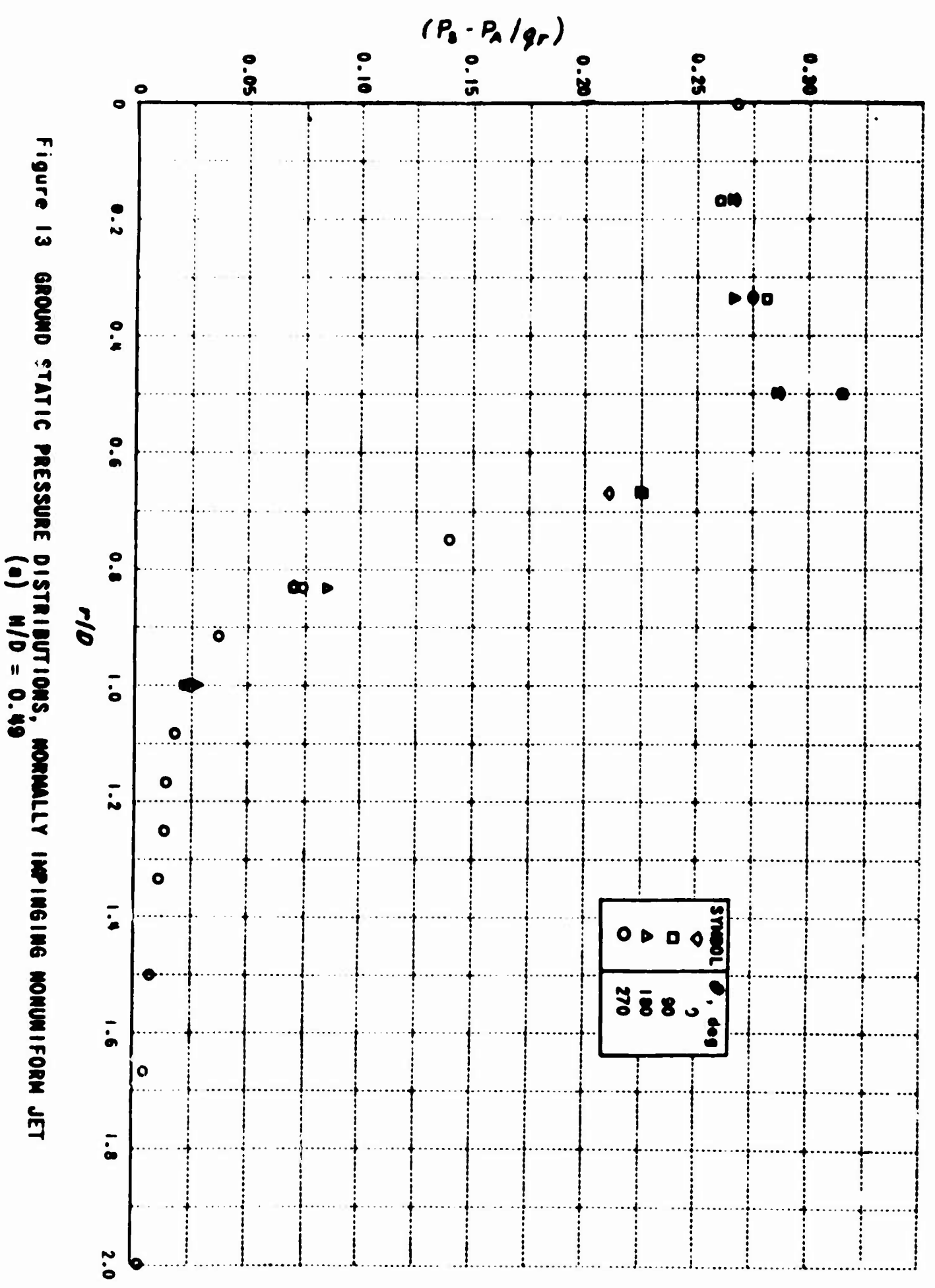
63

Figure 13 GROUND STATIC PRESSURE DISTRIBUTIONS, NORMALLY IMPINGING NONUNIFORM JET
(a) H/D = 0.49
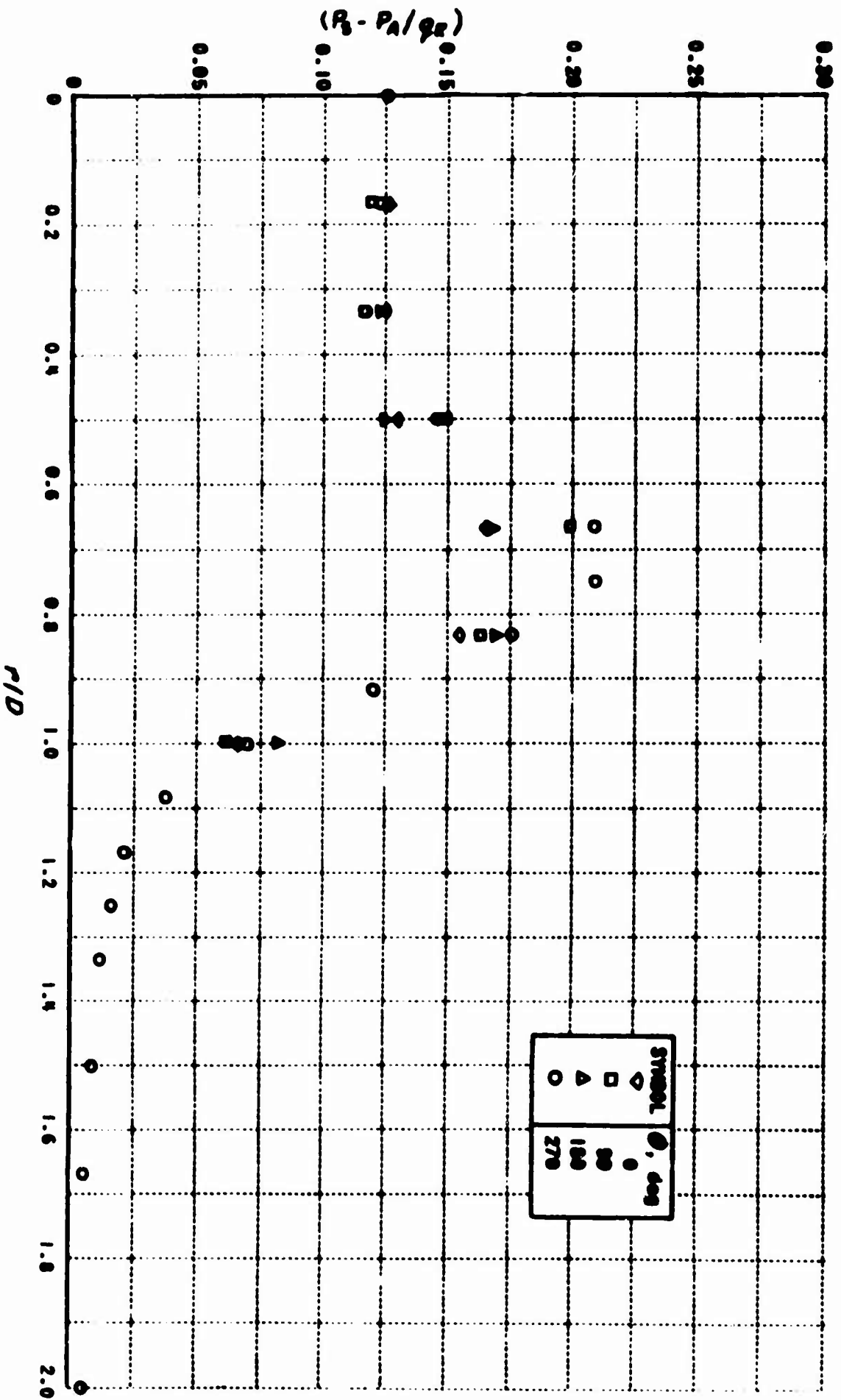
Figure 13 GROUND STATIC PRESSURE DISTRIBUTIONS, NORMALLY IMPINGING NONUNIFORM JET

(b) H/D = 0.99
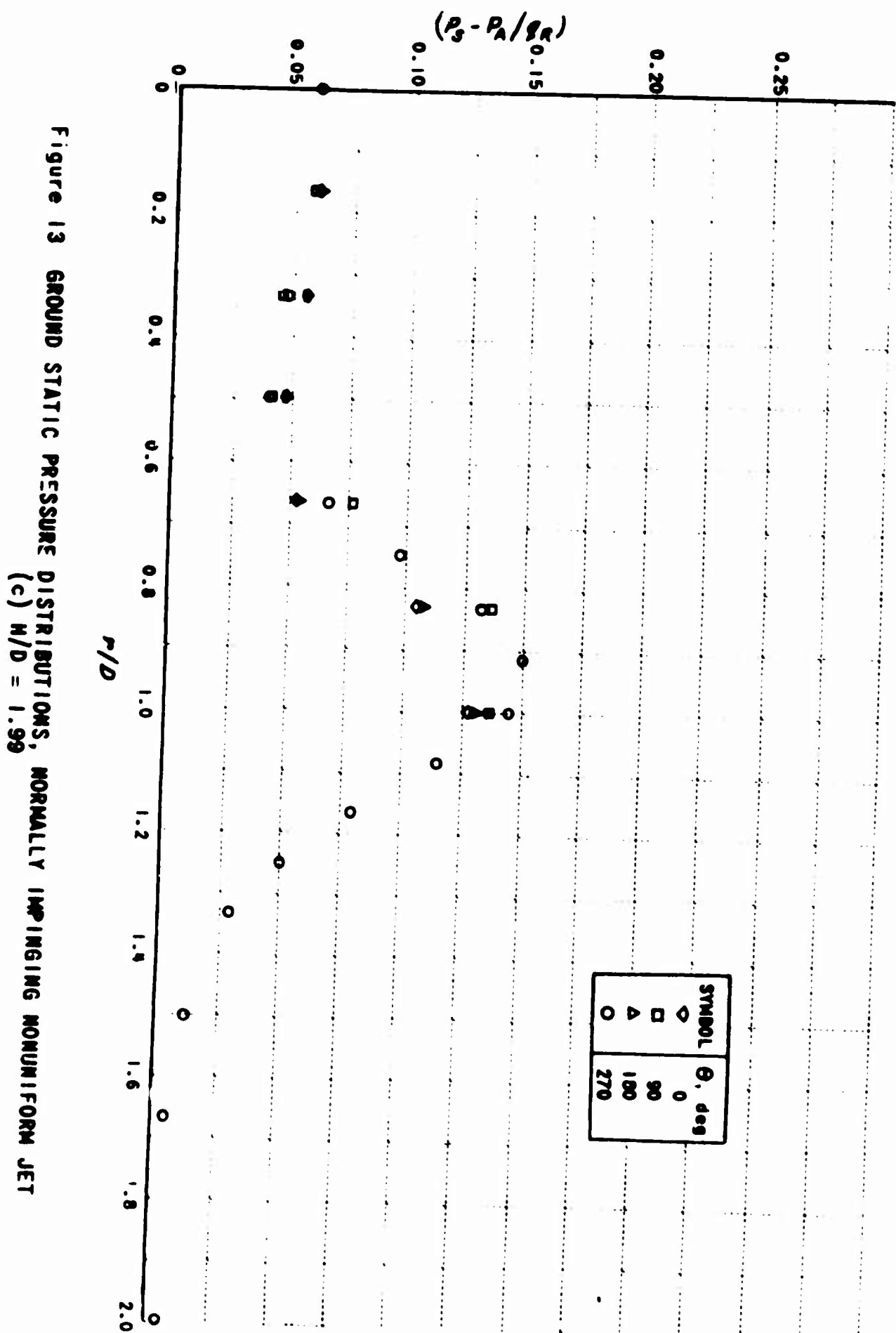
Figure 13 GROUND STATIC PRESSURE DISTRIBUTIONS, NORMALLY IMPINGING NONUNIFORM JET
(c) H/D = 1.99
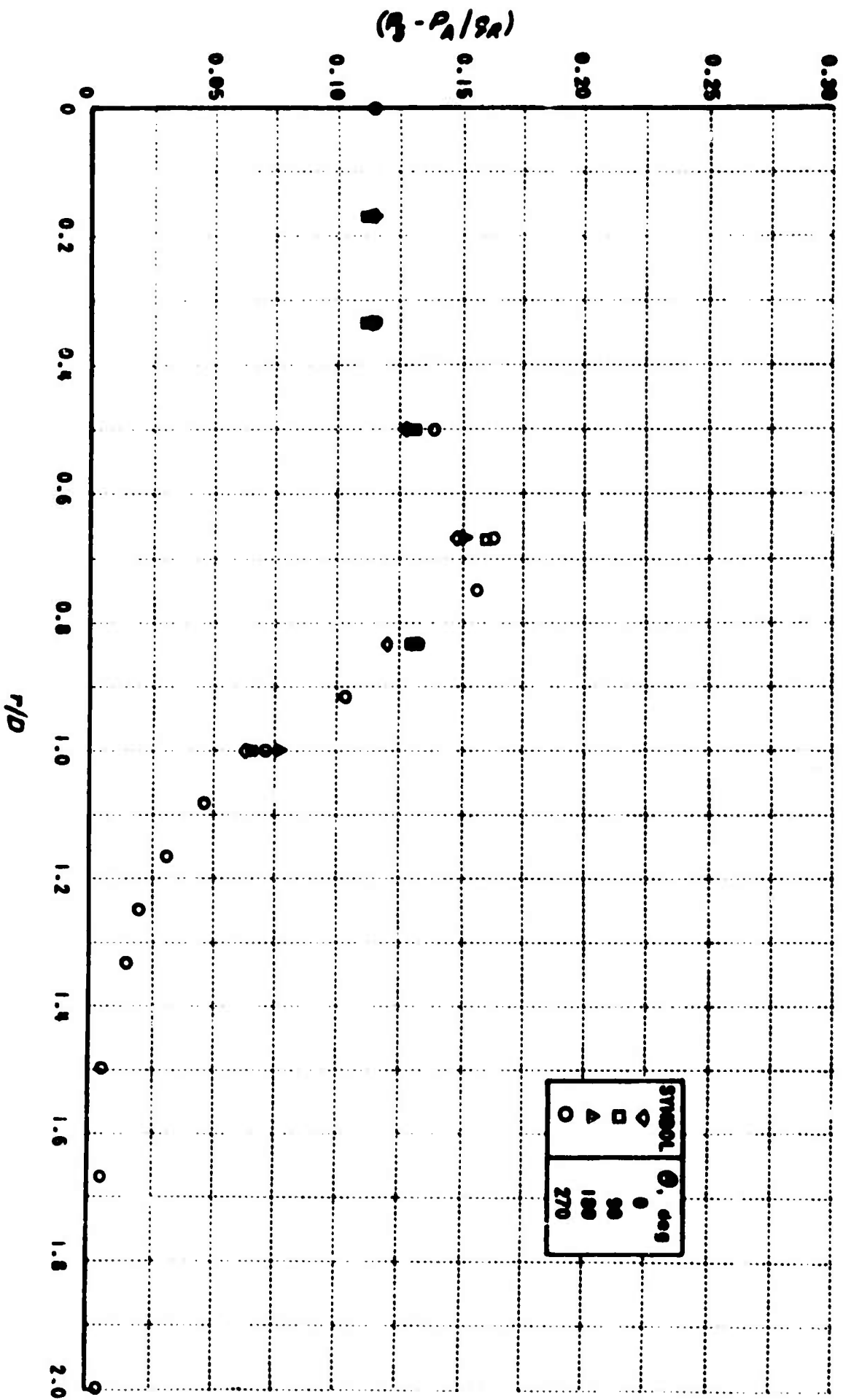
Figure 13 GROUND STATIC PRESSURE DISTRIBUTIONS, NORMALLY IMPINGING NONUNIFORM JET
(d) H/D = 4.07

Figure 14 GROUND STATIC PRESSURE DISTRIBUTION, NONUNIFORM JET, $H/D = 1.99$
TILT ANGLE $\cong$ 5 degrees
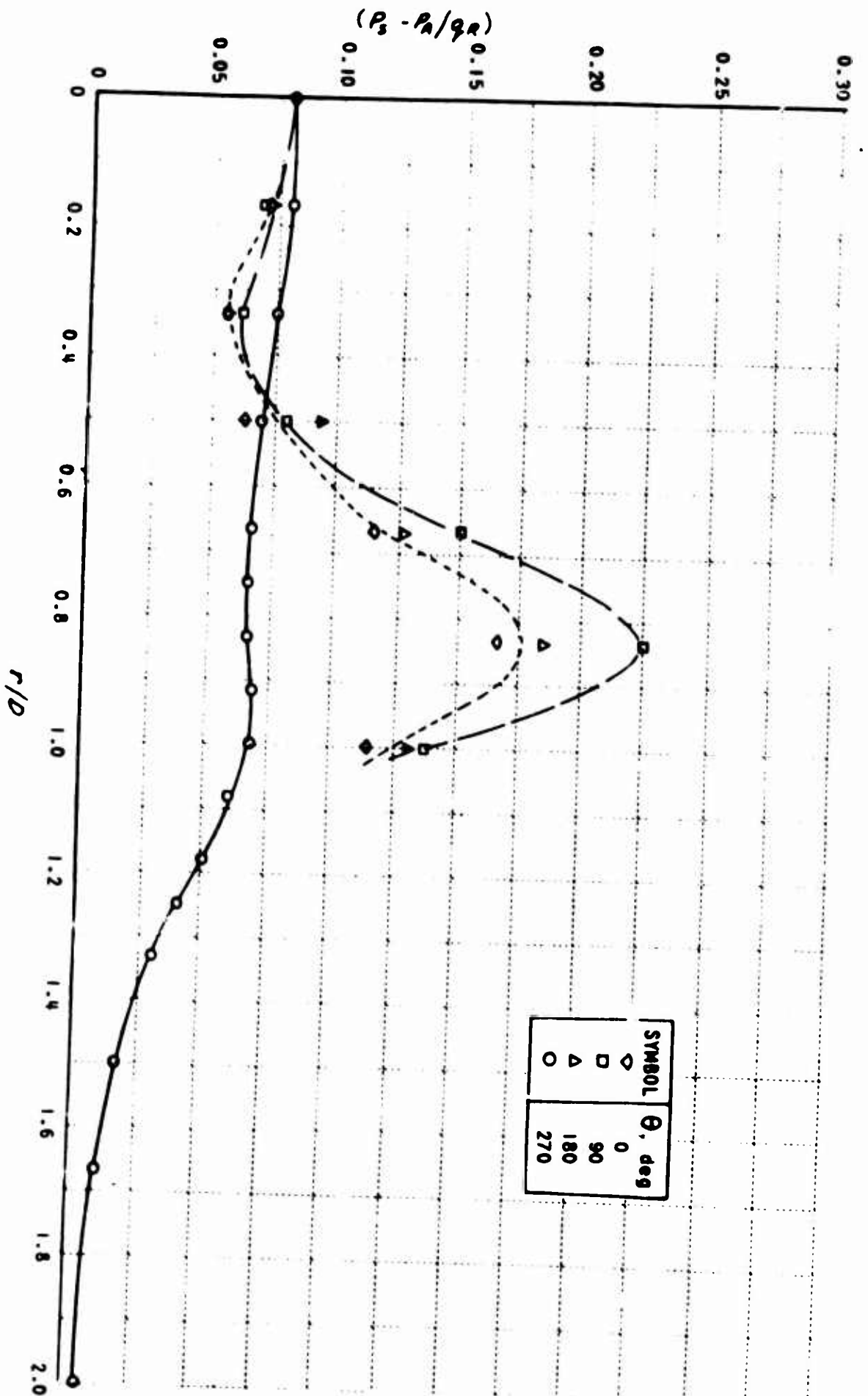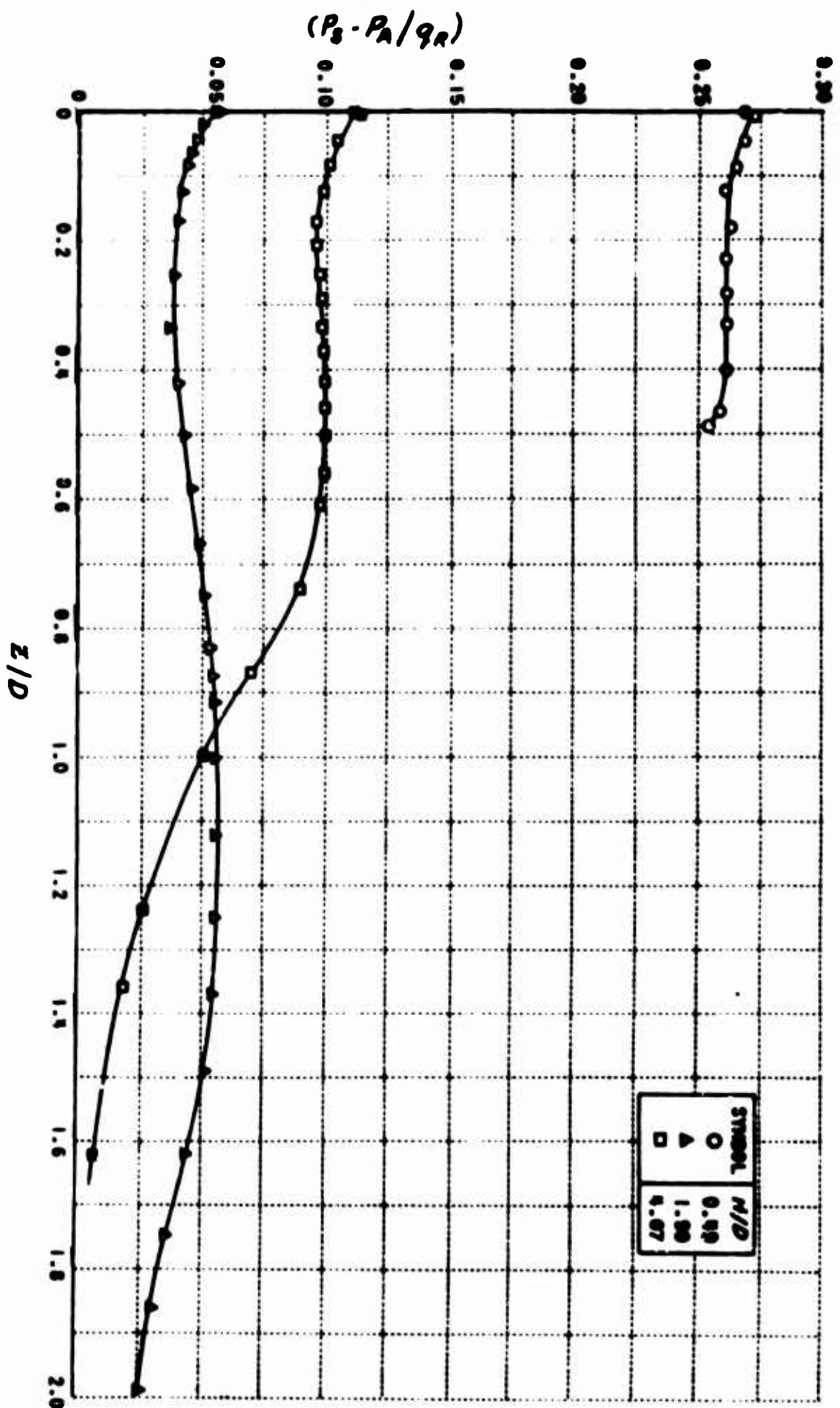
Figure 15　STATIC PRESSURE DISTRIBUTIONS ON JET CENTERLINE, NONUNIFORM JET

Figure 16 ABSOLUTE VELOCITY DISTRIBUTIONS IN TURNING REGION OF IMPINGING NONUNIFORM
JET AT SEVERAL CONSTANT DISTANCES FROM GROUND, H/D = 1.99
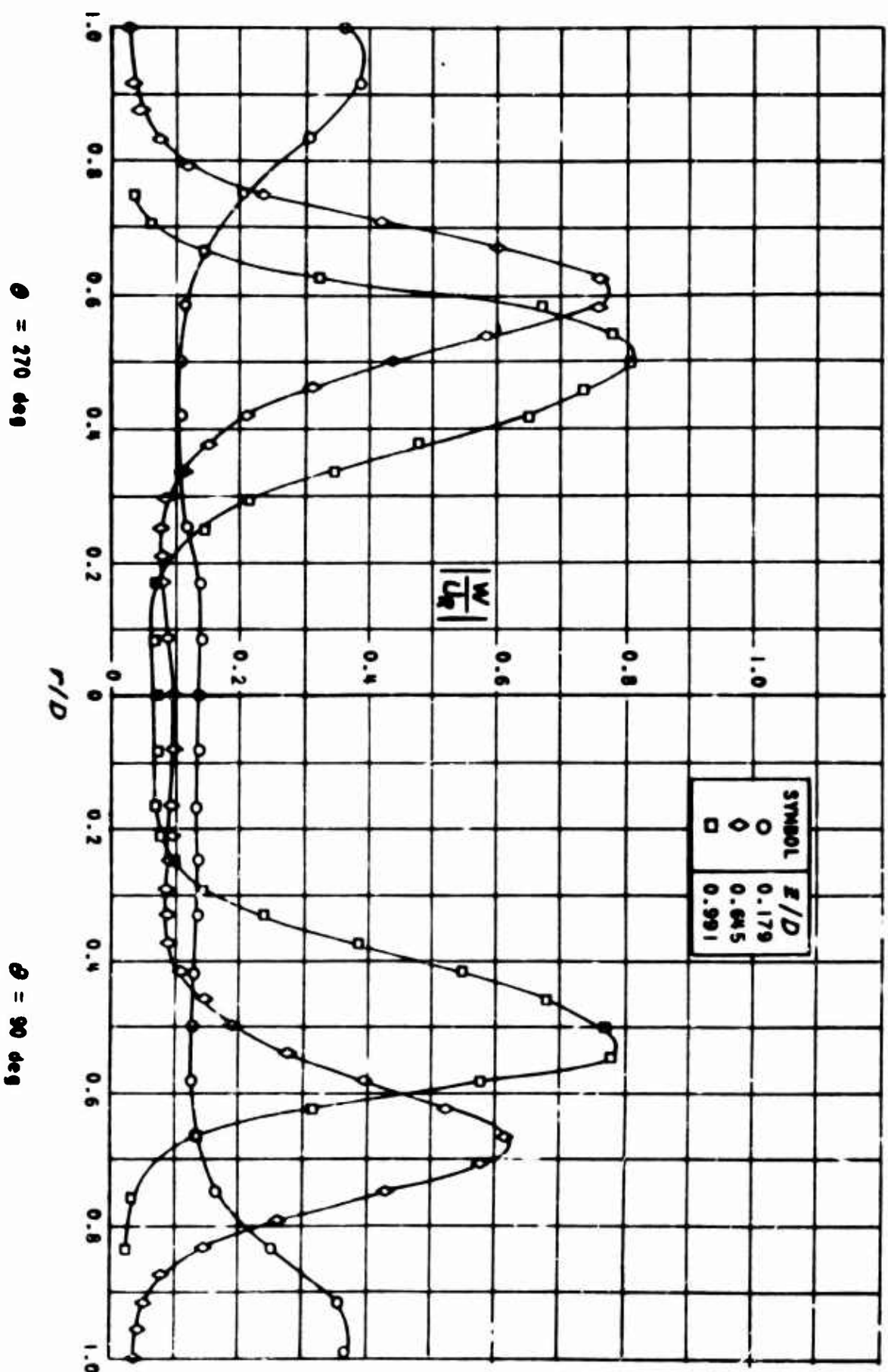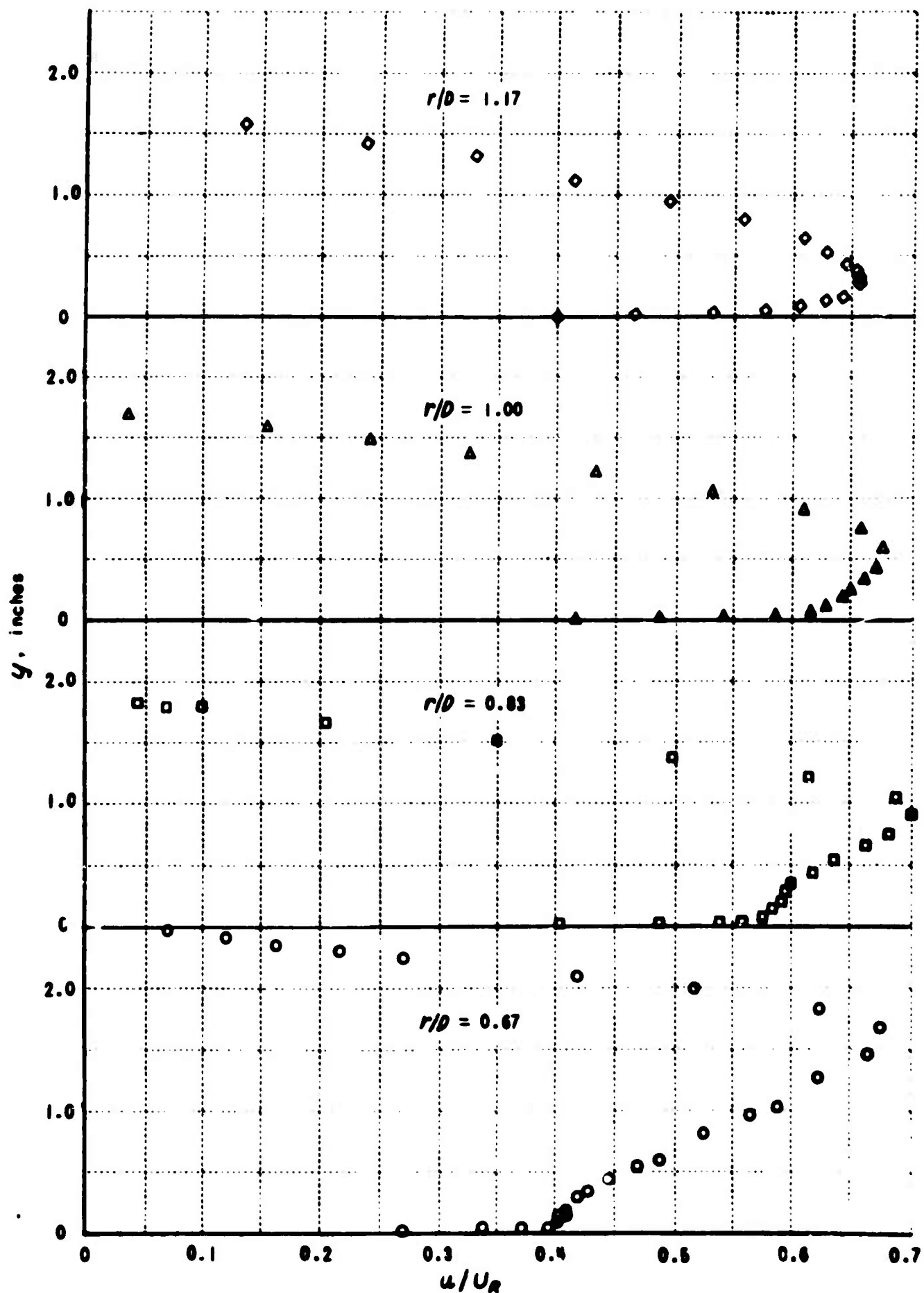
Figure 17 VELOCITY PROFILES NEAR GROUND, NORMALLY IMPINGING NONUNIFORM JET
(a) H/D = 0.49

71
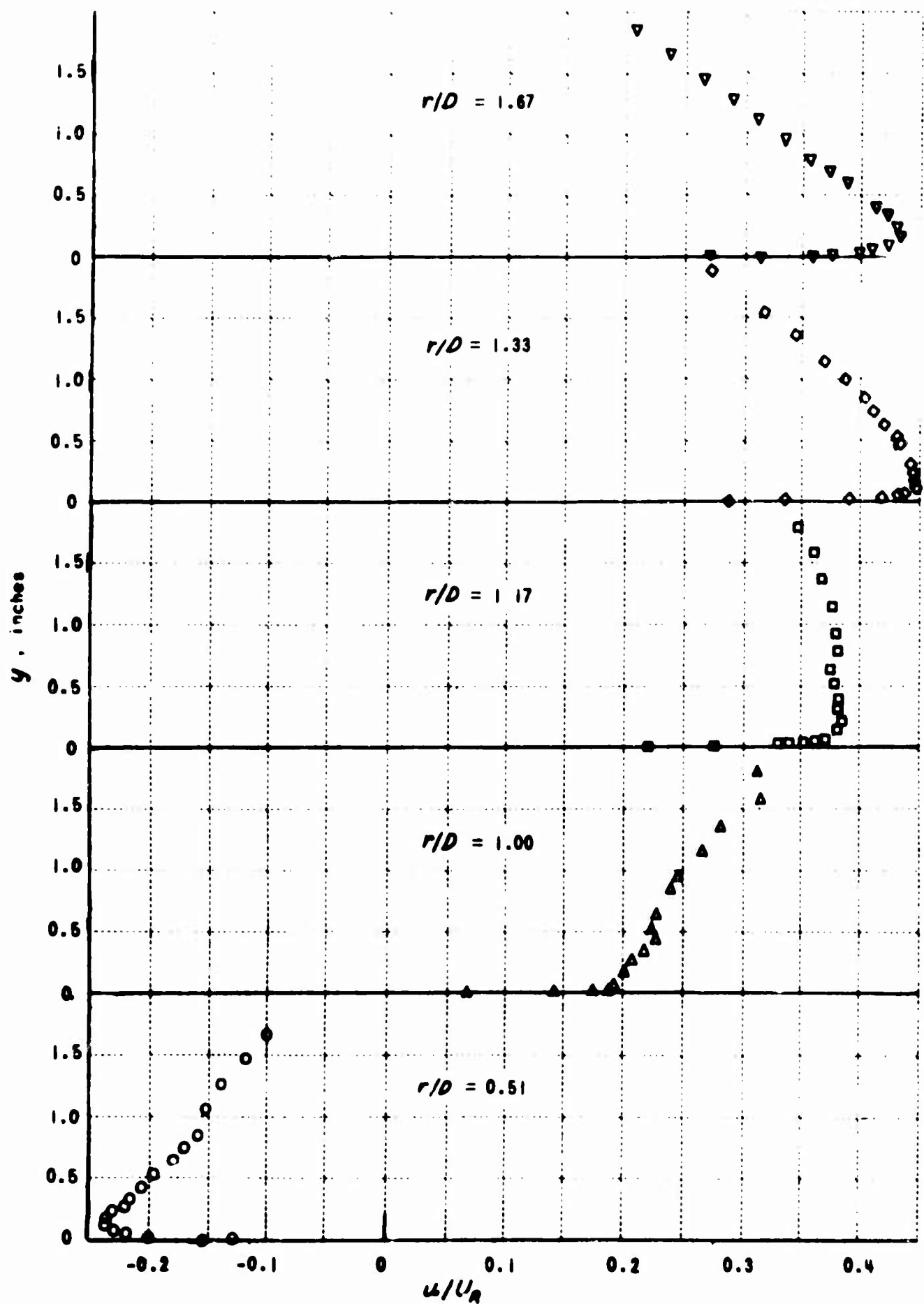
Figure 17 VELOCITY PROFILES NEAR GROUND, NORMALLY IMPINGING NONUNIFORM JET
(b) H/D = 1.99

72   TR 64-42
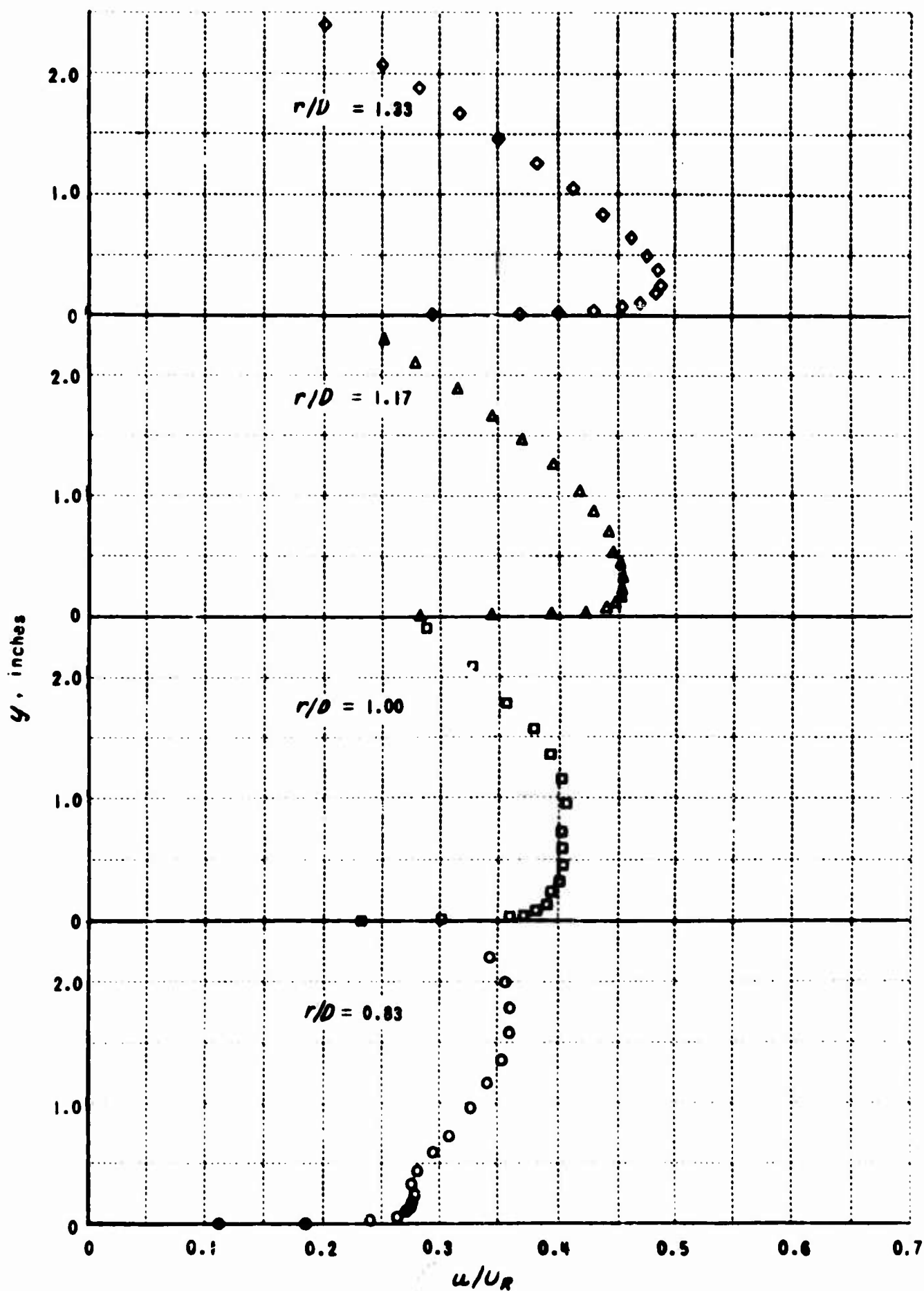
Figure 17 VELOCITY PROFILES NEAR GROUND, NORMALLY IMPINGING NONUNIFORM JET
(c) H/D = 4.07
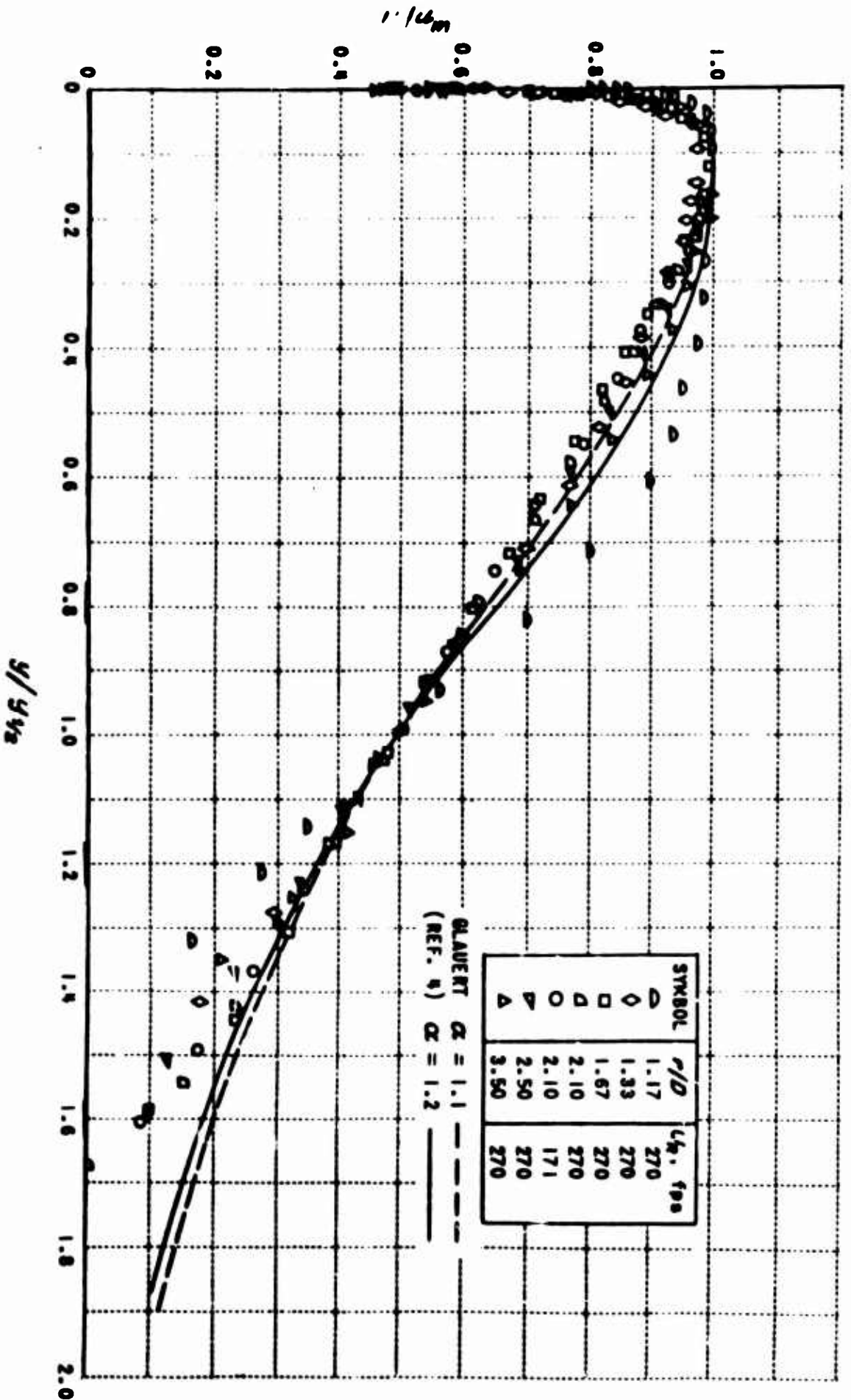
Figure 18 VELOCITY PROFILES NEAR THE GROUND FOR r/R > 1.0,
NONUNIFORM JET, H/D = 1.99

Figure 19 BOUNDARY LAYER PROFILES FOR $r/D > 1.0$, NONUNIFORM JET, $H/D = 1.99$

SYMBOL	r/D	u_n, fps
◇	1.17	270
○	1.33	270
□	1.67	270
◇	2.10	270
○	2.10	171
▽	2.50	270
△	3.50	270

GLAUERT $\alpha = 1.1$
(REF. 4) $\alpha = 1.2$
$\alpha = 1.16$

LAMINAR SUBLAYER FOR TURBULENT PIPE FLOW MATCHED TO $\alpha = 1.16$ AT $y/y_{1/2} = 0.015$
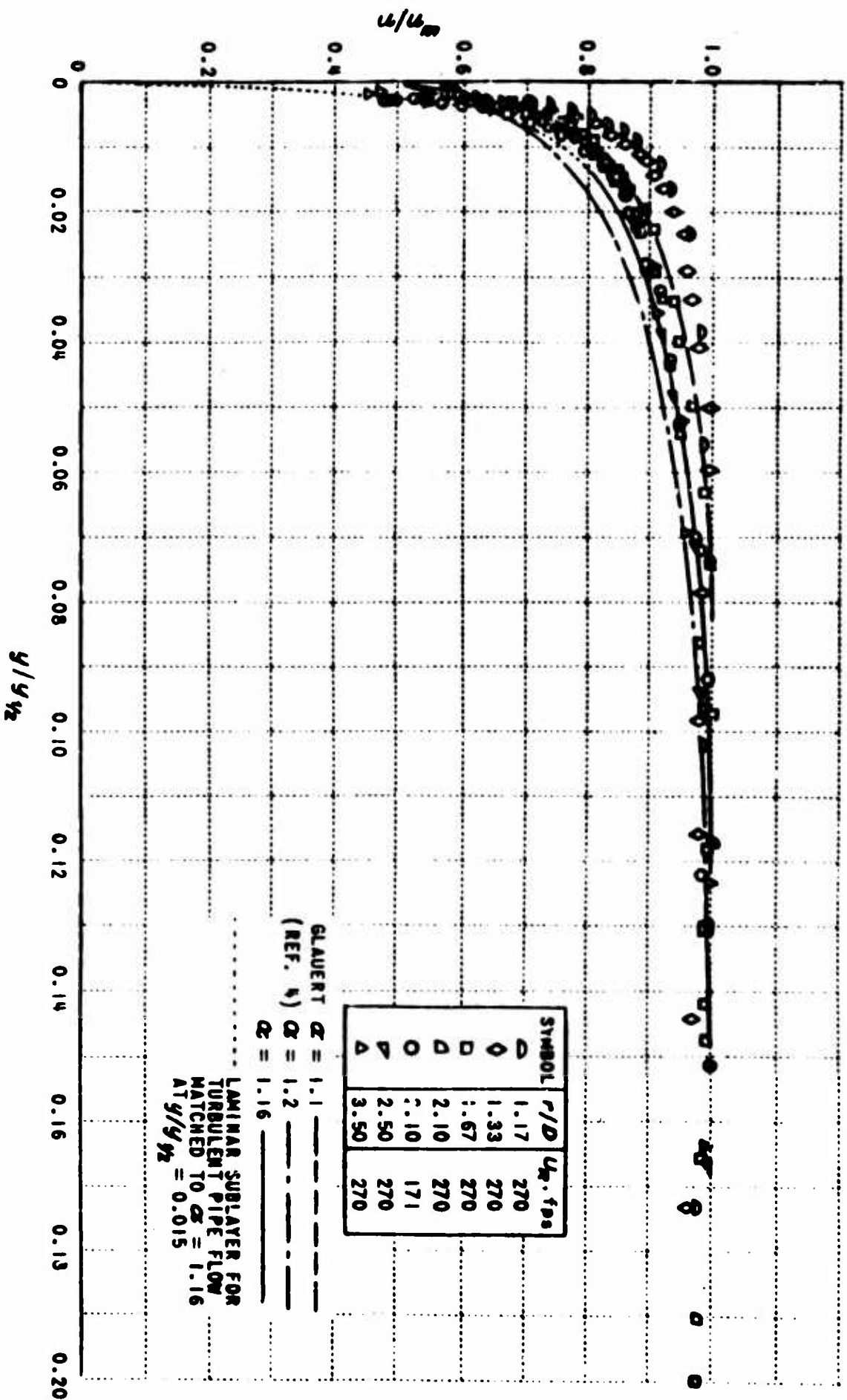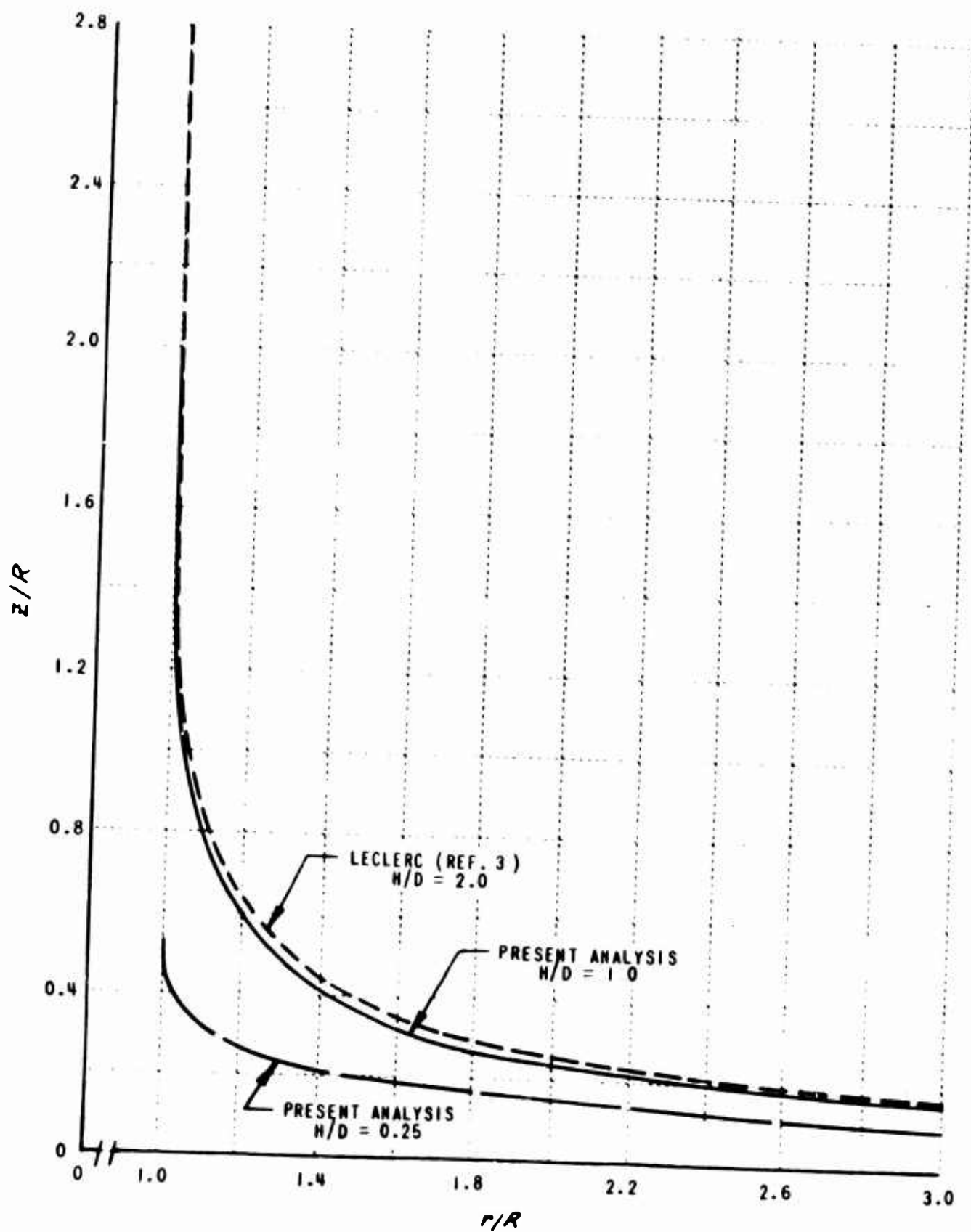
Figure 20   COMPUTED JET BOUNDARIES FOR UNIFORM INVISCID JET
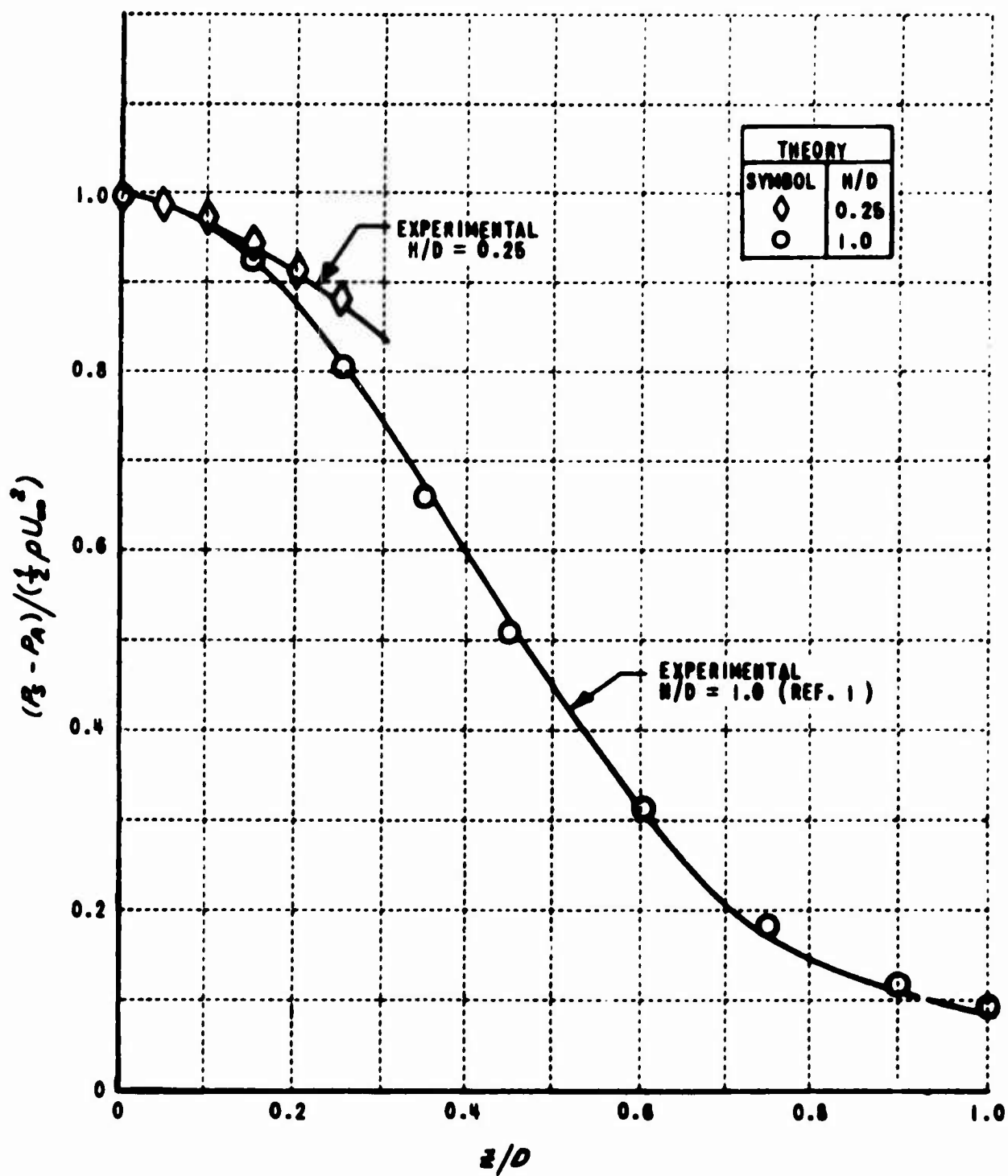
Figure 21 JET-CENTERLINE STATIC PRESSURE DISTRIBUTIONS, UNIFORM JET

77
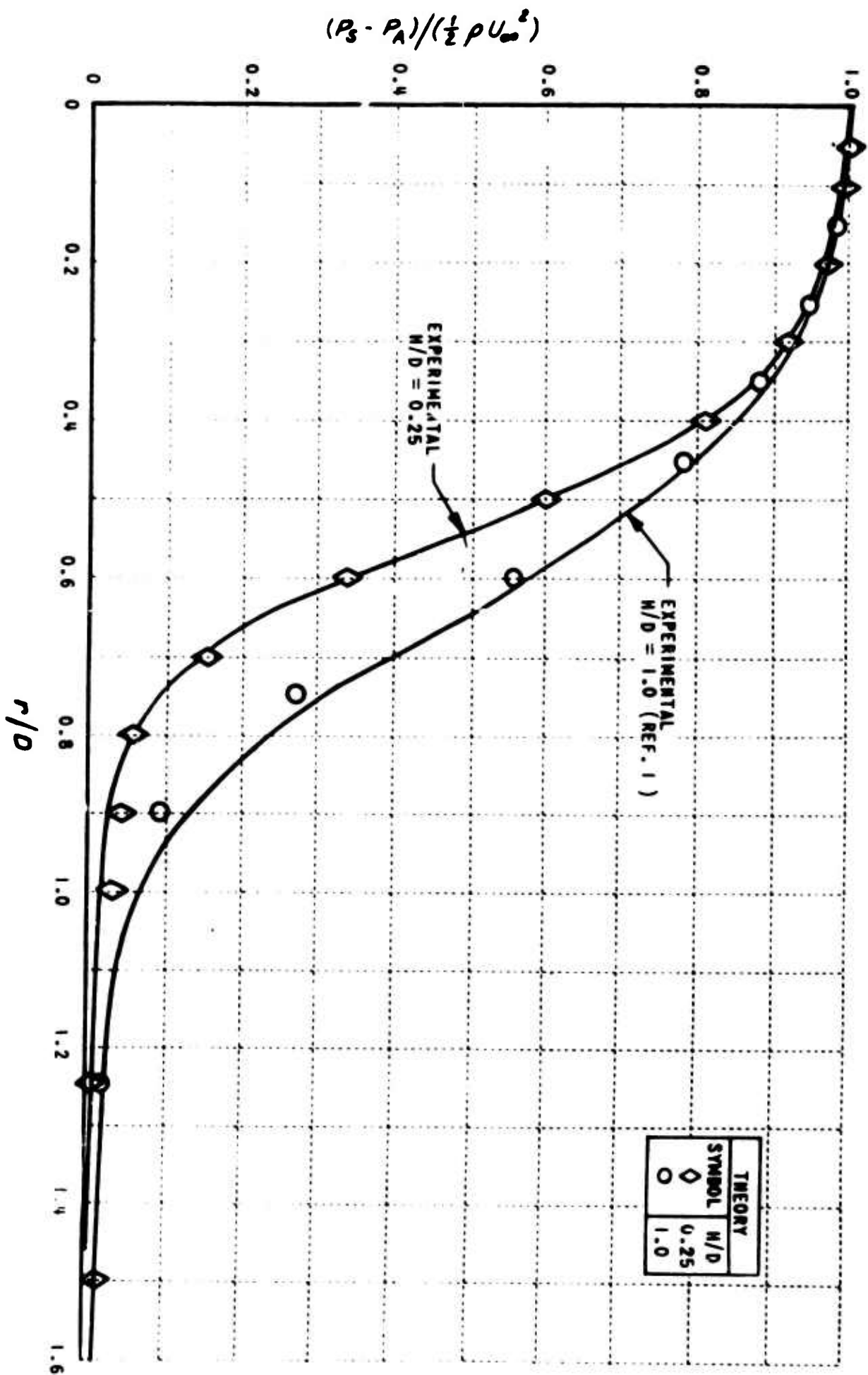
Figure 22 GROUND-PLANE STATIC PRESSURE DISTRIBUTIONS, UNIFORM JET
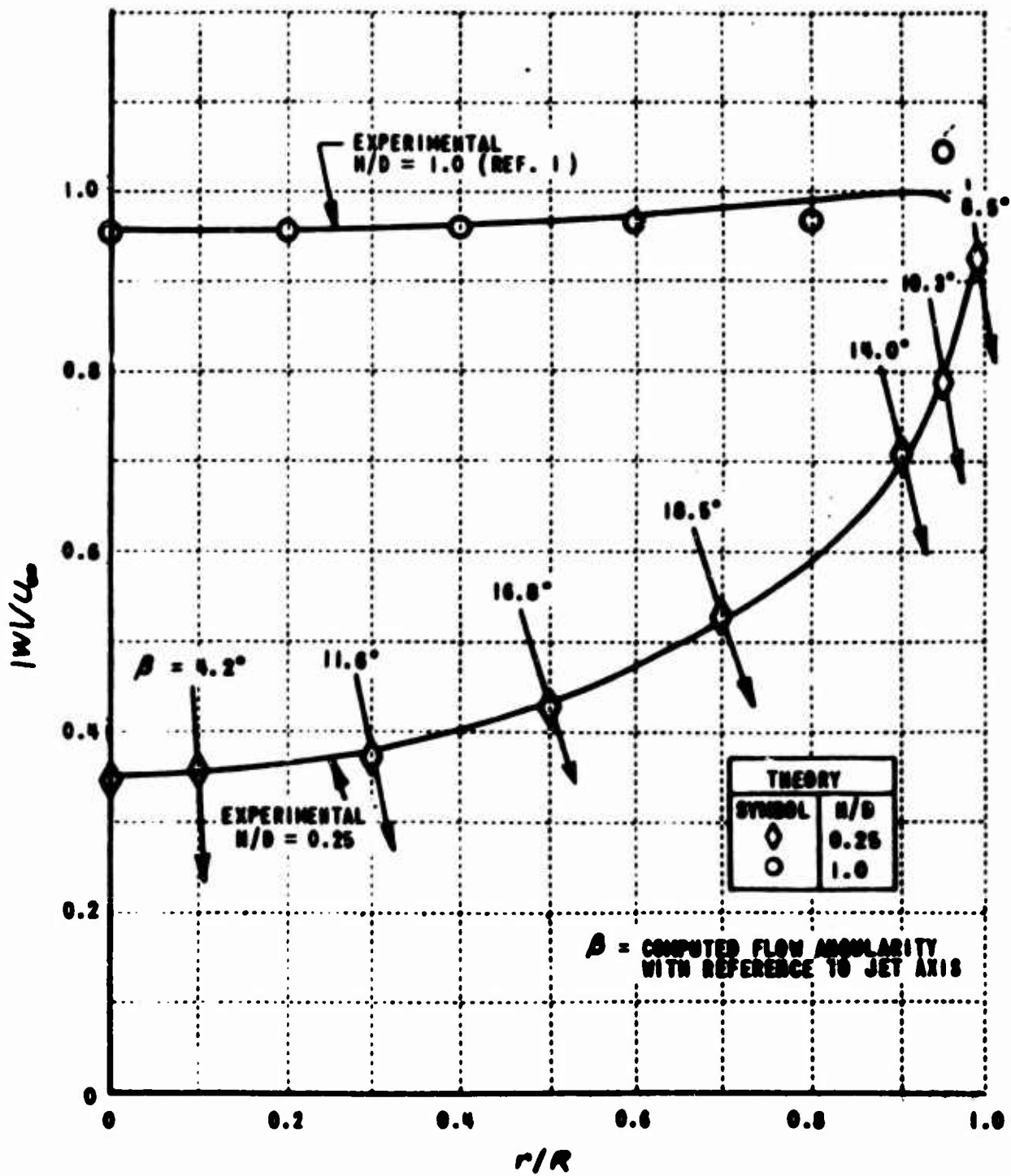
Figure 23 VELOCITY DISTRIBUTIONS AT NOZZLE EXIT, UNIFORM JET

79
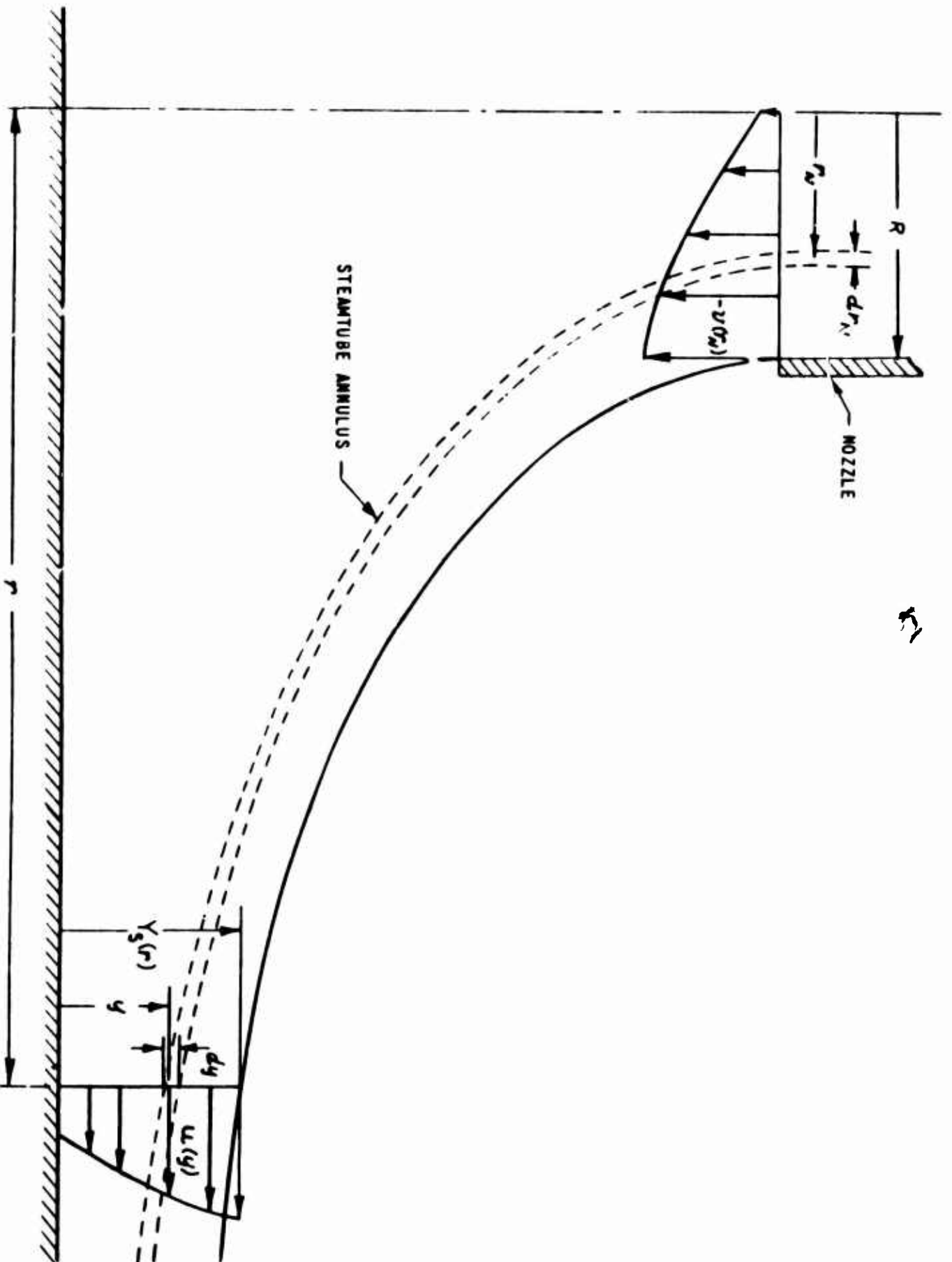
Figure 24　NOTATION USED IN CALCULATION OF RADIAL MOMENTUM
FLUX OF FLOW UNDER NONUNIFORM IMPINGING JET
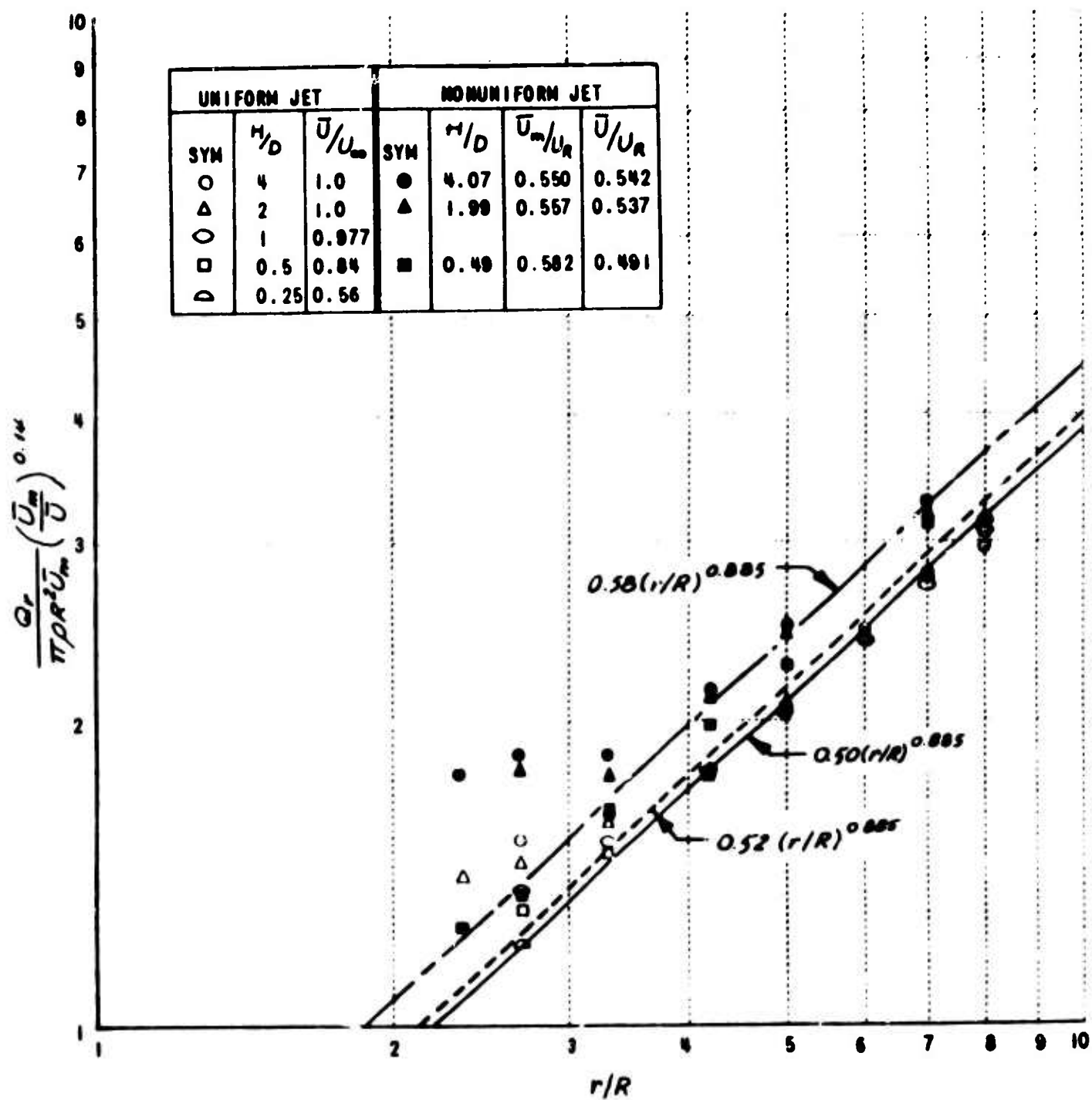
Figure 25 NONDIMENSIONAL RADIAL MASS FLOW vs. r/R FOR BOTH UNIFORM AND NONUNIFORM JETS
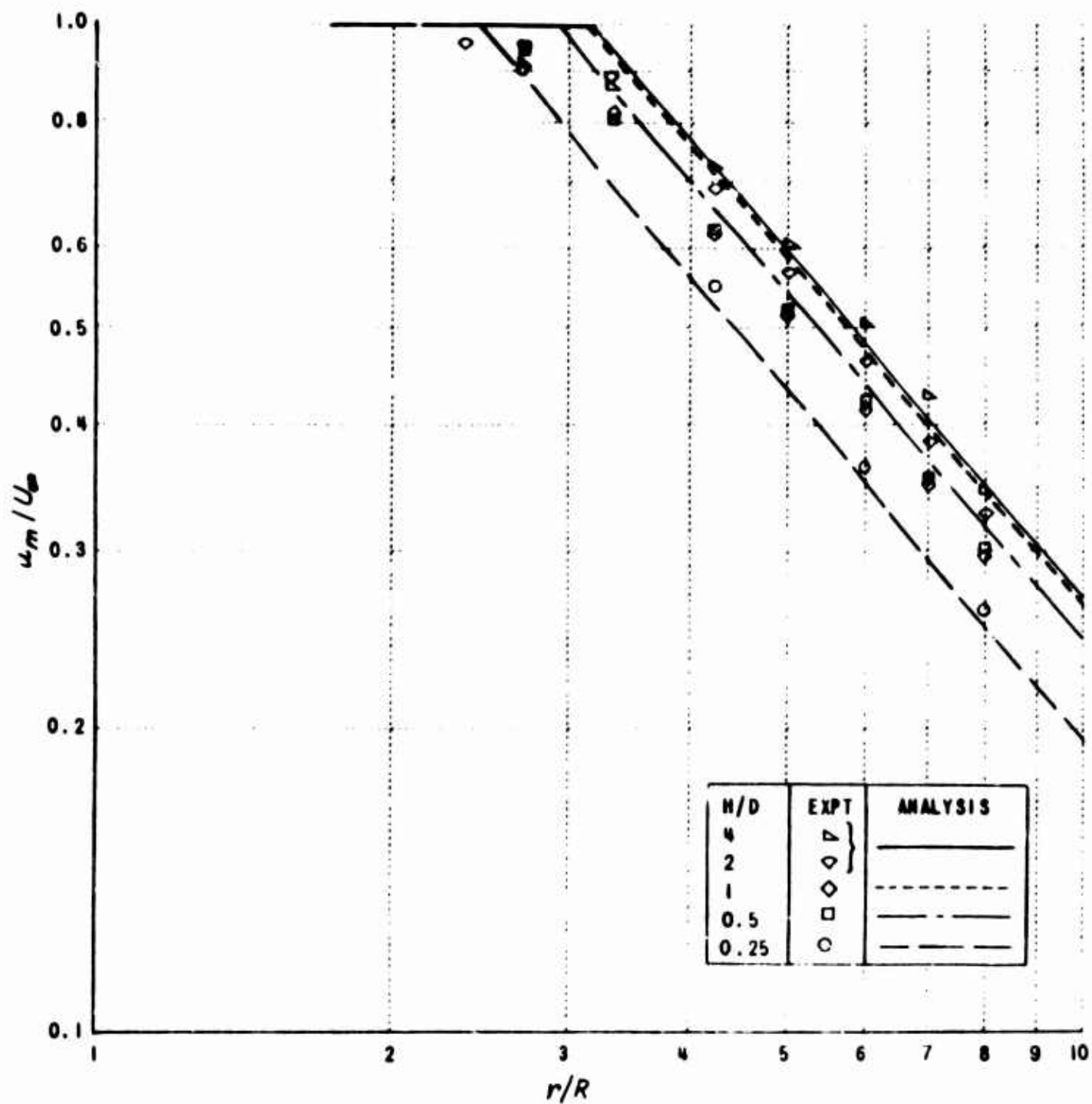
Figure 26   VARIATION OF FLOW PROPERTIES NEAR GROUND WITH RADIAL DISTANCE
FROM STAGNATION POINT, NORMALLY IMPINGING UNIFORM JET
(a)   MAXIMUM VELOCITY NEAR GROUND
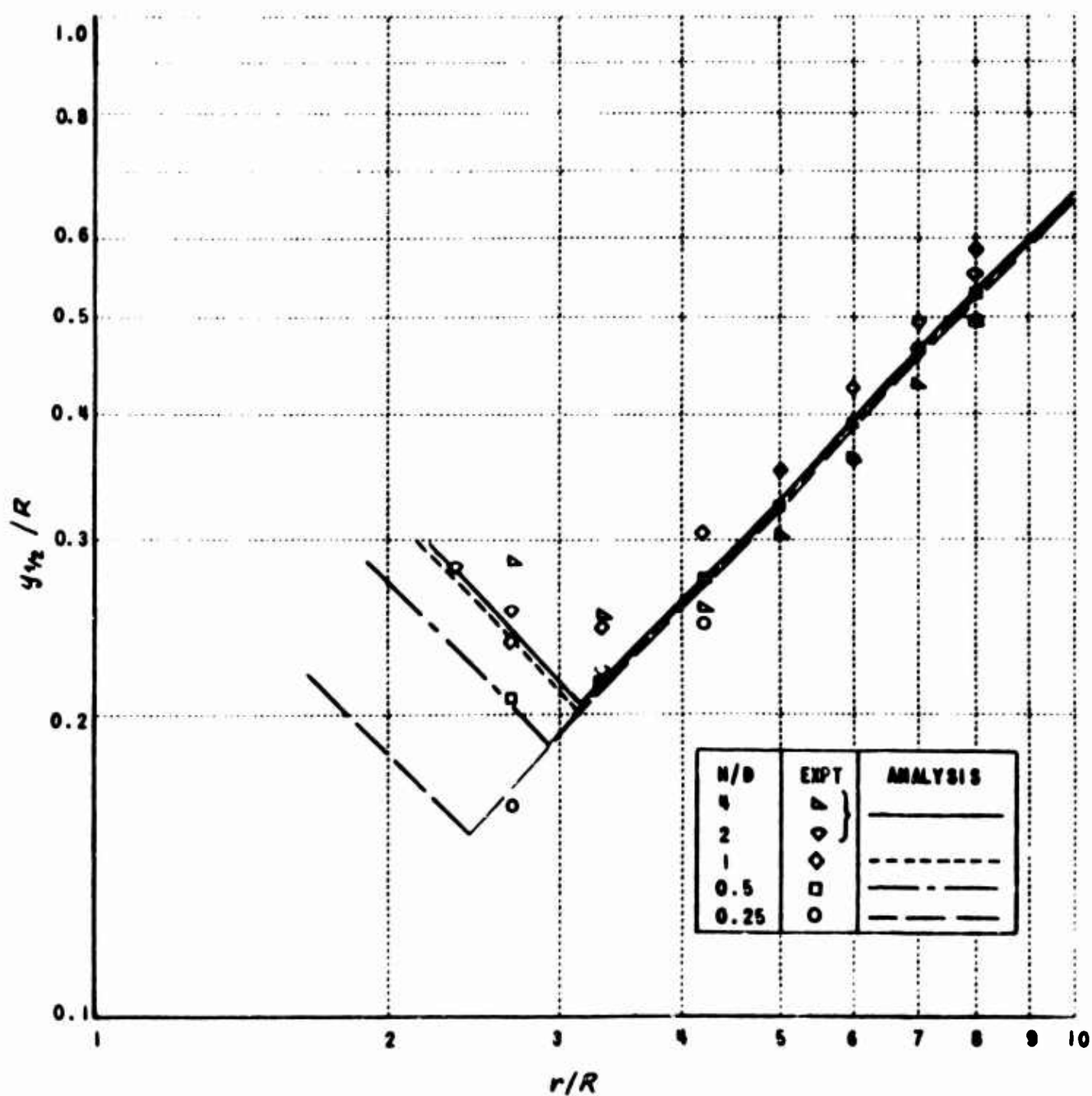
Figure 26 VARIATION OF FLOW PROPERTIES NEAR GROUND WITH RADIAL DISTANCE
FROM STAGNATION POINT, NORMALLY IMPINGING UNIFORM JET
(b) FLOW THICKNESS
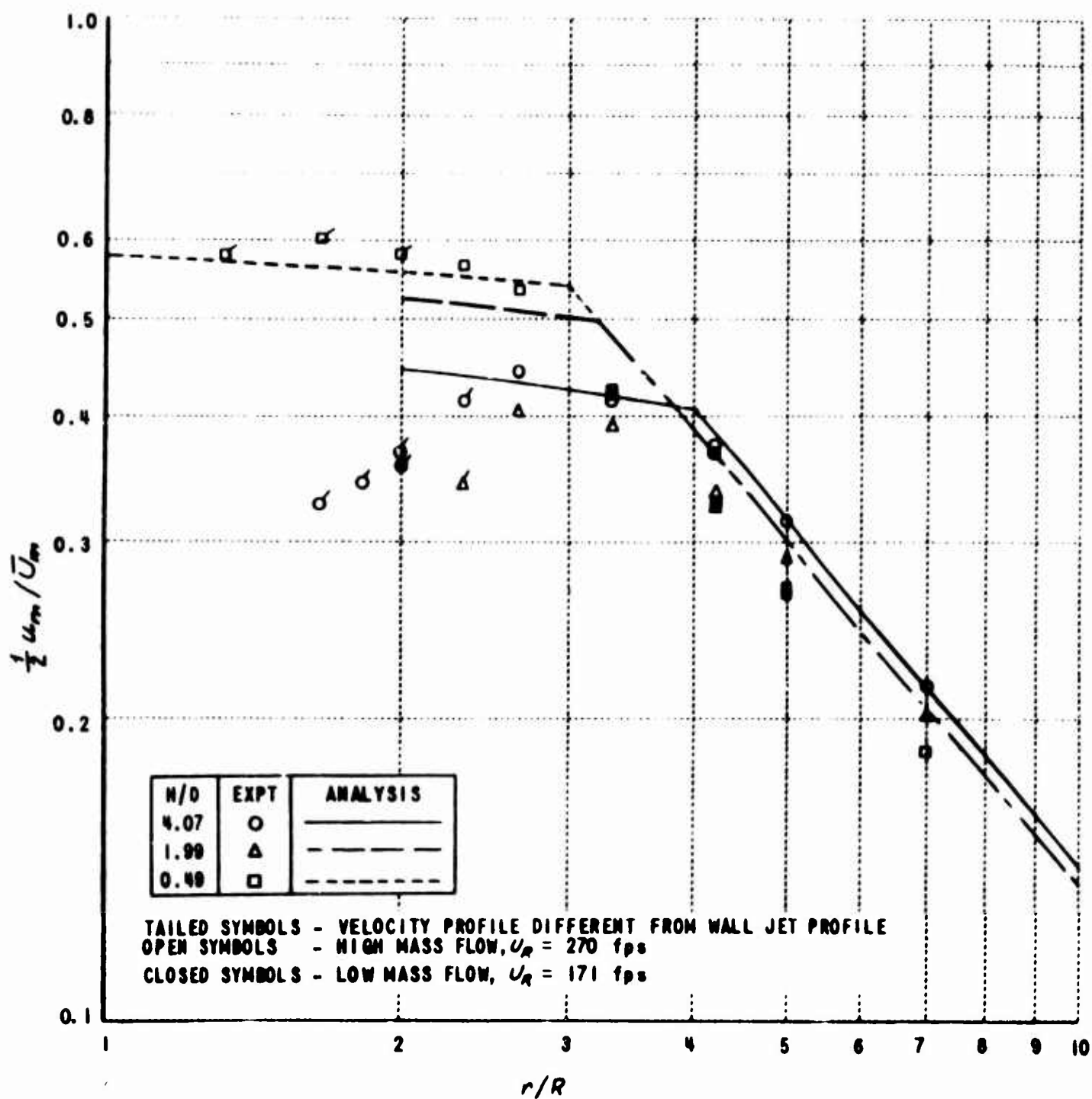
Figure 27 VARIATION OF FLOW PROPERTIES NEAR GROUND WITH RADIAL DISTANCE
FROM STAGNATION POINT, NORMALLY IMPINGING NONUNIFORM JET
(a) MAXIMUM VELOCITY NEAR GROUND
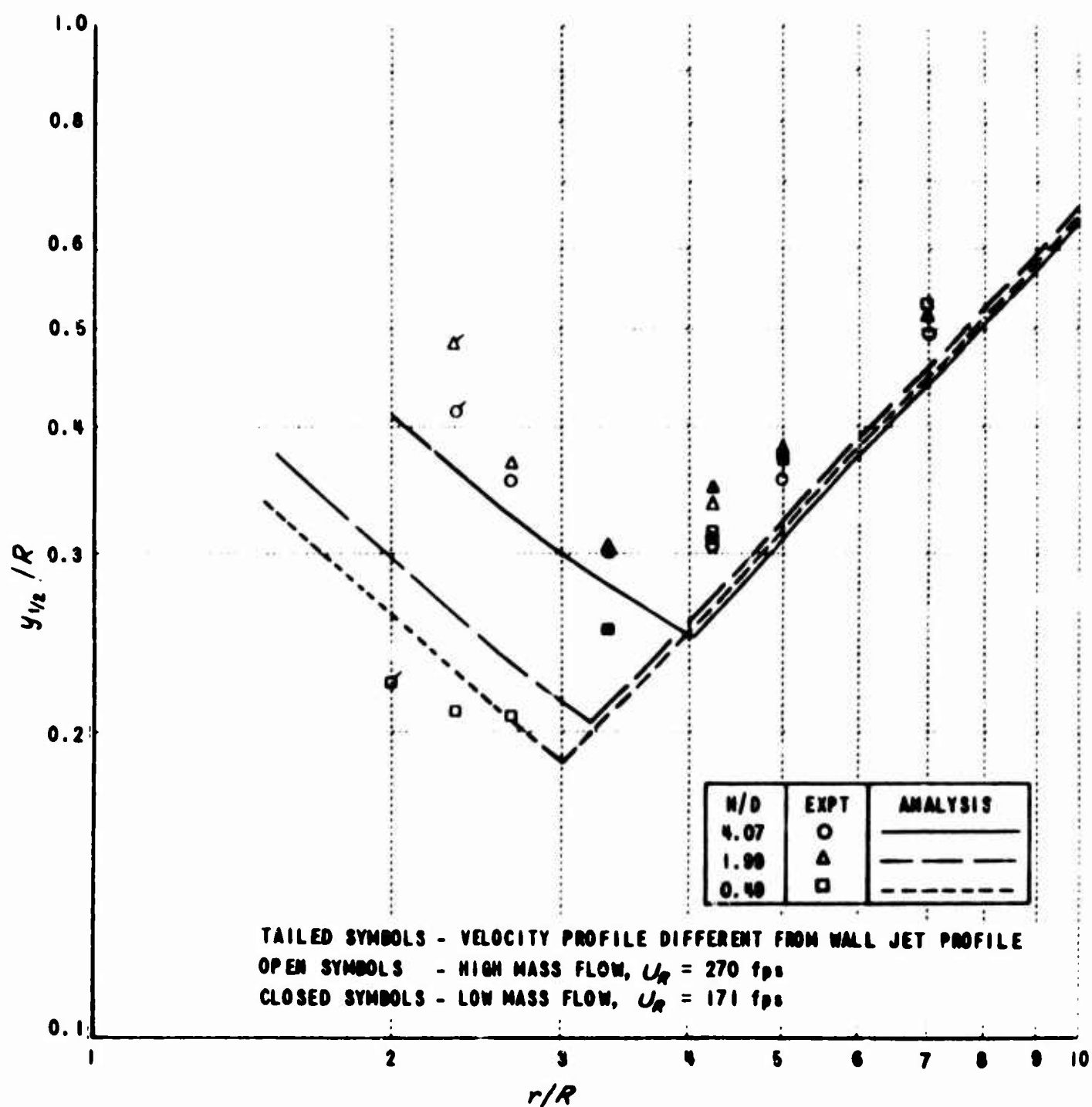
Figure 27   VARIATION OF FLOW PROPERTIES NEAR GROUND WITH RADIAL DISTANCE
FROM STAGNATION POINT, NORMALLY IMPINGING NONUNIFORM JET
(b) FLOW THICKNESS
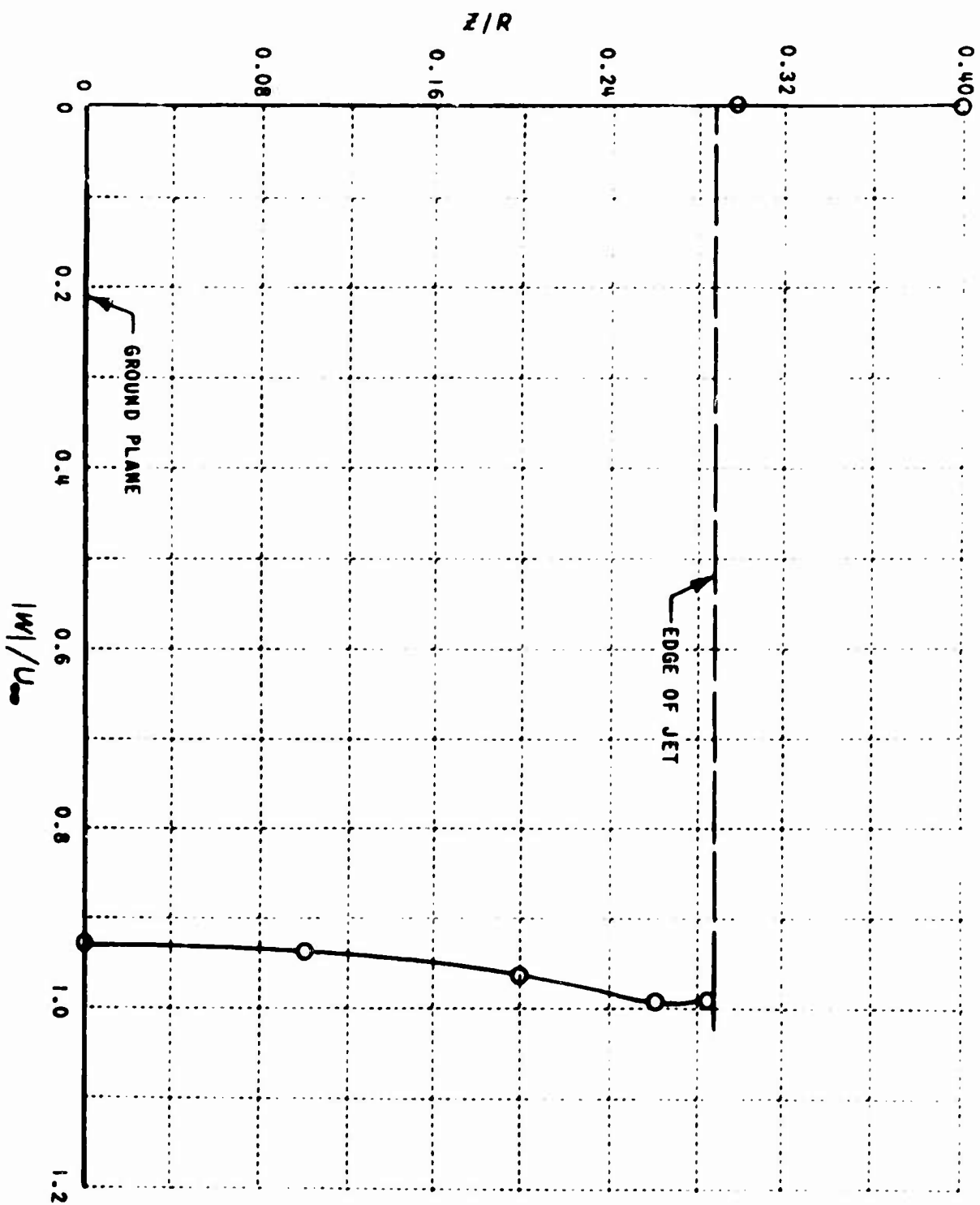
Figure 28 COMPUTED ABSOLUTE VELOCITY PROFILE PERPENDICULAR TO GROUND PLANE
FOR $r/D = 1.7$, $H/D = 1.0$, INVISCID UNIFORM JET ANALYSIS
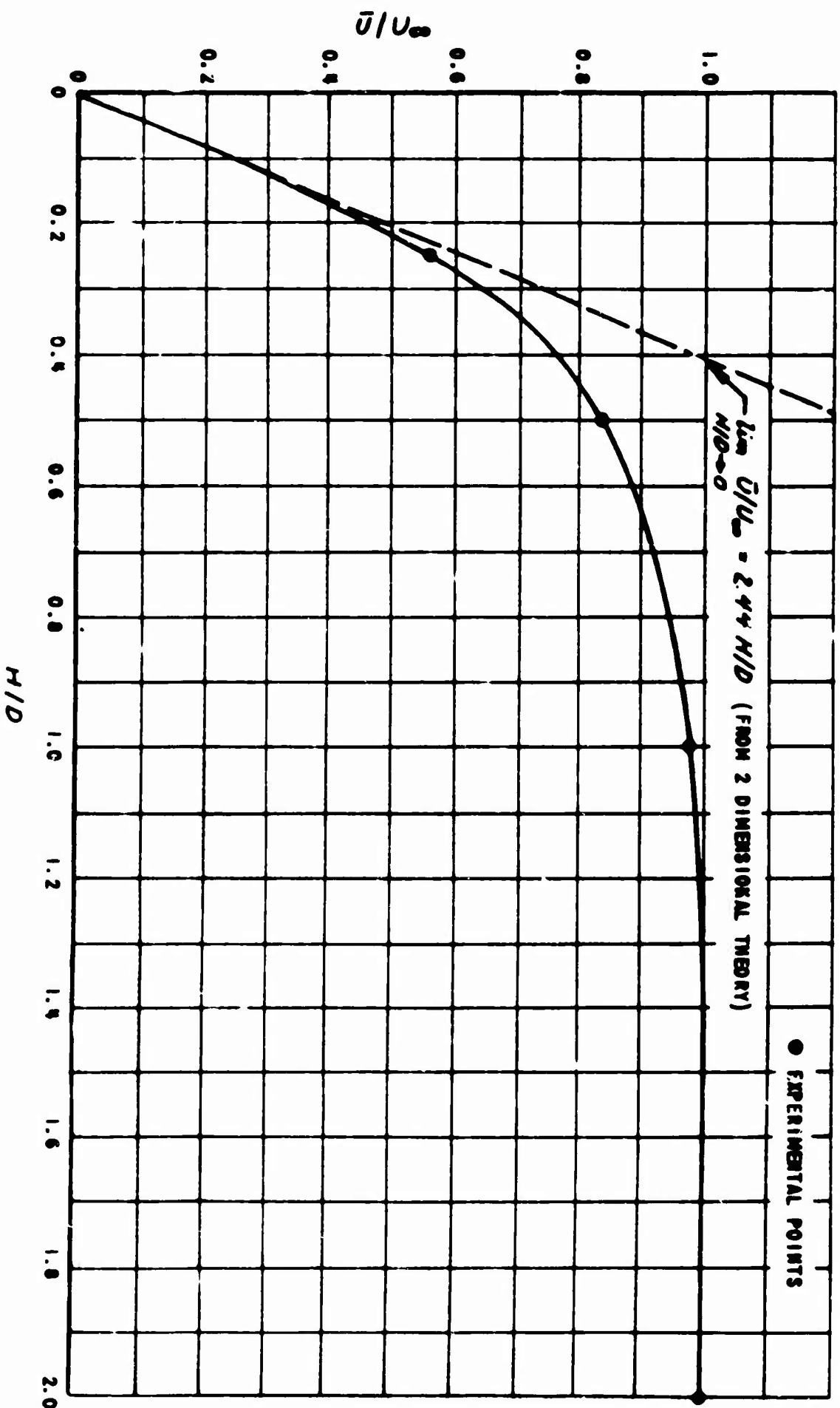
Figure 29 VARIATION OF $\bar{U}/U_\infty$ WITH H/D FOR A UNIFORM JET
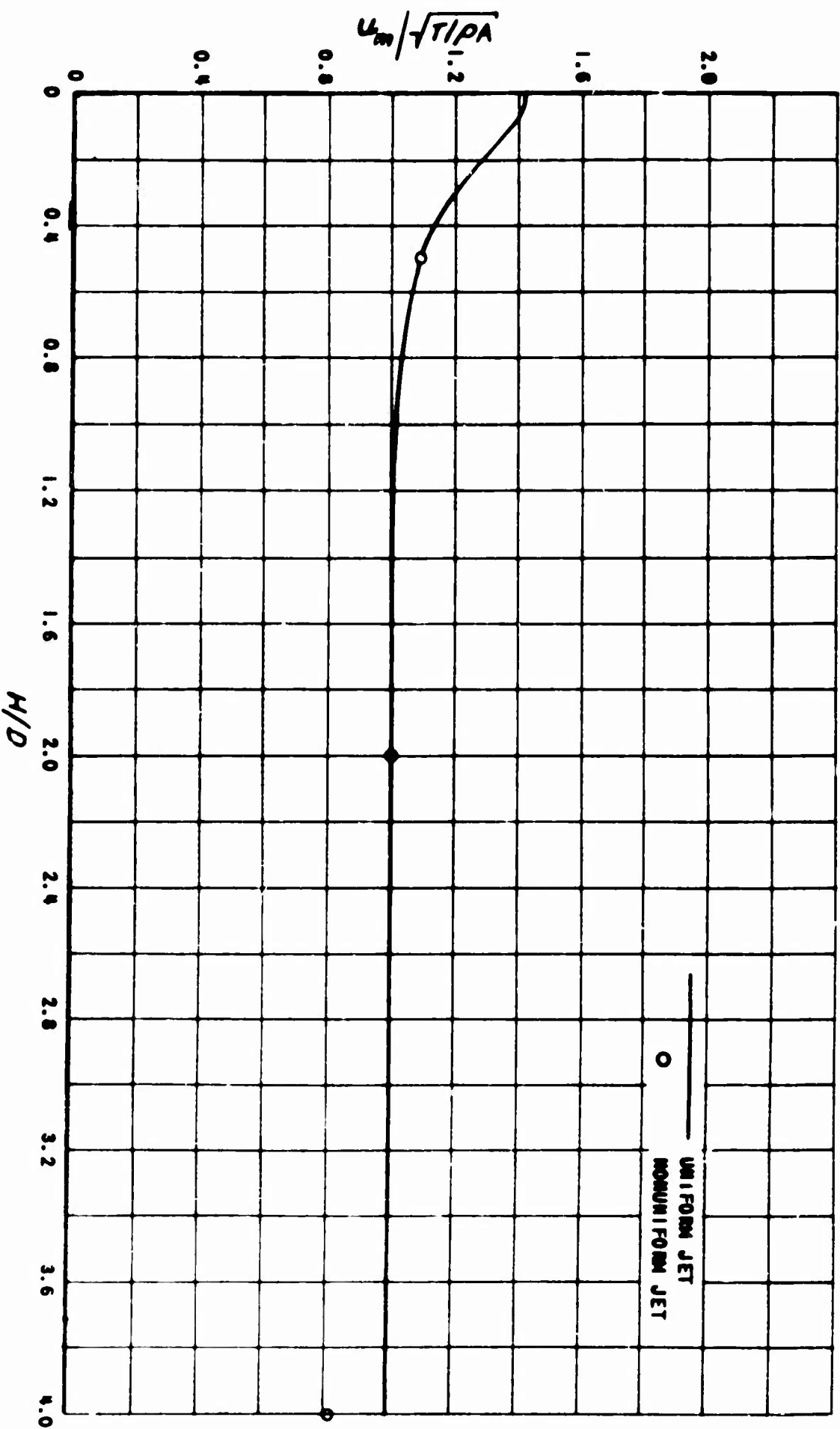
Figure 30 COMPARISON OF CALCULATED MAXIMUM VELOCITY NEAR GROUND AT START OF
WALL JET UNDER UNIFORM AND NONUNIFORM JETS OF EQUAL THRUST LOADING
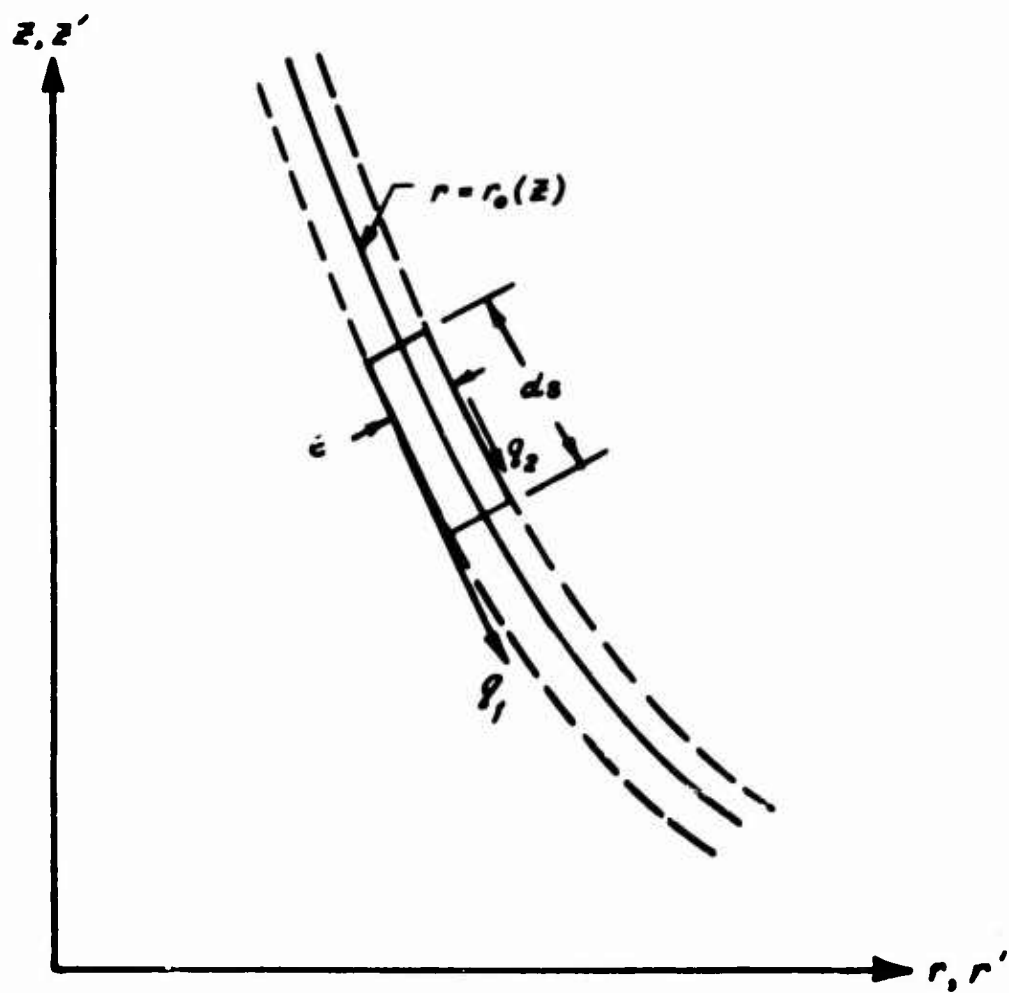
Figure 31 REPRESENTATION OF VORTICITY LAYER ON EDGE OF INVISCID JET
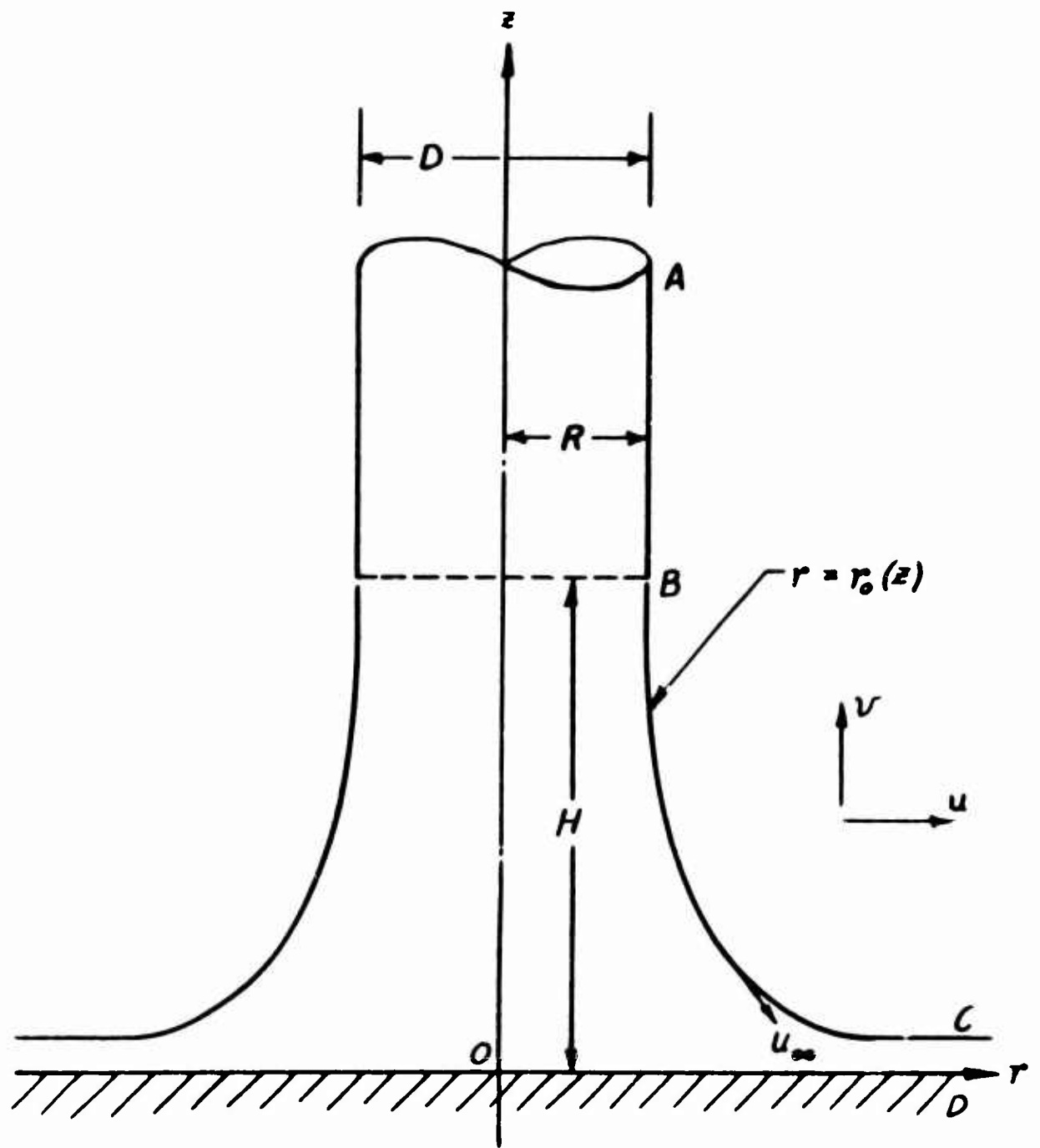
Figure 32 FLOW MODEL USED IN INVISCID ANALYSIS OF CIRCULAR
IMPINGING UNIFORM JET
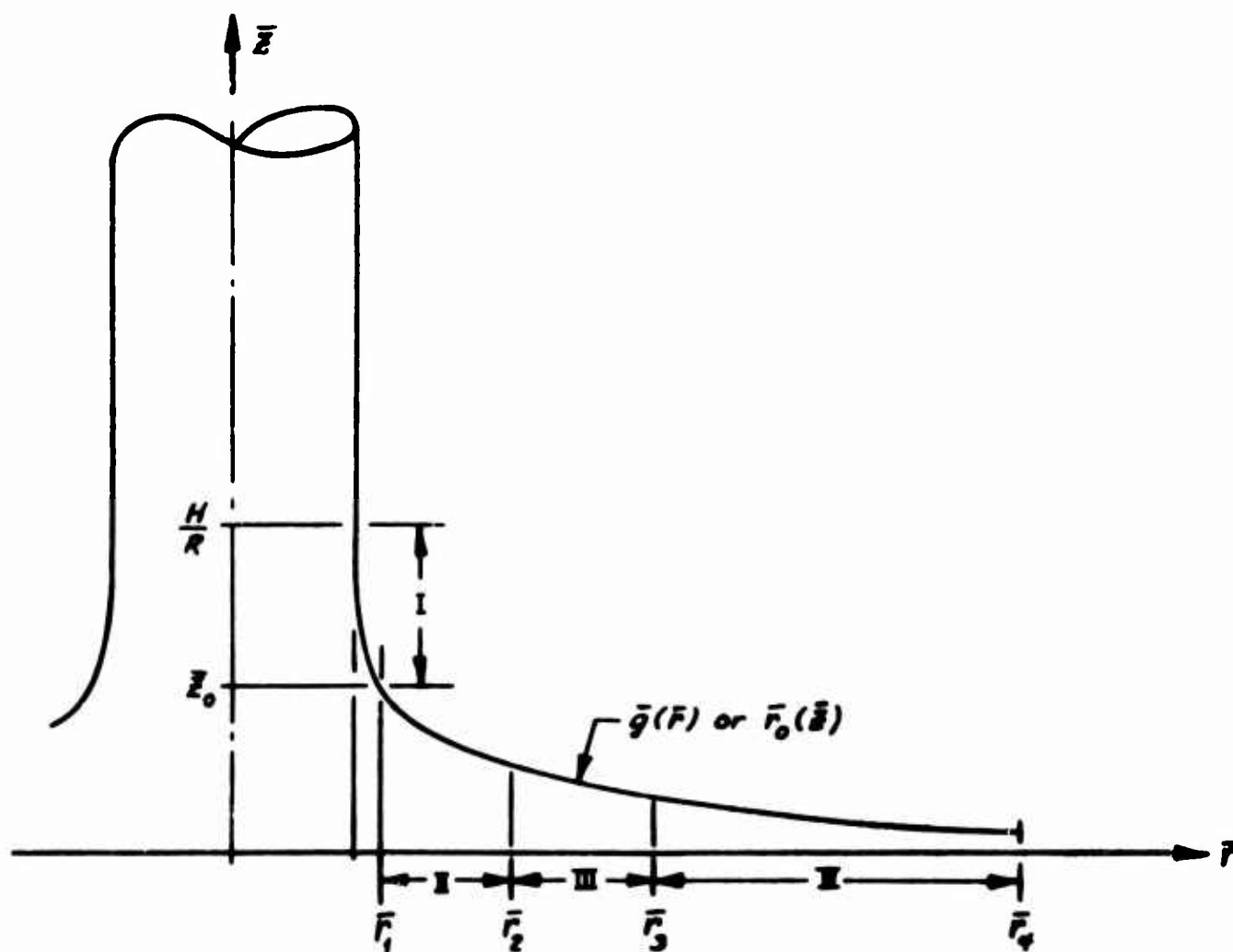
Figure 33 BREAKDOWN OF REGIONS OF INTEGRATION

DISTRIBUTION

U. S. Army Materiel Command	3
U. S. Army Mobility Command	3
U. S. Army Aviation Materiel Command	4
Chief of R&D, D/A	.
U. S. Army Transportation Research Command	67
U. S. Army Research and Development Group (Europe)	1
U. S. Army Engineer Research and Development Laboratories	3
Army Research Office-Durham	2
U. S. Army Test and Evaluation Command	1
U. S. Army Engineer Waterways Experiment Station	1
U. S. Army Combat Developments Command Aviation Agency	1
U. S. Army War College	1
U. S. Army Command and General Staff College	1
U. S. Army Aviation School	1
U. S. Army Infantry Center	2
U. S. Army Aviation Test Board	1
Air Force Systems Command, Wright-Patterson AFB	1
Air Force Flight Test Center, Edwards AFB	1
Bureau of Naval Weapons	4
U. S. Naval Postgraduate School	1
Naval Air Test Center	1
David Taylor Model Basin	1
Ames Research Center, NASA	1
NASA-LRC, Langley Station	1
Lewis Research Center, NASA	1
Manned Spacecraft Center, NASA	1
NASA Representative, Scientific and Technical Information Facility	2
Research Analysis Corporation	1
National Aviation Facilities Experimental Center	1
U. S. Army Standardization Group, Canada	1
Canadian Liaison Officer, U. S. Army Transportation School	1
British Army Staff, British Embassy	1
U. S. Army Standardization Group, U. K.	1
Defense Documentation Center	10

AD

Cornell Aeronautical Laboratory, Inc., Buffalo, N. Y.
THEORETICAL AND EXPERIMENTAL STUDIES OF ROTATING
UNIFORM AND NONUNIFORM JETS - W. Gerdes, Body and
Gary R. Ludwig, TRECOM Technical Report 64-42, Cal. Report
TC-1810-S-11, August 1964, 91 Pp. incl. illus. 6 refs. (Contract
DA 44-177-AMC-16(T)), UNATRECOM Task 1D121401A14175.

Unclassified Report

1. Vertical Takeoff Planes
2. Ducted Propellers
I. U. S. Army Transportation Research
   Command, Ft. Eustis, Va.
II. Cornell Aeronautical Laboratory,
   Buffalo, N. Y.
III. Contract DA 44-177-AMC-16(T)
IV. Body, V. Gerdes
V. Ludwig, Gary R.

AD

Cornell Aeronautical Laboratory, Inc., Buffalo, N. Y.
THEORETICAL AND EXPERIMENTAL STUDIES OF ROTATING
UNIFORM AND NONUNIFORM JETS - W. Gerdes, Body and
Gary R. Ludwig, TRECOM Technical Report 64-42, Cal. Report
TC-1810-S-11, August 1964, 91 Pp. incl. illus. 6 refs. (Contract
DA 44-177-AMC-16(T)), UNATRECOM Task 1D121401A14175.

Unclassified Report

1. Vertical Takeoff Planes
2. Ducted Propellers
I. U. S. Army Transportation Research
   Command, Ft. Eustis, Va.
II. Cornell Aeronautical Laboratory,
   Buffalo, N. Y.
III. Contract DA 44-177-AMC-16(T)
IV. Body, V. Gerdes
V. Ludwig, Gary R.